PLACE IN RETURN BOX to remove this checkout from your record. TO AVOID FINES return on or before date due.

DATE DUE	DATE DUE	DATE DUE

MSU is An Affirmative Action/Equal Opportunity Institution

## Subthreshold Pion Production From Characterized Events in <sup>20</sup>Ne + <sup>27</sup>Al Reactions

By

Stefan Andreas Hannuschke

#### A DISSERTATION

Submitted to
Michigan State University
in partial fulfillment of the requirements
for the degree of

DOCTOR OF PHILOSOPHY

Department of Physics and Astronomy

1996

#### ABSTRACT

## SUBTHRESHOLD PION PRODUCTION FROM CHARACTERIZED EVENTS IN $^{20}$ NE + $^{27}$ AL REACTIONS

By

#### Stefan Andreas Hannuschke

The production of positively charged pions below the free nucleon-nucleon threshold in intermediate energy heavy ion collisions was investigated. The system studied was <sup>20</sup>Ne + <sup>27</sup>Al at bombarding energies of 90, 110 and 150 AMeV. Pions and fragments were detected using the MSU  $4\pi$  Array yielding complete event characterization. Using the Array to determine the centrality of pion producing events, an apparent enhancement of the production cross section for peripheral events was found. That trend increases with decreasing bombarding energy. The kinetic energy distributions measured for protons and pions are in good agreement with BUU model calculations. The proton spectra are reproduced for all kinetic energies, whereas the pion spectra are under-predicted at the lower energies. Analyzing the energy spectra for all detection angles in terms of a classical Maxwell-Boltzmann distribution, the apparent temperatures for protons and pions were extracted. The values for both, pions and protons, are in very good agreement with known systematics. The pion temperatures show no dependence on the event centrality, whereas the ones for proton emission show a steady decrease with increasing impact parameter. Correlations of pions with the event as a whole were also investigated. The azimuthal distribution with respect to the reaction plane shows a weak in-plane emission for pions in the forward direction. A transverse flow analysis for pions and light charged particles shows the typical signal for helium and protons. The pions show an enhancement for forward rapidities at the highest beam energy.

For Sabine

#### ACKNOWLEDGEMENTS

I will probably never forget the first experiment I participated in here at the NSCL. After having looked at the  $4\pi$  Array and not having the slightest idea how it works, I was even more confused looking at some on-line spectra. Fortunately there were several people that helped me in my quest to learn something about nuclear physics.

Most importantly I would like to express my gratitude to my advisor Dr. Gary D. Westfall for giving me a chance to learn a great deal about the experimental side of nuclear physics. Working with him on several experiments, and understanding more and more about them, was not only a challenge but also a great pleasure. His guidance during my studies here was always balanced; never too pushy but always willing to answer any questions I might have had. His great experience in physics often allowed him to steer me away from dead ends.

The other person I owe a great deal to is Skip Vander Molen. He originally proposed the experiment that kept me busy for the last few years. His immense knowledge of the data aquisition system and computers in general (and the ability to decipher hex numbers in his head) has inspired me to learn something about these things myself. He told me as much about getting the data to tape as Gary did making sense out of it. Skips helpful criticism in group meetings often made me sit back and re-think the results I was so excited about, noticing the one or other flaw in them.

The other members of the  $4\pi$  group also deserve a great deal of credit for providing a very pleasant working environment and always an open ear for discussions, not only about physics. All graduate students I worked with, Tong Li, Eugene Gualtieri, Jaeyong Yee, Robert Pak, Nathan Stone and Omar Bjarki (in approximate order of disappearance), always made sure that the next experiment was a full success. The

post-docs I got to know, Roy Lacey, Sherry Yenello and Bill Llope, were all good role models for a successful career in physics. They taught me how to set up experimental devices and never got tired of explaining why what I just did wouldn't work.

I would also like to thank the entire operating staff of the NSCL for providing the necessary ingredients for the run and analysis of my experiment. Special thanks goes to the computer group for never complaining when I bugged them to move tape drives, get more disk space, or even fix something in the middle of the night.

Since my graduate work here at MSU consisted not only of research, but also of class work, I would like to thank my teachers for a very good education in other fields of physics. I very much enjoyed their teaching and learned a great deal about gamma matrices and Schwarzschild metric.

My parents, Sigrid and Klaus Hannuschke, as well as my parents in law, although not being geographically close, were always with me during the last five years. Their continuing support, not only in the form of mailings of chocolate, smoked ham and coffee, made this work possible.

Also I would like to thank all my friends for not being upset when I "had to go to the lab" during parties and other get-togethers.

Last, but certainly not least, I would like to thank my wife, Sabine Helling, for her tremendous patience with me. I think the last few years were harder on her than on me. Although working on her own degree, she was always willing to unburden me of the "little things", without even mentioning it. Without her unconditional support I would not have been able to finish this work.

## **Contents**

LI	ST (	OF TABLES	vii
LI	ST (	OF FIGURES	viii
1	Intr	roduction	1
2	Exp	perimental Details	6
	2.1	Introduction	6
	2.2	The Michigan State University $4\pi$ Array	6
		2.2.1 Plastic Phoswich Counters	7
		2.2.2 Bragg Curve Counters	12
		2.2.3 Phoswich Calibration	18
		2.2.4 BCC Calibration	23
	2.3	Charged Pion identification	24
	2.4	Pion Energy Calibration	32
	2.5	The Experiment	35
3	Cer	ntrality of Pion Producing Events	40
	3.1	Introduction	40
	3.2	Centrality Selection	40
	3.3	Less Central	41
4	Sin	gle Particle Distributions	51
	4.1	Polar Angle Distributions	51
	4.2	Kinetic Energy Distributions	52
5	Azi	muthal Distributions and Transverse Flow	73
	5.1	Introduction	73
	5.2	Azimuthal Correlations	74

	5.3 Transverse Flow	79
6	Conclusion	85
A	Impact Parameter Selection	88
	A.1 Method	88
LI	IST OF REFERENCES	95

## List of Tables

2.1	Scintillator Characteristics	11
2.2	Phoswich Specifications	11
2.3	BCC Specifications	18
2.4	BCC Specifications	24
2.5	Pion Statistics	39
4.1	Pion Temperature Compilation	58
A.1	Impact parameter bins for KE <sub>t</sub>	90
<b>A.2</b>	Impact parameter bins for N <sub>ch</sub>	92
<b>A.3</b>	Impact parameter bins for $N_{lcp}$	92
A.4	Impact parameter bins for Z <sub>mr</sub>	92

# List of Figures

1.1	Pion slope factors for several systems
1.2	Transverse flow for pions at high energies
1.3	Polar angle distribution for neutral pions
2.1	$4\pi$ Array Schematic
2.2	$4\pi$ Module Schematic
2.3	Forward Array Schematic
2.4	Phoswich Signal and Gates
2.5	Ball Phoswich Spectrum
2.6	FA Phoswich Spectrum
2.7	BCC Diagram
2.8	BCC vs. Fast Plastic Spectrum
2.9	Ball PID Gates
2.10	FA PID Gates
2.11	Ball Response Functions
2.12	BCC Response
2.13	BCC vs. Fast Plastic Template
2.14	$E_{\mu}$ Signal and Gates
2.15	Inclusive Ball $\Delta E$ vs. E spectrum
2.16	$E_{\mu}$ gated Ball $\Delta E$ vs. E spectrum
2.17	Ring distributions for several PID gates
2.18	Parameters for ring distributions
2.19	Pion and proton energy calibration from the Plastic Ball 36
2.20	Pion energy calibration for plastic phoswich
3.1	Centrality of pion events, 150 AMeV
3.2	Centrality of pion events, 90 AMeV
3.3	Comparison of pion yield with BUU calculations
3.4	Gated KE <sub>t</sub> distributions

3.5	Mean KE <sub>t</sub> values for different gates	48
3.6	Impact parameter distributions for pion events	50
4.1	Laboratory polar angle distributions for several particle types	<b>53</b>
4.2	Gated lab polar angle distributions	<b>54</b>
4.3	BUU and data comparison of polar angle distributions for protons	<b>55</b>
4.4	BUU and data comparison of polar angle distributions for pions	56
4.5	Pion kinetic energy distributions at 150 AMeV	<b>59</b>
4.6	Pion kinetic energy distributions at 110 AMeV	60
4.7	Fit parameters for pions at 150 AMeV	62
4.8	Fit parameters for pions at 110 AMeV	63
4.9	Pion temperature compilation	64
4.10	Beam energy dependence of pion source velocity and slope parameter	66
4.11	Proton kinetic energy distributions at 90 AMeV	67
4.12	Fit parameters for protons at 90 AMeV	68
4.13	Beam energy dependence of proton source velocity and slope parameter	70
4.14	Comparison of spectral shapes with BUU for protons	71
4.15	Comparison of spectral shapes with BUU for pions	72
5.1	Reaction plane determination method	75
<b>5.2</b>	Azimuthal distributions for He ions at 150 AMeV	76
<b>5.3</b>	Azimuthal distributions for He ions at 90 AMeV	76
5.4	Azimuthal distributions for pions and protons at 150 AMeV	78
5.5	Transverse flow for helium	80
5.6	Transverse flow for protons	81
5.7	Transverse flow for pions	<b>82</b>
5.8	Summary of transverse flow for helium, protons and pions	84
A.1	Probability distributions for centrality observables	91
<b>A.2</b>	Estimate of maximum impact parameter	94

## Chapter 1

## Introduction

The study of meson production below the free nucleon-nucleon threshold can provide valuable information about the formation of hot nuclear matter far away from the ground state and lead to a better understanding for the nuclear equation of state (EOS)[Brau 87, Gutb 89, Dani 88]. Because mesons must be created in the reaction rather than be merely liberated, they are dominantly emitted from the hottest and most dense regions created in central collisions [Suzu 91a]. Pions, being the lightest mesons, have been observed from collisions at incident energies as low as 25 AMeV. The production of pions can be understood in terms of the BUU model except at the very lowest incident energies where an abnormally high momentum tail of the Fermi distribution of the constituent nucleons has to be assumed to explain the observed data [Niit 91].

A great deal of work has been done in understanding the inclusive production of pions from a variety of systems. In general, the production cross sections and energy spectra can be understood in terms of BUU [Li 91b]. One striking feature that has emerged recently is the small variation in the slope parameter,  $T_0$ , of the pion invariant cross section kinetic energy spectra at 90° in the center of mass frame for beam energies below 100 AMeV [Suzu 91b] (see Figure 1.1).

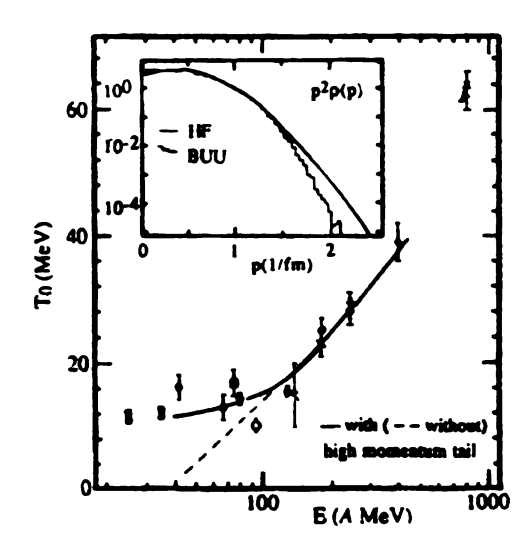


Figure 1.1: Slope factors (T<sub>0</sub>) for  $\pi^-$  spectra at  $\theta_{CM}$  together with the temperatures (T\*) deduced from  $\pi^0$  distributions. The inset shows the shape of the momentum distribution used in the calculation. From [Suzu 91a].

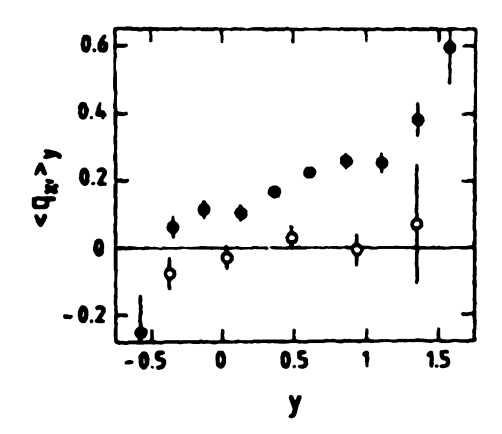


Figure 1.2:  $\langle q_{x'} \rangle_y$  vs. rapidity y for  $\pi^+$  produced in Ne-Pb collisions at 800 AMeV.  $q_{x'}$  is the transverse momentum, normalized to the pion mass, in the estimated reaction plane. Experimental results (filled circles) are compared to the results of intranuclear-cascade (INC) calculations (open circles) for collisions with squared reduced impact parameter  $b^2/(R_1 + R_2)^2 \approx 0.18$ . From [Goss 89].

Pion production from characterized events has been studied at Saclay at high energies (400, 600, 800 AMeV) using Diogene [Goss 89]. Figure 1.2 shows the pion transverse flow in the estimated reaction plane. Except for the point at the lowest rapidity the flow is positive for all rapidities. This positive flow was attributed to absorption of the pions in nuclear matter.

At intermediate energies pion production has been studied using the MUR at GANIL in coincidence with a single pion detector. The system studied was 94 AMeV O+Al [Aiel 88]. The authors found that coincident particle distributions are very similar for high energy proton and pion triggered events but different from those in inclusive reactions. In a similar experiment, pion production in coincidence with fission fragments was studied using the system O+Th at 95 AMeV [Eraz 88]. Through an analysis of the impact parameter distributions obtained from the fission fragment folding angles, the authors concluded that pion production requires a large overlap of the target and projectile nuclei.

In a recent experiment [Schu 94] polar and azimuthal distributions of subthreshold neutral pions were measured in coincidence with projectile-like fragments (see Figure 1.3). The findings are that the final-state interaction of pions with the nuclear medium seems to play an important role.

We studied  $^{20}$ Ne +  $^{27}$ Al reactions at 90, 110 and 150 AMeV with close to  $4\pi$  coverage for pion detection and event characterization. The good solid angle coverage of the device enables us to perform a detailed analysis of event properties such as reaction plane, impact parameter and degree of multifragmentation for inclusive events and events in which a pion was detected. The range of bombarding energies studied covers the balance energy for this system where the transverse collective flow disappears.

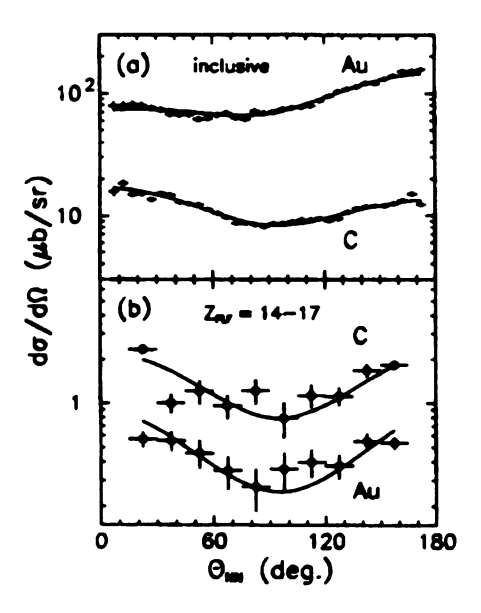


Figure 1.3: (a) Inclusive  $\pi^0$  polar distribution measured for  $^{36}$ Ar +  $^{197}$ Au and  $^{36}$ Ar +  $^{12}$ C at 95 AMeV, transformed into the N-N cm frame. (b) same as (a), but for very peripheral collisions, selected by requiring  $Z_{\rm PLF}$  in the range 14 – 17. The solid curves are shadowing calculations normalized to the integral of the data. From [Schu 94].

The remainder of this study is organized as follows. Chapter 2 contains a description of the technical details of the experiment, including a description of the MSU  $4\pi$  Array and its subelements, as well as information about the electronic modules and logic used to record the data. An outline of the on-line and off-line data analysis and the detector calibrations is also given. The pion detection and identification method is explained in detail. In Chapter 3 we investigate the centrality distributions and compare events where a pion was identified with inclusive events. Different methods for determining the approximate impact parameter of the collision are presented. Chapter 4 deals with single particle observables for pions and protons. Comparisons of angular and kinetic energy distributions are made with BUU model calculations. Inverse slope parameters for the pion and proton kinetic energy spectra are determined and compared with known systematics for similar systems. In Chapter 5 the correlation of the pion with global event properties is investigated and the results

compared with those for protons and helium. In particular we show the azimuthal distributions with respect to the approximate reaction plane and the transverse flow in that plane. In Chapter 6 we summarize the results of this study. Appendix A discusses the experimental determination of the centrality of an event, and the technique of impact parameter determination based on different global observables.

## Chapter 2

## **Experimental Details**

### 2.1 Introduction

The  $4\pi$  Array, as instrumented for this experiment, provided close to  $4\pi$  detection of light charged particles, intermediate mass fragments, and positively charged pions. Most previous experiments studying subthreshold pion production did not have coverage as complete as that provided by the  $4\pi$  Array, either in geometric acceptance or range of particle types identified.

The following sections in this chapter describe in detail the  $4\pi$  Array, its various components and their acceptance, and the methods used to calibrate them.

### 2.2 The Michigan State University $4\pi$ Array

The MSU  $4\pi$  Array [West 85] consists of a 32-faced, aluminum, truncated icosahedron housing several different detector subsystems. Of the 32 faces, 20 are of hexagonal shape and 12 are pentagonal. If one were to paint the hexagons white and the pentagons black the Array would look like a giant scoccer ball. On all of the hexagonal and on 10 of the pentagonal faces aluminum plates are mounted that serve as backplates for the 30 modules of the main Ball. One of the remaining pentagons serves

as the mount for the beam entrance pipe as well as the target mechanism. The other one supports the Forward Array and the exit beam pipe. The shape of the Array is shown in Figure 2.1.

The 30 modules of the main Ball are each divided into 6 (hex) or 5 (pent) triangular sub-modules of close packed fast/slow plastic phoswich detectors. Mounted in front of each of the 30 modules are gas ionization chambers that are capable of functioning as Bragg curve counters or serve as  $\Delta E$  detectors for low energy particles that stop in the fast plastic scintillator. The 5 most forward of the gas counters are further segmented into 6 separate detectors. A schematic view of a Ball hexagonal module is shown in Figure 2.2. In total the main Ball consists of 170 plastic phoswich detectors and 55 gas ionization chambers covering polar angles from about 18° to 162°. Mounted on the most forward pentagonal face is the Forward Array consisting of 45 fast/slow plastic phoswich counters, covering approximately 54% of the solid angle from 7° to 18°.

#### 2.2.1 Plastic Phoswich Counters

The 170 plastic phoswich counters in the main Ball are composed of a 3 mm thick layer of Bicron BC-412 fast plastic scintillator ( $\Delta E$  component) which is optically coupled to a 250 mm thick block of Bicron BC-444 slow plastic scintillator (E component). The terms "fast" and "slow" refer to the rise time of the light pulse in either of the components for charged particle energy deposition. The specifications for the two scintillator materials are summarized in Table 2.1. The solid angles of each of the submodules in the hexagonal and pentagonal modules are 66 msr and 50 msr respectively. The total solid angle subtended by the main Ball detectors is therefore 10420 msr or 83% of  $4\pi$ . The phoswich detectors in the Forward Array are composed of the same scintillator material. They also come in two different shapes. There are 30 cylindrical

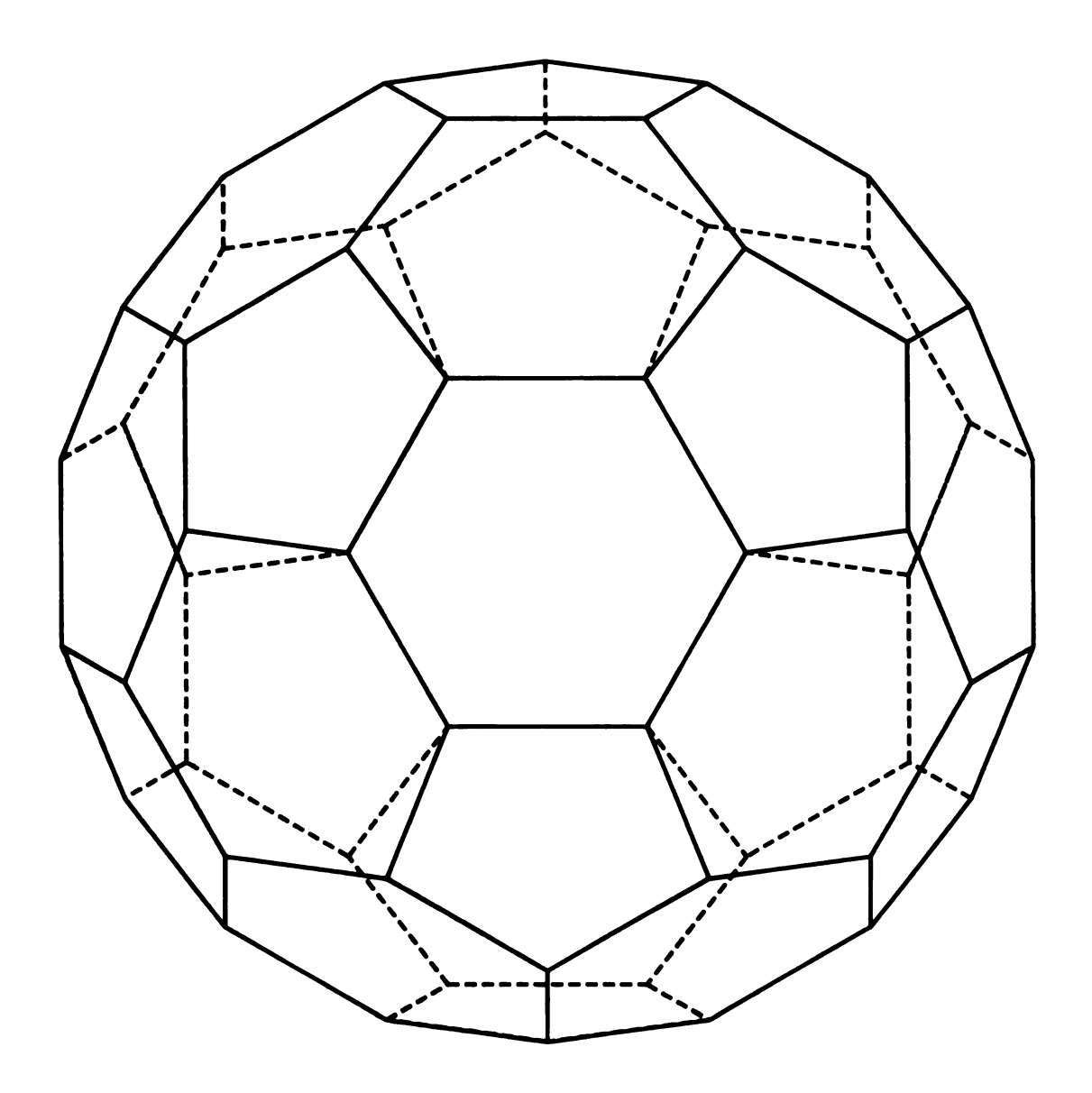


Figure 2.1: Schematic diagram showing the underlying geometry of the  $4\pi$  Array.

### SUBARRAY OF MULTIPARTICLE ARRAY

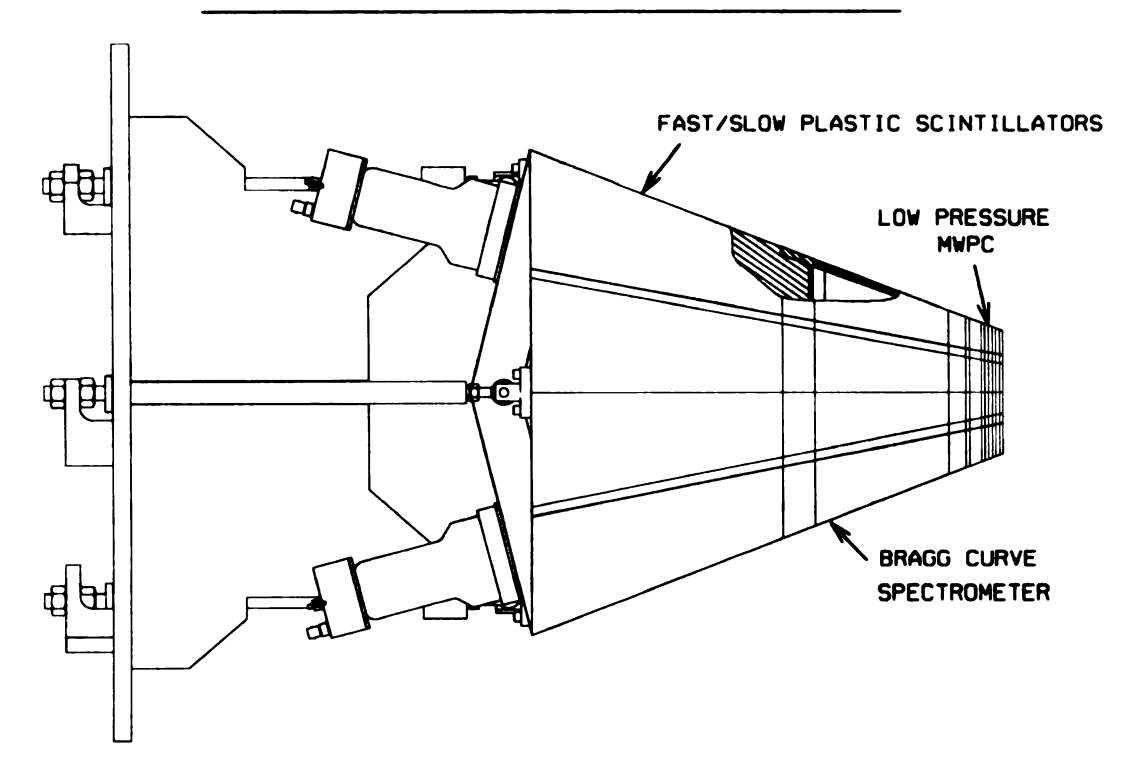


Figure 2.2: Schematic diagram showing the components of a  $4\pi$  module.

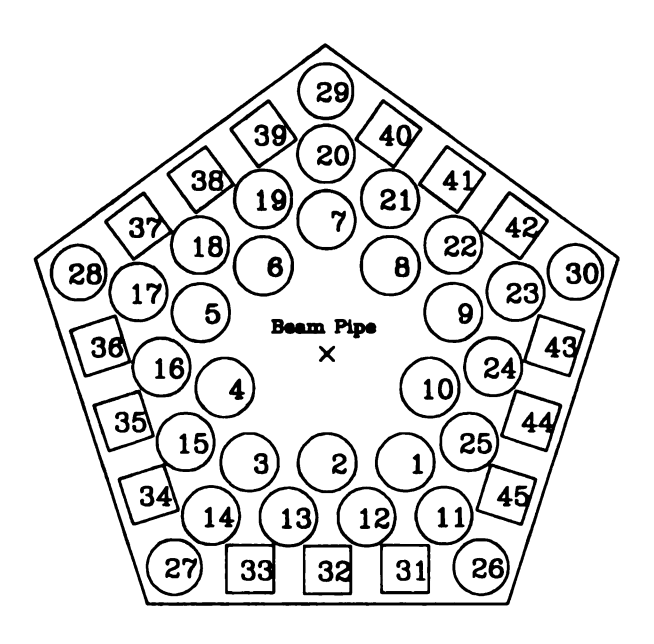


Figure 2.3: The layout of the 45 Forward Array detectors.

and 15 truncated pyramidal detectors. The fast ( $\Delta E$ ) component is only 1.6 mm thick and the slow (E) component 150 mm for the cylinders and 130 mm for the truncated pyramids. The thinner  $\Delta E$  component allows for a lower kinetic energy threshold for the heavier fragments in the forward direction. The solid angles are 3.02 msr and 2.75 msr for cylindrical and pyramidal, respectively, therefore covering about 54% of the total solid angle between 7° and 18°. A summary of low energy threshold, angular coverage, and Z identification capabilities is given in Table 2.2.

Energetic charged particles penetrating a phoswich detector will produce two different flashes of light. The first one originates from the fast ΔE component, which is proportional to the rate of energy loss in that medium, and the second one comes from the slow E component. If the particle stops in the second component that signal will be proportional to the total energy of the ion after passing through the fast component. The combined light pulse is transformed into an electronic signal and amplified via 8-stage Amperex photo-multiplier tubes. The resulting signals are then approximately separated into the fast and slow components by means of two different gates to charge-to-digital converters (QDC, Lecroy FERA 4301B). A schematic of the signal with the corresponding gates is drawn in Figure 2.4.

Figures 2.5 and 2.6 show examples of the 2-dimensional spectra obtained by plotting the fast ( $\Delta E$ ) signal against the slow (E) signal. The strong band along the  $\Delta E$  axis is from particles that stop in the fast plastic layer and have therefore no slow signal. The fact that a small amount of E is present is simply due to the integration of the tail of the fast signal in the E gate to the FERA. Similarly, the line at the bottom of the spectra is caused by particles such as neutrons or photons that deposit no or very small amounts of energy in the fast layer. The tilt of this line arises from integration of a part of the slow signal in the  $\Delta E$  gate to the FERA. Naturally all charged particles approach that line as their  $\Delta E$  goes to zero. In the spectrum for

Table 2.1: Characteristics of the two types of scintillator used in the phoswich detectors.

BICRON Plastic	Rise time (ns)	Fall time (ns)
BC-412 (fast)	1.0	3.3
BC-444 (slow)	19.5	179.7

Table 2.2: Specification of the Ball and Forward Array phoswich detectors.

Characteristic	Ball Phoswich	FA Phoswich
Polar Angle region (°)	18 - 162	7 - 18
Solid Angle coverage (%)	84	54
Z identification	1 - 8	1 - 10
Energy Threshold (AMeV)		
Pion	8	N/A
Proton	12	7
Helium	17	12
Carbon	32	22

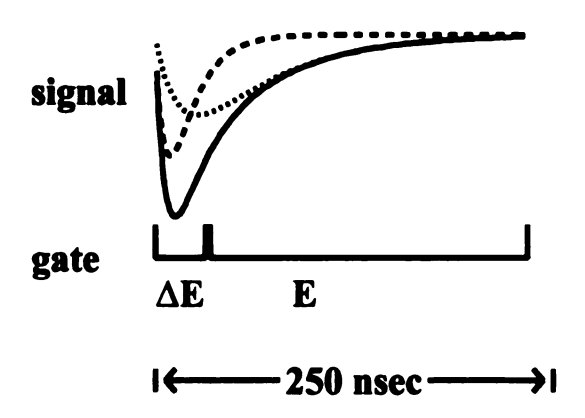


Figure 2.4: Diagram of the phoswich signal and gates.

the Ball detector (Figure 2.5) lines can be observed for Z = 1 to 3, possibly four, with isotope resolution for Z = 1. If one displays these spectra in a higher resolution even <sup>3</sup>He and <sup>4</sup>He can be separated. The Forward Array spectrum also shows lines for Z = 1 to 3, again with isotope resolution for Z = 1. With more statistics higher Z = 1 lines can be observed. The bin width in both histograms is 16 FERA channels, so that the actual resolution is better than the figures indicate.

### 2.2.2 Bragg Curve Counters

In addition to the 170 main Ball phoswich counters and the 45 forward array counters the  $4\pi$  Array contains 30 gas-filled ionization chambers (Bragg Curve Counters). The ion chambers are directly mounted on the face of the main Ball phoswich modules. They are of either hexagonal or pentagonal pyramidal shape depending on which type of Ball module they are mounted on. A 2.5  $\mu$ m thick aluminum coating is evaporated on the face of the phoswich fast plastic layer and serves as the anode for the BCC. In the most forward ring of the main Ball modules (5 hexagons) the anode is separated into 6 electrically isolated segments corresponding to the 6 phoswich submodules. The total number of BCC is therefore 55 with only 30 separate gas volumes. The front pressure windows are made of 900  $\mu$ g/cm², aluminized kapton foil. These windows are epoxied to a stainless steel frame that serves at the same time as the cathode for the BCC. The perpendicular distance from the anode to the cathode is 13.36 cm.

In front of the anode at a distance of about 1 cm a Frisch grid is installed in the BCCs. It is made of 12.5  $\mu$ m gold plated tungsten wires spaced .5 mm apart, and epoxied with conductive epoxy to a copper strip on the BCC frame. The Frisch grid is held at ground potential in order to shield the anode from the image charge induced by the drifting electrons. In order to produce an approximately radial electric field inside the BCC chamber, a shaping grid is installed inside the housing. It consists

#### **Main Ball Phoswich Spectrum**

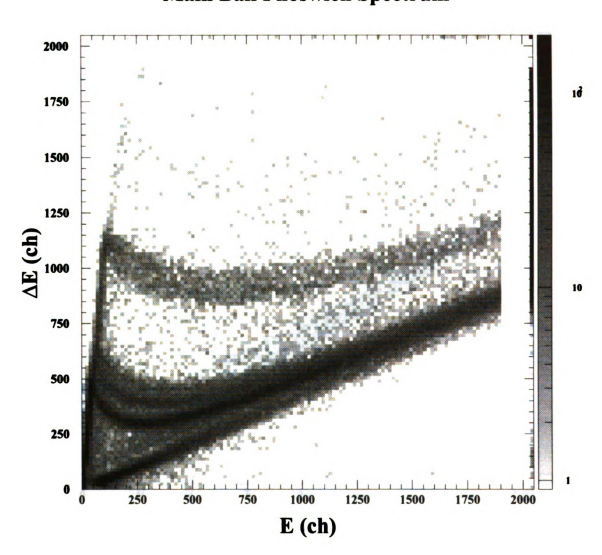


Figure 2.5: Typical raw spectrum from a Ball phoswich for Ne + Al at 150 AMeV. Lines for particles of Z=1 - 3 are identified with isotopic resolution for Z=1.

## **Forward Array Phoswich Spectrum**

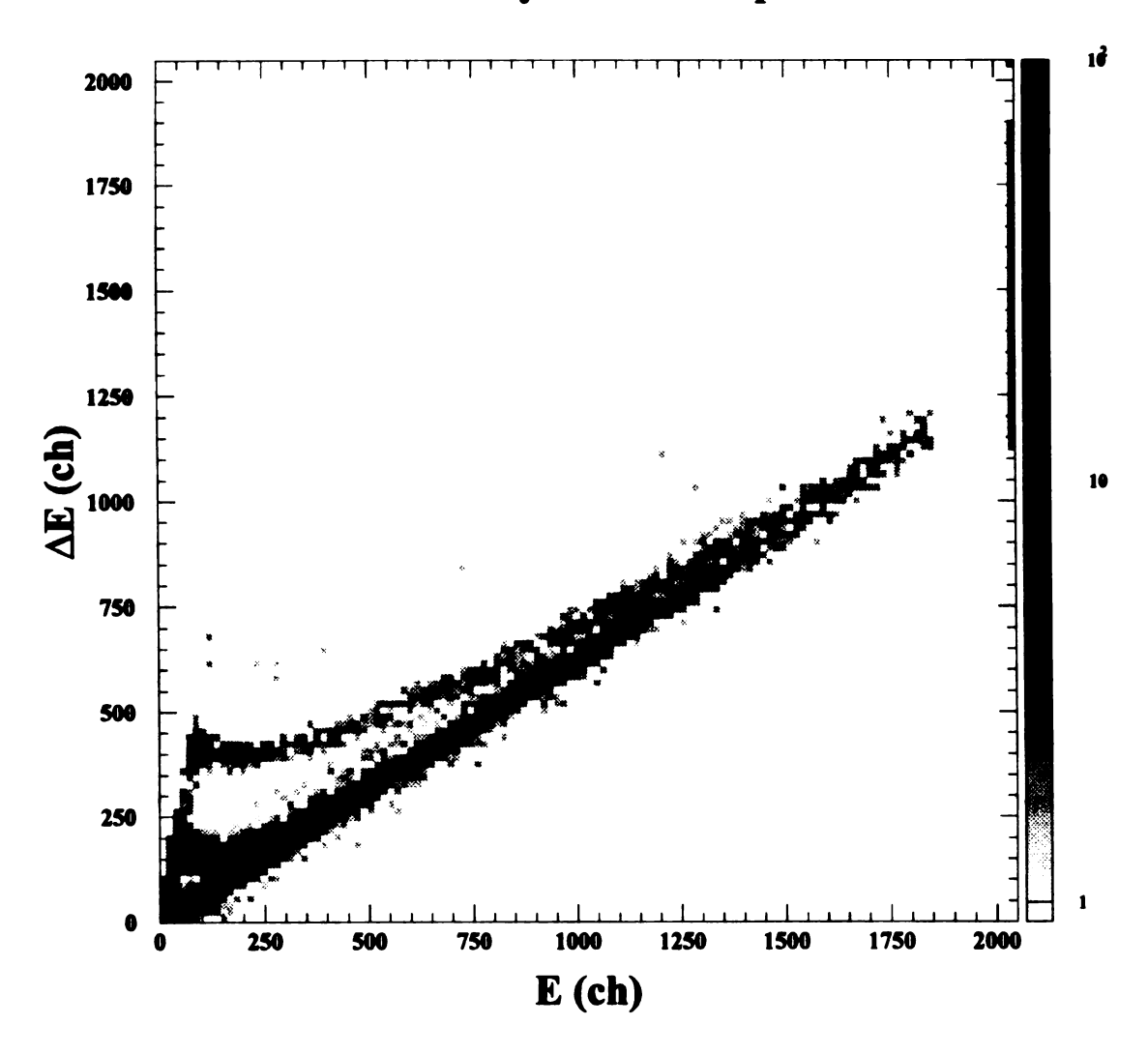


Figure 2.6: Typical raw spectrum from a Forward Array phoswich for Ne + Al at 150 AMeV. Lines for particles of Z=1 - 3 are identified with isotopic resolution for Z=1.

of 21 parallel copper strips, each encircling the volume of the chamber between the Frisch grid and the cathode. The strips are connected by 21 1.55 M $\Omega$  resistors creating a 21 stage voltage drop between the cathode potential and ground. A schematic view of a BCC chamber is given in Figure 2.7.

Positive ions entering the chamber through the front window will produce electronion pairs as they lose energy along their trajectory. The functional dependence of the rate of energy loss on the distance of penetration is the well known Bragg curve. It typically has a strong peak close to the end of the particle track.

The electron-ion pairs created by the ionizing particle will drift along the electric field lines towards opposite sides of the detector. The negative signal from the anode is fed into a charge-sensitive pre-amplifier and integrated. The resulting signal is supplied to a shaping amplifier that provides a fast (differentiated) output and a slow (2 x differentiated and 2 x integrated) output. If the ionizing particle stops in the gas volume of the BCC detector, the peak height of the fast output is proportional to its charge whereas the slow one represents the total energy. For particles not stopping inside the BCC counter the slow output is still proportional the energy loss in the detector volume. In the latter case that signal together with the corresponding signal from the fast plastic behind the BCC can be used for  $\Delta E$  vs. E particle identification. Since there are 170 phoswich counters with BCCs in front of them, there are effectively 170 BCC/fast plastic telescopes as well. Figure 2.8 shows such a spectrum. The lowest Z line above the noise is for He ions, the one above it for Li. Again, with more statistics higher Z lines can be observed. The bin width here is 16 FERA channels in x-direction on 32 Silena channels in y-direction.

Originally the BCCs were intended to be operated with 500 Torr of P5 gas (95% argon, 5% methane), and with -1200 V and +500 V on the anode and cathode re-

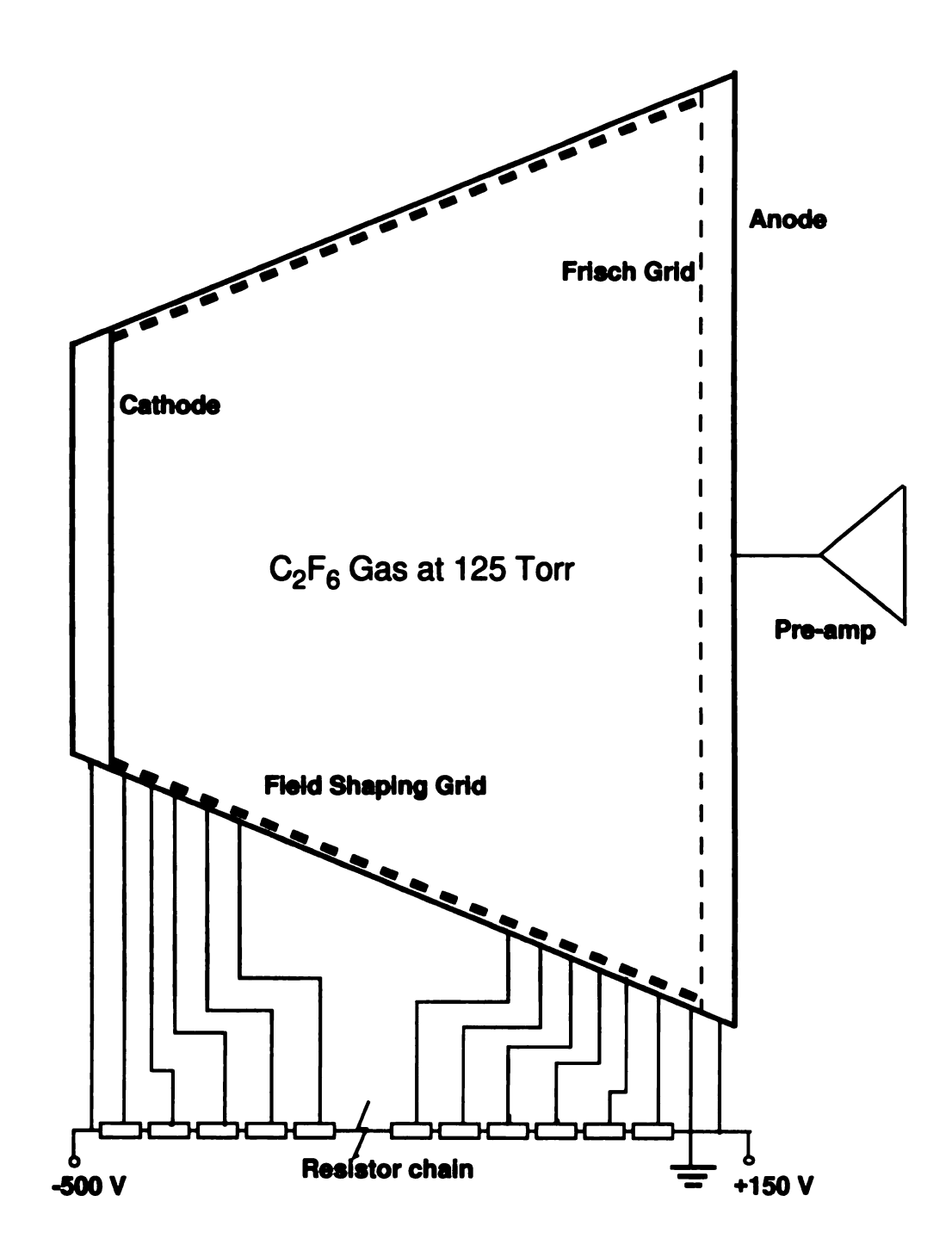


Figure 2.7: Schematic of the MSU  $4\pi$  Array Bragg curve counter.

## **BCC** vs. Fast Plastic Spectrum

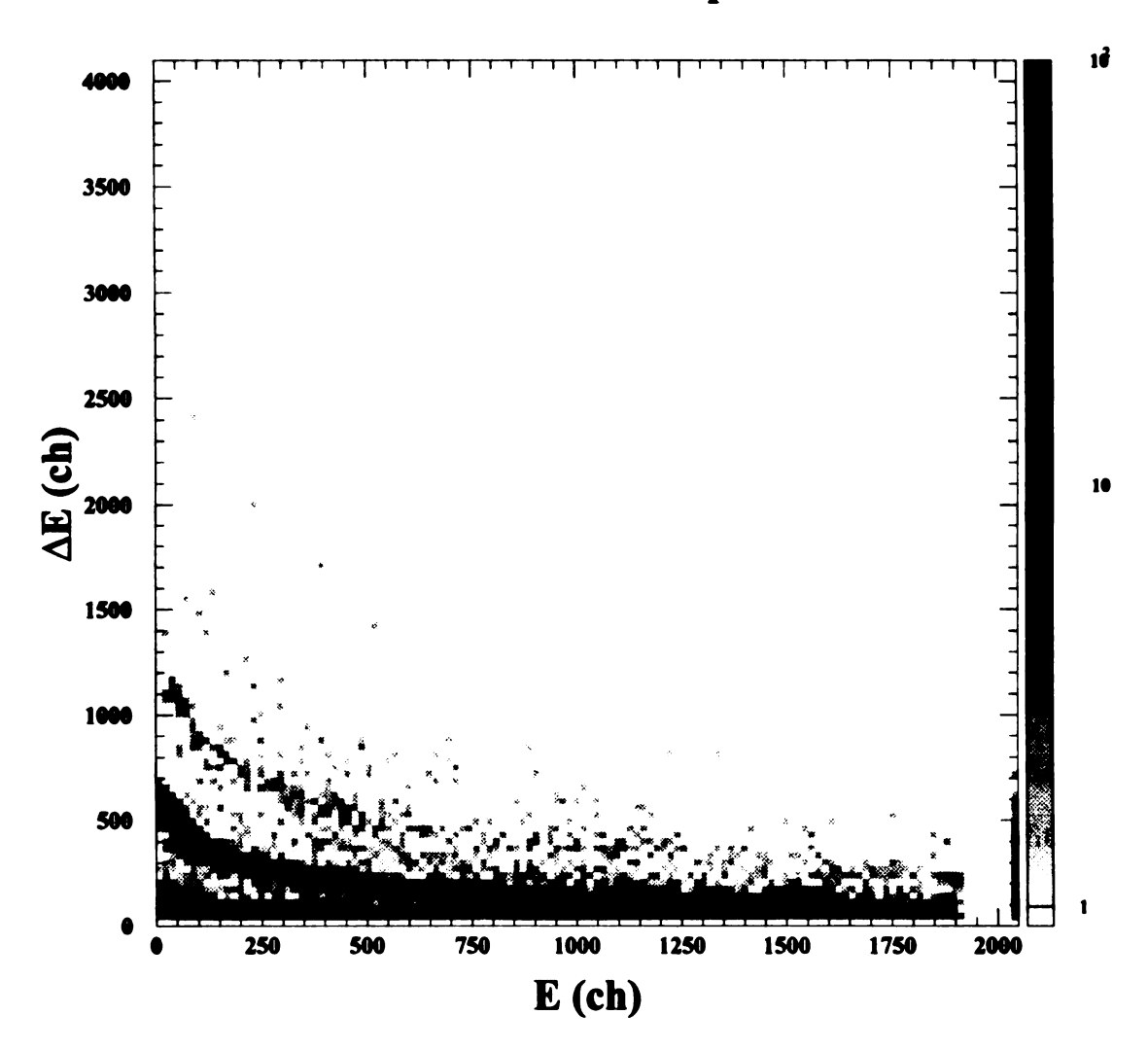


Figure 2.8: BCC vs. fast plastic spectrum for Ne + Al at 90 AMeV. The lowest Z line above the noise is for helium, the one above for lithium.

Table 2.3: Specifications of the Bragg curve counters.

Characteristic	BCC vs. FP	BCC E vs. Z
Polar Angle region (°)	18 - 162	18 -162
Solid Angle coverage (%)	84	84
Z identification	2 - 18	3 - 18
Energy Threshold (AMeV)		
Lithium	4.0	2.0
Boron	5.0	3.0
Carbon	5.5	4.0

spectively. For the present experiment however, the BCCs were filled with 125 Torr of  $C_2F_6$  and operated at -500 V and +150 V. The lower gas pressure puts less strain on the front windows and the heavier gas compensates for the loss in stopping power. Since for such a light system  $^{20}Ne + ^{27}Al$  heavy fragments are not expected, only the BCC/fast plastic identification method was used. A summary of the characteristics of the BCCs is given in Table 2.3.

### 2.2.3 Phoswich Calibration

Because of the large number of detectors in the  $4\pi$  Array, a method had to be developed to keep the time needed for detector calibration within reasonable limits. The basic idea is [Cebr 90, Cebr 92] to create two-dimensional calibrated templates for each of the detector systems to which all the individual  $\Delta E$  vs. E spectra are then mapped. The template consists of a set of gate lines for the observed Z lines to which the spectra can be matched as well as calibration curves for the Z lines that are used to map matched channel numbers to incident particle energies.

To obtain the gate lines a typical spectrum is transformed so that the punch-in line and neutral line coincide with the y and x axis. Then lines are drawn on either side of the Z lines in that spectrum. These lines are the gate lines. The transformation

equations are

$$CH_f = (\Delta E_{ch} - Y_0) - (E_{ch} - X_0)M_n$$

$$CH_s = (E_{ch} - X_0) - (\Delta E_{ch} - Y_0)/M_p, \qquad (2.1)$$

where  $\Delta E_{\rm ch}$  and  $E_{\rm ch}$  are the fast and slow raw channel numbers,  $M_n$  and  $M_p$  are the slopes of the punch-in and neutral line and  $X_0$  and  $Y_0$  are the coordinates of the intersection of the two lines.  $CH_f$  and  $CH_s$  are the transformed fast and slow channel numbers.

Using these gate lines one can assign each point in the mapped spectrum an A and Z value. The atomic mass number used is the most common isotope for the cases where isotope resolution is not given from the gate lines. All phoswich raw spectra can now be gain matched and transformed to fit the template. The matching parameters and the gains are stored in a file and are used in further steps of the data analysis. Figures 2.9 and 2.10 display the gate lines for the Ball and Forward Array phoswiches used in this experiment.

The second ingredient for the energy calibration are response functions that map the transformed fast and slow channel numbers to energies deposited in the corresponding plastic scintillator. These response functions were determined from a previous calibration experiment [Cebr 90], and are of the form:

$$CH_s = aE_s^{1.4}/A^{0.4}Z^{0.8}$$
  
 $CH_f = bE_f^{0.5} - c.$  (2.2)

The inverse of these equations converts the transformed fast and slow channel numbers into the energy deposited in the corresponding plastic. The arbitrary constants a,b, and c are determined by fitting the lines following this functional form to the same representative spectrum used to create the gate lines. The final response functions used for the Ball are shown in Figure 2.11.

## **Main Ball Gatelines**

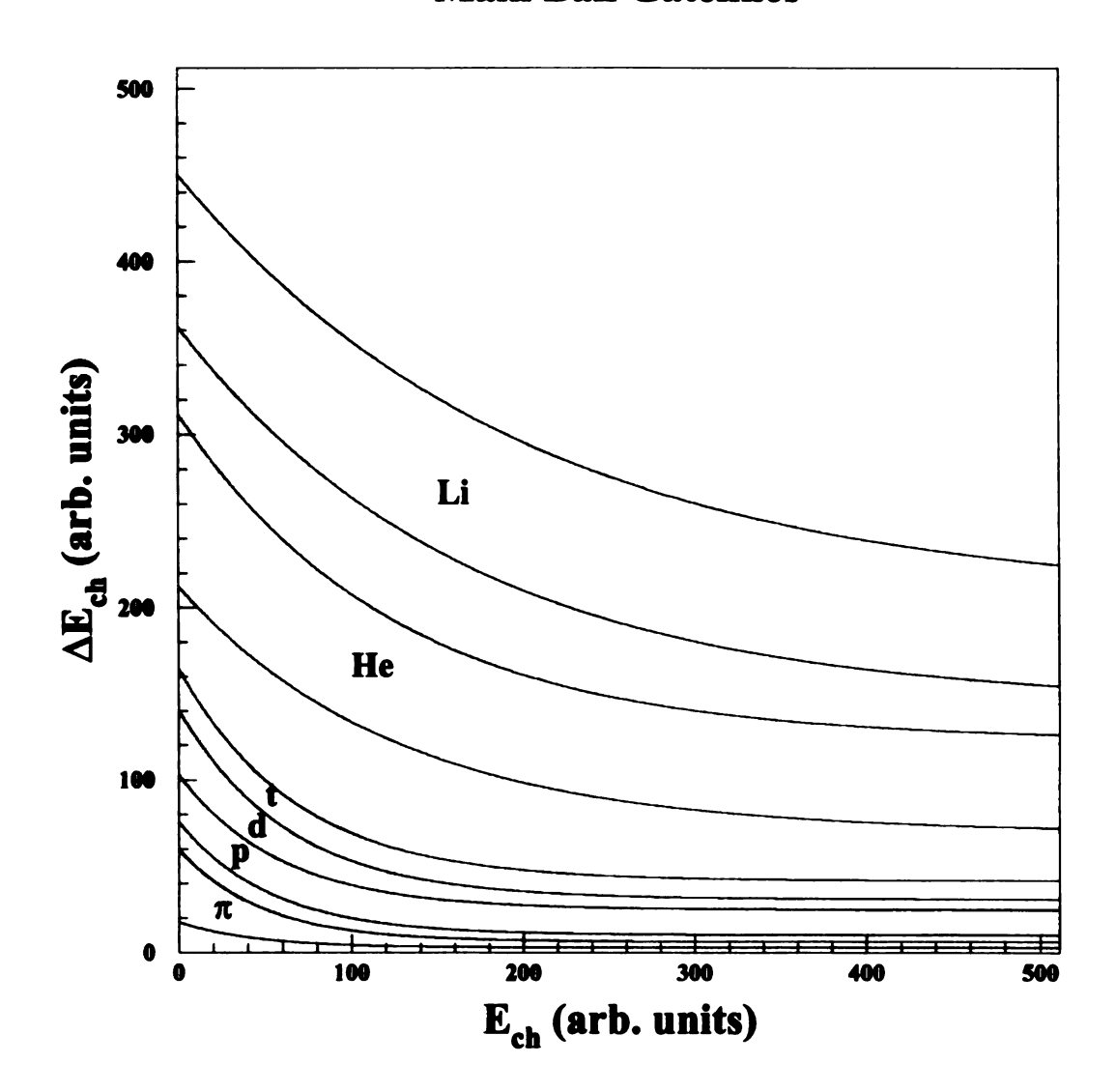


Figure 2.9: The particle gate lines for  $\pi$ , p,d,t and Z = 2 - 3 for the Ball phoswich detectors.

## **Forward Array Gatelines**

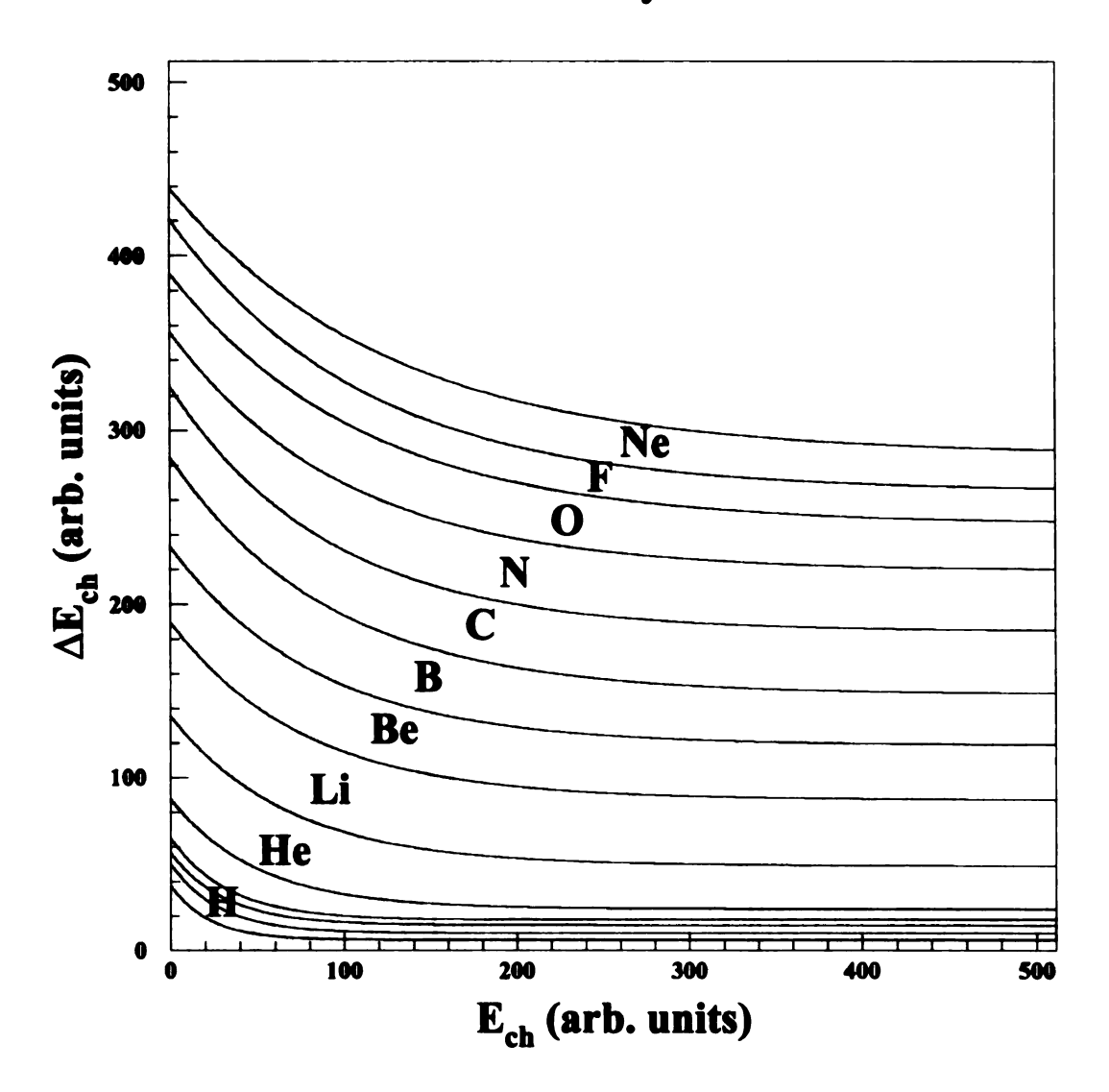


Figure 2.10: The particle gate lines for p,d,t and Z=2 - 10 for a Forward Array phoswich detector.

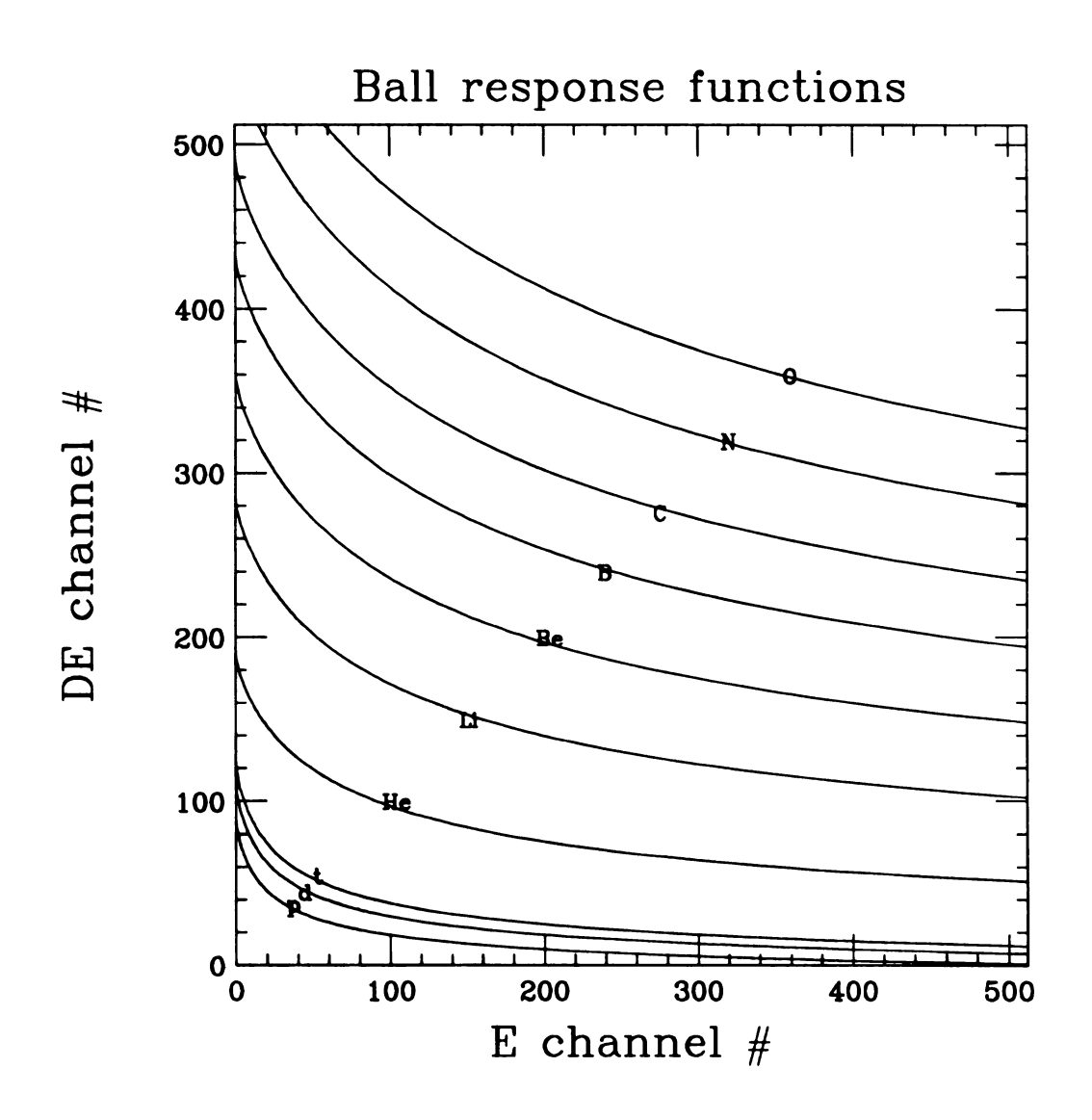


Figure 2.11: The response functions for p,d,t and Z = 2 - 5 for a Ball phoswich.

As a last step one has to obtain the value of the incident energy of a given particle by simply looking up the well known energy loss curves for that particle type. In our case the energy loss program DONNA was used to calculate  $\Delta E$  and E vs.  $E_{inc}$  providing it with the densities, composition and thickness of the detector media.

To summarize, calibrated templates are generated for the Ball and Forward Array detectors to which all raw phoswich spectra are matched. From this template look-up tables are made which map raw channel number into particle type and incident energy. The angles of the detected particles are assigned as the geometric mean angle of the corresponding detector. Using these tables, the raw data tapes are sorted onto "physics" tapes which contain information regarding the event multiplicity and the atomic mass number, charge,  $\Theta$ ,  $\Phi$ , and kinetic energy of each of the particles in the event.

#### 2.2.4 BCC Calibration

Since the nature of the BCC vs. fast plastic spectra is also  $\Delta E$  vs. E, the calibration of those is accomplished in a very similar way to the phoswich detectors. The main differences are that the gate lines as well as the response functions are generated from a known functional form and since both  $\Delta E$  and E originate from separate signals no transformation of the spectra is necessary. The response for the fast plastic is identical to the slow plastic in the phoswich calibration, since here it is the stopping detector. The form is

$$CH_f = \alpha E_f^{1.4} / (A^{0.4} Z^{0.8}).$$
 (2.3)

During a field test using a BCC with P5 gas and corresponding specifications listed in Table 2.4 [Cebr 91] the response function for the BCC was originally determined

Table 2.4: Specifications of the Bragg curve counters.

Characteristic	BCC vs. FP	BCC E vs. Z
Polar Angle region (°)	18 - 162	18 -162
Solid Angle coverage (%)	84	84
Z identification	2 - 18	3 - 18
Energy Threshold (AMeV)		
Lithium	4.0	2.0
Boron	5.0	3.0
Carbon	5.5	4.0

to be linear

$$CH_{BCC} = \beta E_{BCC} \tag{2.4}$$

(see Figure 2.12). In that test run, it was determined that the BCC energy response was independent of particle type. However, in the present experiment, it is necessary to introduce a charge dependence into the energy calibration as an exponent in the energy term.

$$CH_{BCC} = \beta E_{BCC}^{C(Z)} \tag{2.5}$$

In the same fashion as for the phoswiches a common template is made to which all the BCC vs. fast plastic spectra are gain matched. The energy loss calculations are performed using the ELOSS program. The template used in this experiment is shown in Figure 2.13.

### 2.3 Charged Pion identification

The positively charged pions were detected using  $\Delta E$  vs. E particle identification (PID) in the fast/slow plastic phoswich counters of the main Ball, similar to the method used by the Plastic Ball group [Bade 82, Gutb 89]. In order to distinguish

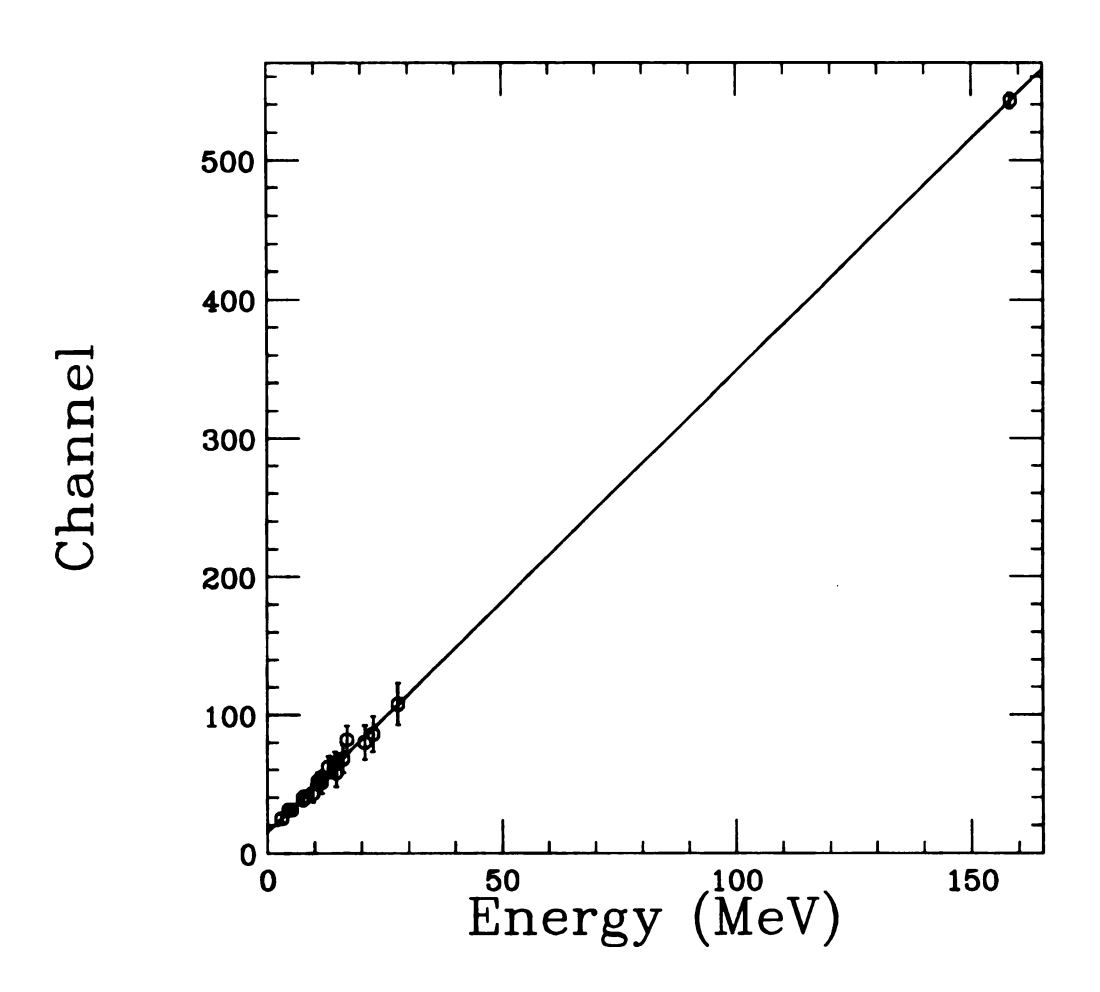


Figure 2.12: Bragg curve response function from test run.

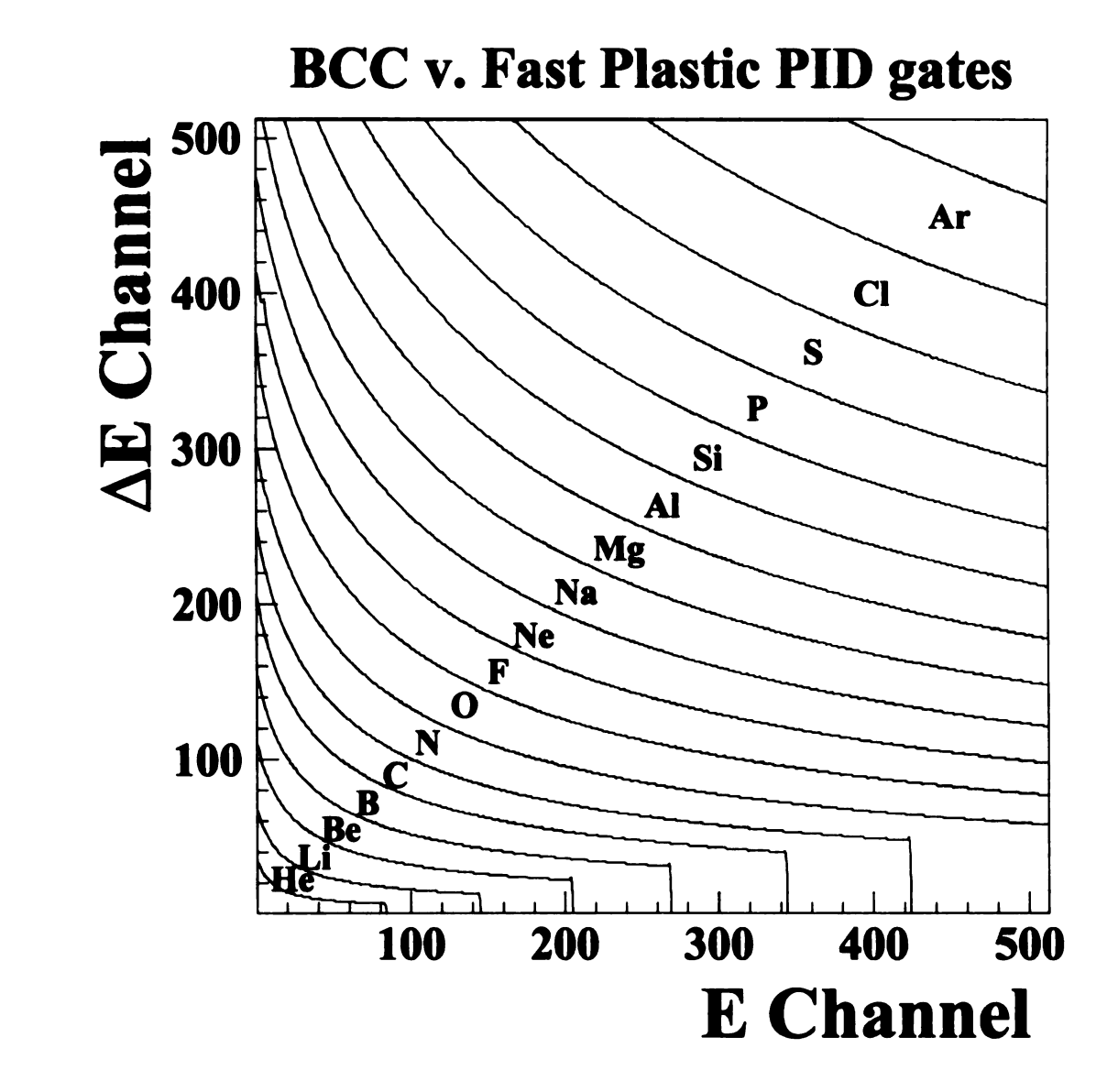


Figure 2.13: Template for a BCC vs. Fast Plastic spectrum.

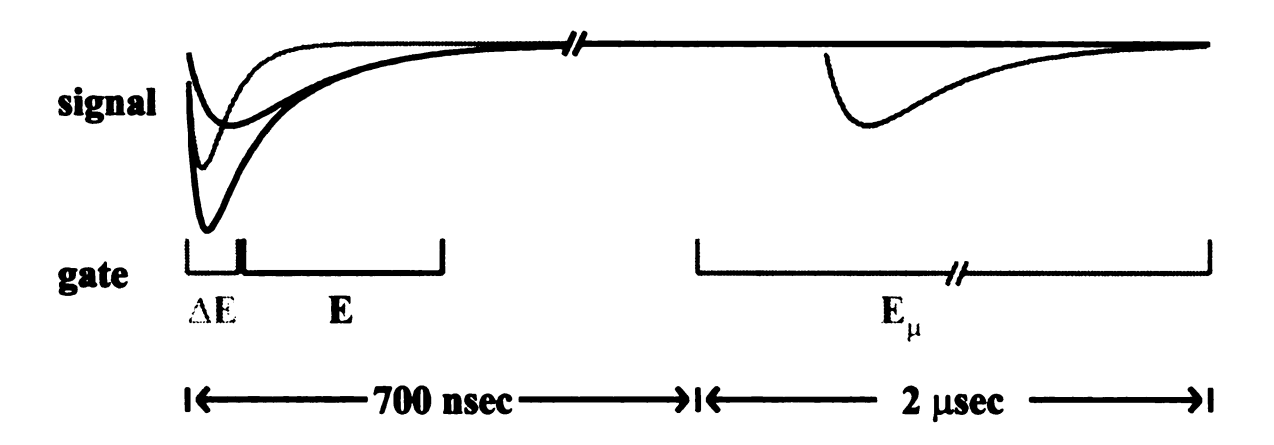


Figure 2.14: Diagram of the phoswich signal and gates for an incident pion.

real pions from background we used the dominant decay of positively charged pions,

$$\pi^+ \to \mu^+ + \overline{\nu_{\mu}} \qquad \lambda = 26 \text{ nsec}, \text{ p}_{\text{max}} = 30 \text{MeV/c}$$
  
$$\mu^+ \to e^+ + \overline{\nu_e} + \nu_{\mu} \quad \lambda = 2.2 \text{ } \mu\text{sec}, \text{ p}_{\text{max}} = 53 \text{MeV/c}.$$
 (2.6)

The energy loss of the positron from the  $\mu^+ \to e^+$  decay was recorded using an additional bank of QDCs (also Lecroy FERA 4301B) with a gate of 2  $\mu$ sec width that was delayed by 700 nsec with respect to the  $\Delta E$  gate (See Figure 2.14). Any hit in that delayed gate will be called an  $E_{\mu}$  gate, irrespective of the particle it was associated with (if any). In order for a hit in the  $\Delta E$  vs. E  $\pi$  particle identification gate to be identified as a real pion we require a coincidence with an  $E_{\mu}$  gate. In a test run where the  $E_{\mu}$  signal was recorded for only 16 detectors, the time signal from the decay was also recorded. In that case an exponential fit to the time spectrum resulted in  $\lambda = 2.2 \pm 0.4 \mu$ sec.

The resulting pion identification is demonstrated in Figures 2.15 and 2.16. The upper panes in both figures show gain matched and added  $\Delta E$  vs. E spectra for all detectors in the indicated polar angle range. In the lower pane the projection of a

vertical slice of the 2-dimensional data is shown for E channels between 100 and 200. In the inclusive distributions (Figure 2.15) an expected line in the pion identification gate is completely hidden by the background. The cut at the indicated E channels (lower right) reveals no structure in the resulting  $\Delta E_{ch}$  distribution in the area where a pion peak should arise. However, if one requires a coincident signal in the delayed  $E_{\mu}$  gate (Figure 2.16) the same data reveals a clear line below the protons with a very small contribution from background signals. The same cut as for the inclusive data now shows a strong peak at the expected position.

Due to the unusually long gate ( $2\mu$ sec) for the type of QDC used (Lecroy FERA 4301B, rated up to 512 nsec gates), one can expect several problems in the pion identification method.

The first is false signals in the delayed gate that arise from random noise accumulation, accidental pile up from uncorrelated events and possibly large initial  $\Delta E/E$  signals that might leak into the delayed gate. The random noise contribution is small for low pion energies and might increase somewhat for the higher energies, as can be seen from the lower panel in Figure 2.16. The polar angle dependence of  $E_{\mu}$  gated PID distributions indicates the importance of accidental pile up, since at forward angles many more protons and neutrals have an associated  $E_{\mu}$  signal than at backward angles. This indicates that false  $E_{\mu}$  signals are mainly related to high count rates in the phoswich detectors. In fact, at the very forward angles in the Ball (rings 1 and 2 at 23° and 32°) the pions cannot be separated from the background. The total polar angle coverage for pion identification is therefore from 46° to 157° in the laboratory frame.

On the other hand, the method used will misidentify some real pions as noise since the finite width and position of the  $E_{\mu}$  gate only captures those decays that fall within

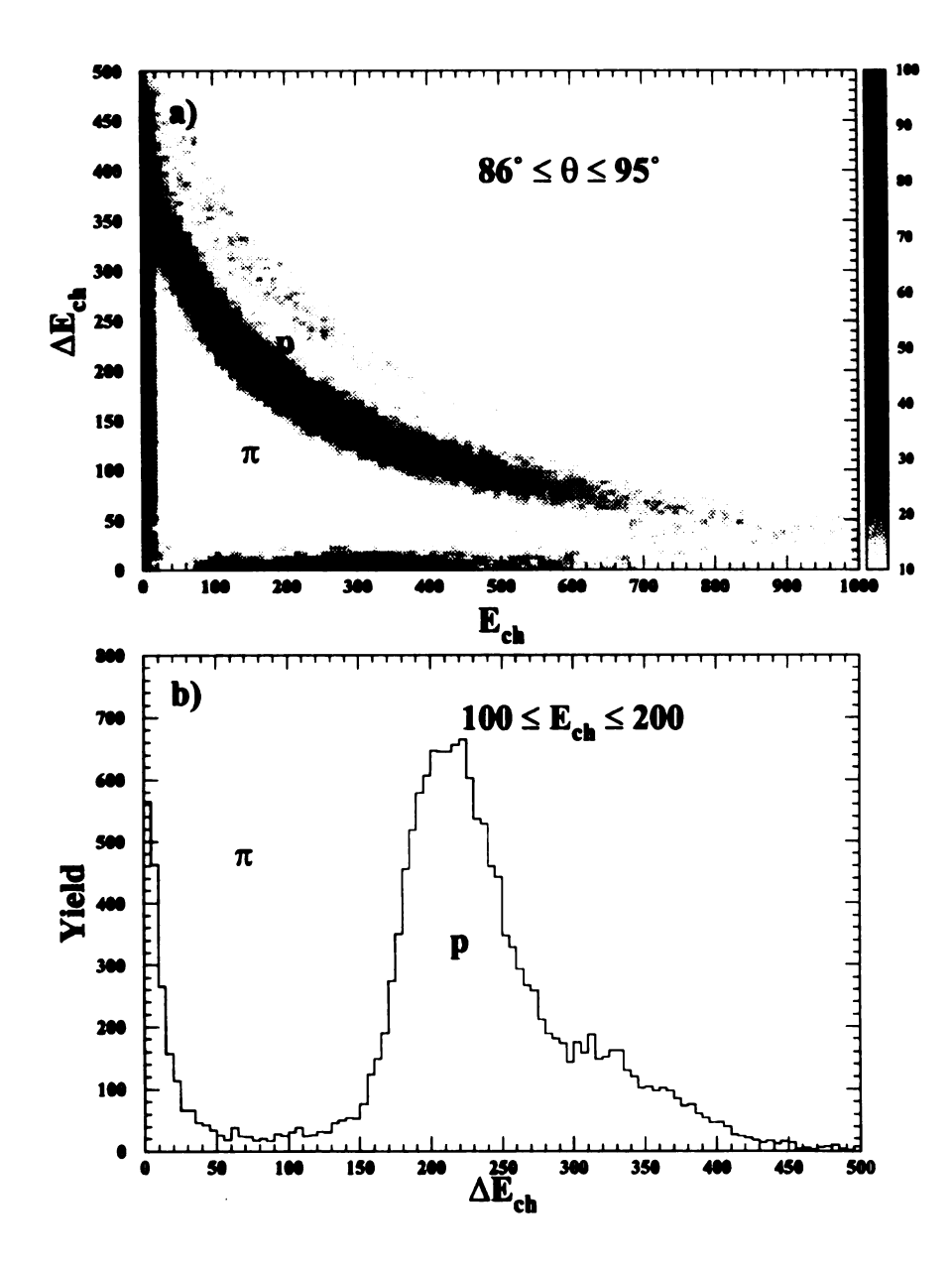


Figure 2.15: (a) Inclusive Ball  $\Delta E$  vs. E spectrum summed over all detectors in the indicated polar angle range and (b) resulting  $\Delta E_{ch}$  distribution

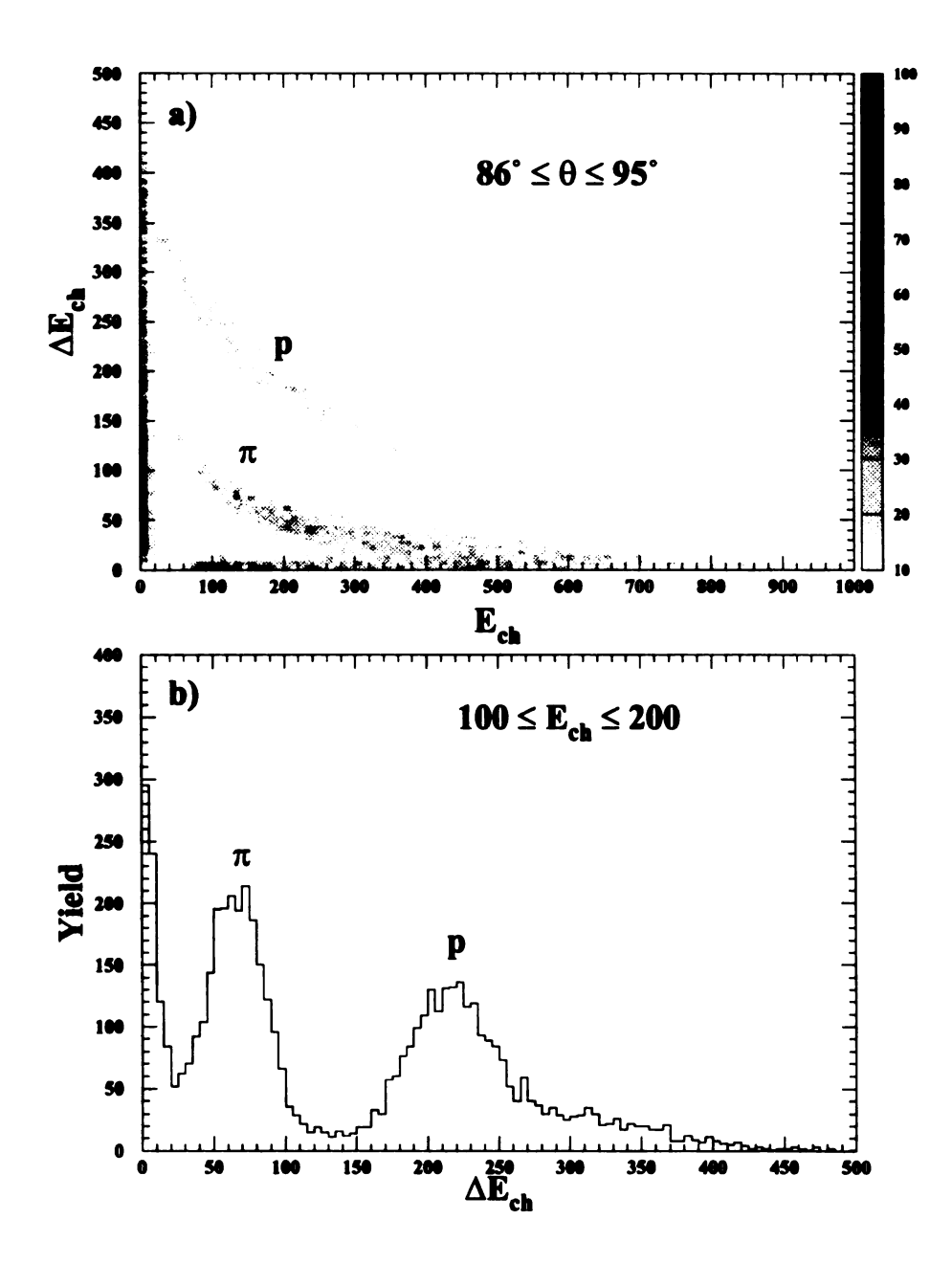


Figure 2.16: Same as Figure 2.15 with  $E_{\mu}$  gate applied.

the gate. Also, depending on the stopping position of the muon, some positrons might escape the detector without leaving enough energy. This will be especially important for pions with low incident energy, since these will not penetrate the phoswich deep enough to enable the resulting positron to deposit enough energy in the detector to be detected. The low energy threshold for the muon to be detected was determined to be about 5 MeV.

An additional problem arising from the long gate is related to the charge integrating ADC used to record the  $E_{\mu}$  signal. The FERA measures charge by charging a capacitor with the input pulse and discharge it through an RC circuit. Since the discharge process starts immediately after the gate opens (or the signal arrives) a variation of measured charge with arrival time will occur. That variation is compensated for gate widths up to 500 nsec and can be adjusted for gate widths up to 1  $\mu$ sec. Since that gate width is too short to capture a significant amount of the decaying muons it was decided to compromise the constancy of the  $E_{\mu}$  signal and use a  $2\mu$ sec gate. For gate widths above  $2\mu$ sec all signals arriving more than  $2\mu$ sec before the end of the gate are completely decayed and therefore not recorded.

In order to overcome the above mentioned problems we apply lower  $E_{\mu}$  cuts for several detectors and exclude the first two rings of Ball detectors (23° and 32°) for pion identification. The resulting pion identification is demonstrated in Figures 2.17 and 2.18. In Figure 2.17 we show the number of hits in a given PID gate as a function of the ring number, in the Ball, that was hit. The PID gates are for neutrals (n), pions  $(\pi)$ , between pions and protons  $(\pi - p)$  and protons (p) which includes both regions adjacent to the pion PID gate (see Figure 2.9). The solid histograms represent the inclusive data, i.e., all hits in the corresponding PID gate are accepted. Note that there is no obvious difference between the pion and the data in the two neighboring PID gates. The triangles show the data if a coincidence with an  $E_{\mu}$  signal is required.

Now the slope for the data in the pion PID gate is very different from the ones in the other PID gates. Both the inclusive and the gated data are area normalized to one by fitting an exponentially decaying function to the data and integrating the area below that function. In Figure 2.18 the inverse slope and the total area for both inclusive (squares) and gated (triangles) data are displayed in the upper two panels. As could already be seen in Figure 2.17 the inverse slope for the pion data with an  $E_{\mu}$  gate is much larger than the one for the inclusive data, whereas the other PID gates show no significant change in the slope whether the  $E_{\mu}$  gate is applied or not. From that we conclude that for hits in the pion PID gate a coincident  $E_{\mu}$  signal is mainly due to the decay products, whereas for neutrals and protons the number of coincident  $E_{\mu}$  signals is a constant fraction of the total number of counts in that gate. This is further demonstrated in the bottom panel of Figure 2.18 where the ratio of the total yield with a corresponding  $E_{\mu}$  signal and the inclusive yield is shown. That ratio is at least a factor of two larger for pions than for the other particle types.

In summary, the detection efficiency for positively charged pions depends not only on polar angle but also on the energy of the incident pion. The most forward angles do not provide a clean separation for pions from background. The yield for low energy pions will be underestimated due to the method of identification. Absolute cross section cannot be obtained at the current level of analysis. The total polar angle coverage is from 46° to 157° in the laboratory frame.

## 2.4 Pion Energy Calibration

In order to obtain an energy calibration, one could simply use equation 2.2 with the appropriate mass scaling for the pion mass (A = 0.15). This would imply a factor of about 1.7 more light produced for a pion, than for a proton depositing the same

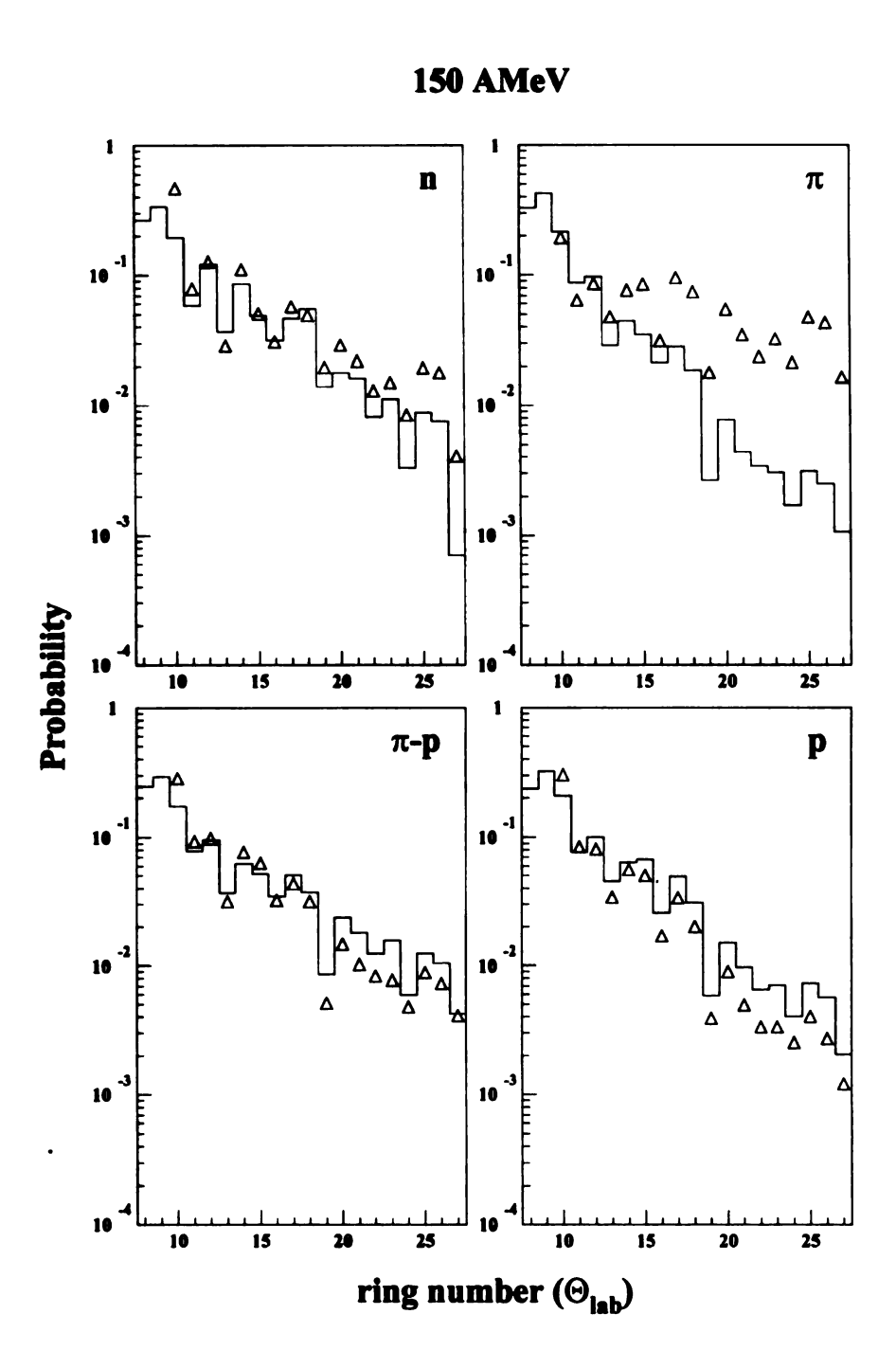


Figure 2.17: Inclusive (histograms) and  $E_{\mu}$  gated (symbols) probability distributions for detector hits in the main Ball as a function of ring number.

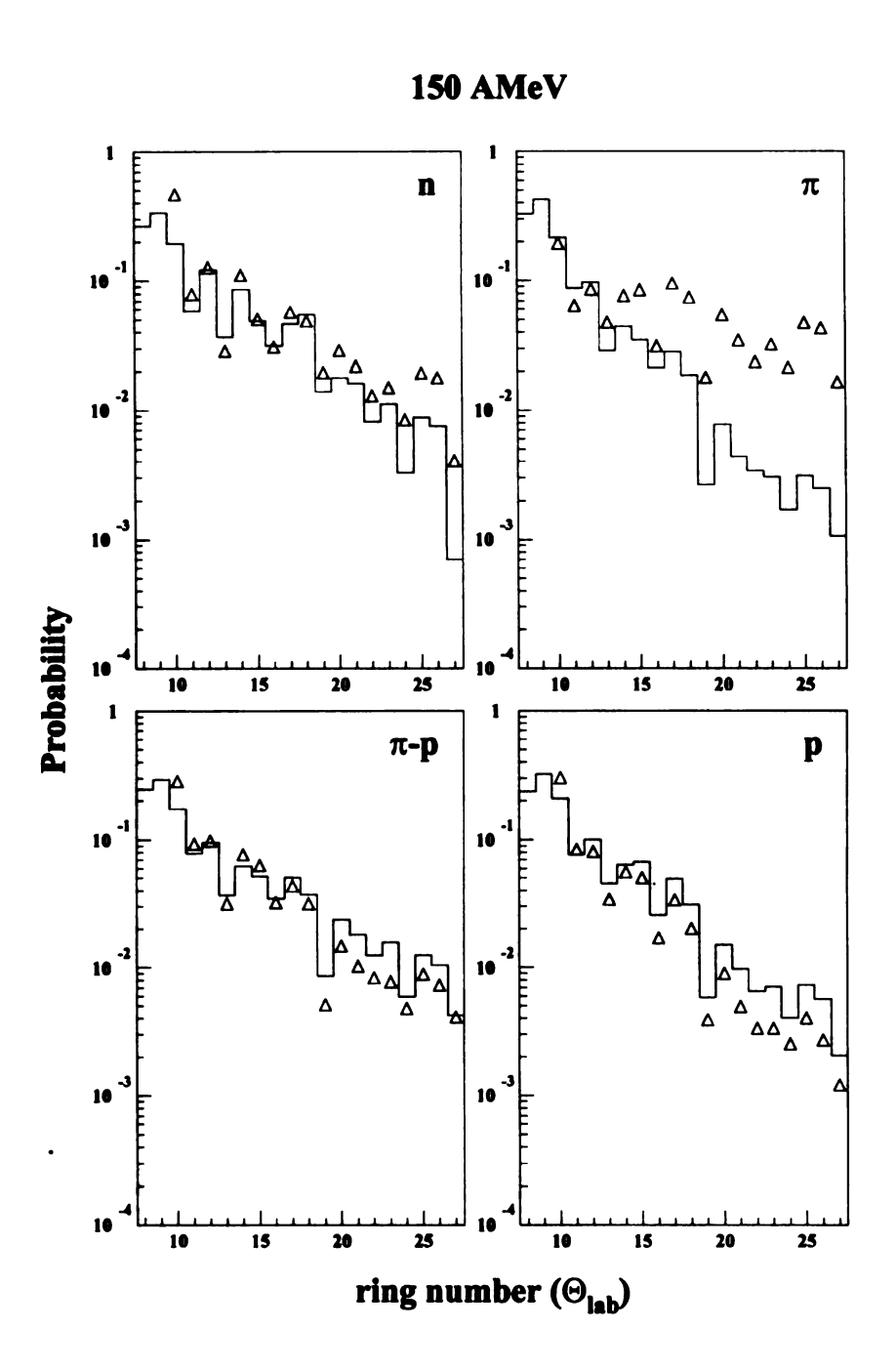


Figure 2.17: Inclusive (histograms) and  $E_{\mu}$  gated (symbols) probability distributions for detector hits in the main Ball as a function of ring number.

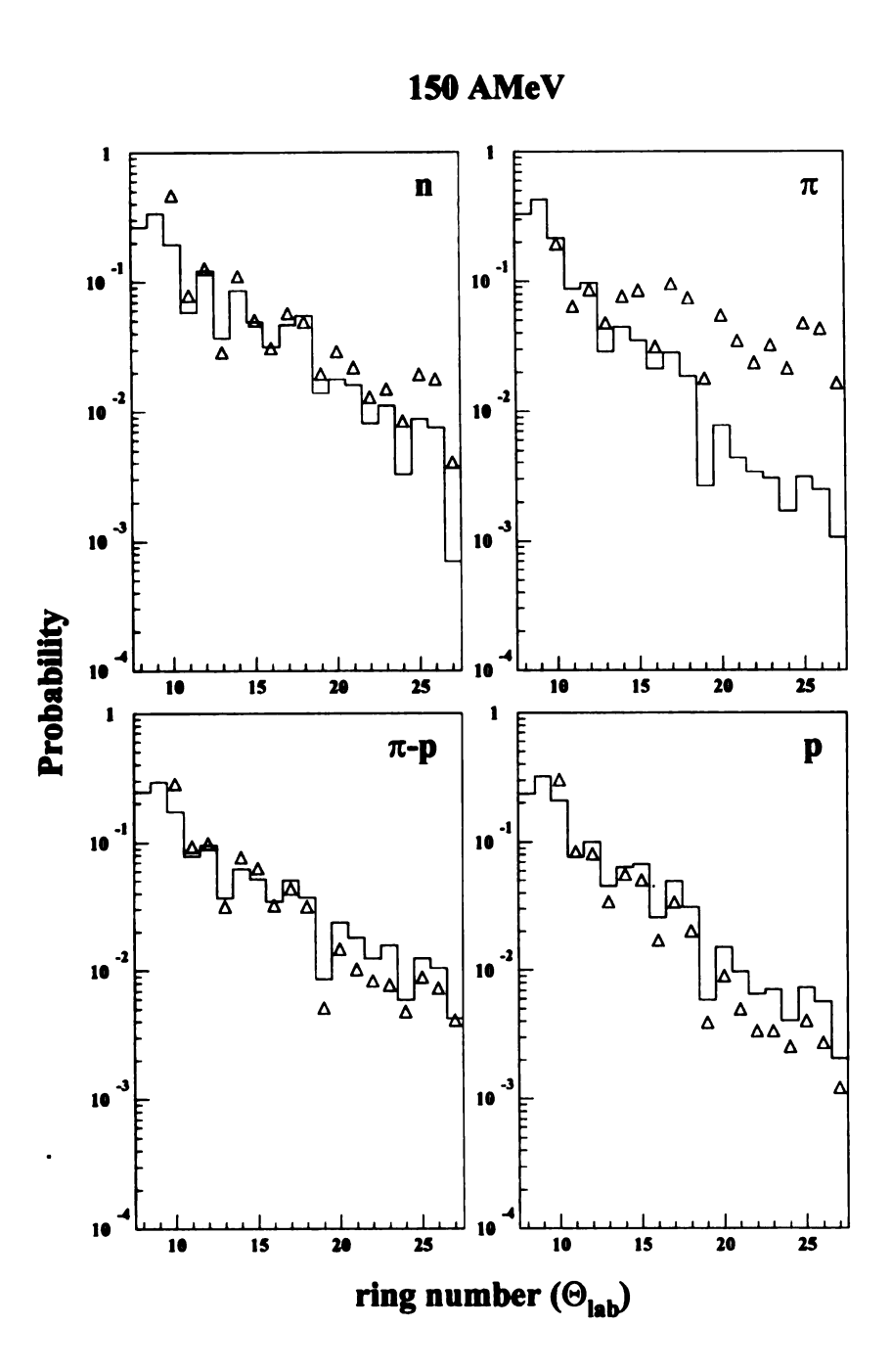


Figure 2.17: Inclusive (histograms) and  $E_{\mu}$  gated (symbols) probability distributions for detector hits in the main Ball as a function of ring number.

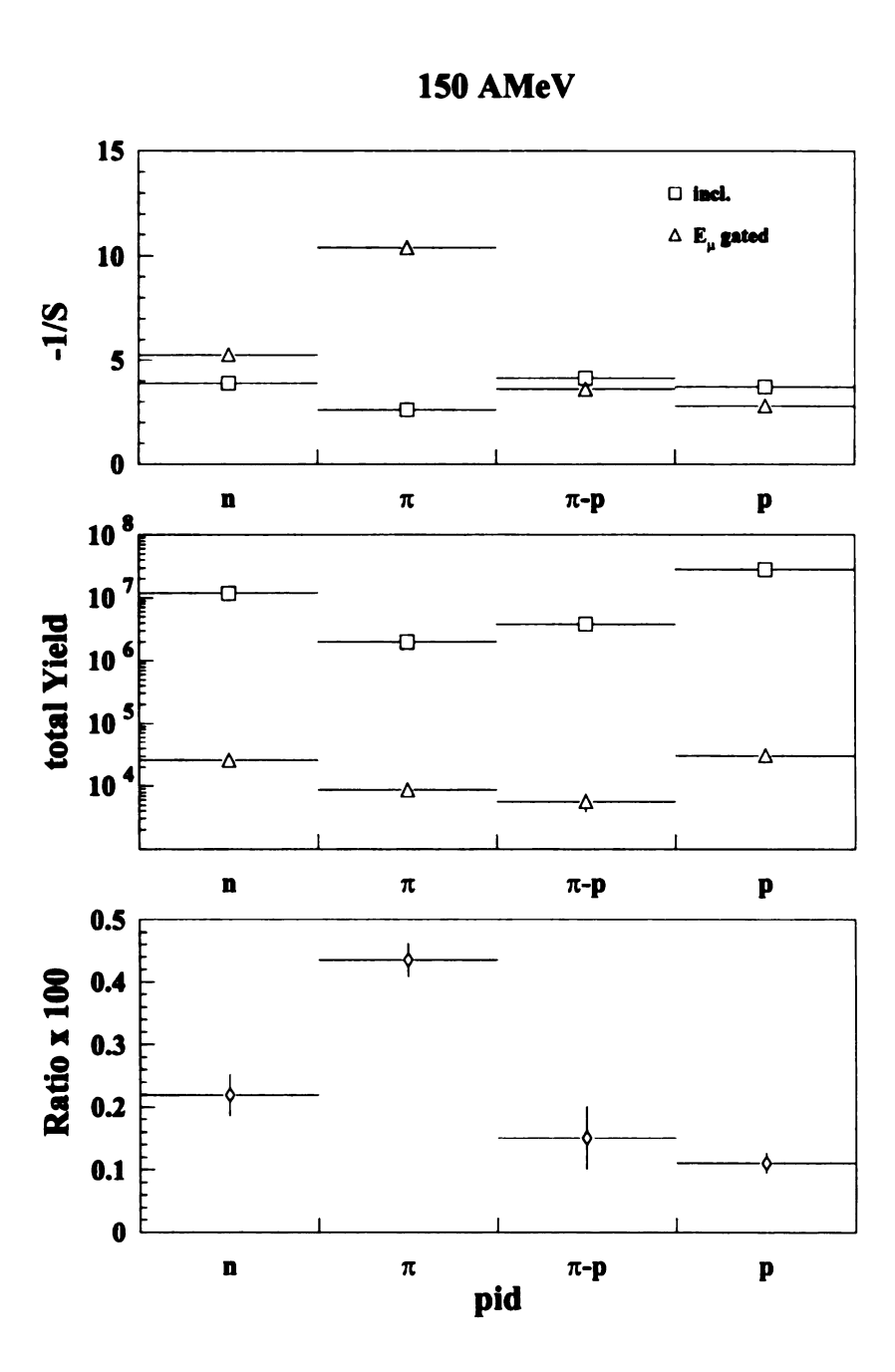


Figure 2.18: Inverse slope, total yield and ratio for detector hits in the main Ball, inclusive and  $E_{\mu}$  gated.

energy in the detector. This is clearly too high, since even an electron produces only about 1.6 times as much light as a proton for a deposited energy of 160 MeV in a plastic scintillator [Birk 64]. Obviously the well known energy calibration of the  $4\pi$  Array phoswich detectors for particles with mass number  $A \geq 1$  cannot be extrapolated to pion masses. Figure 2.19 shows the energy calibration for protons and pions obtained by the Plastic Ball group [Bade 82]. The two curves show a very similar response, with slightly more light produced from pions than from protons for the same deposited energy. Since the stopping plastic scintillator in the Plastic Ball is very similar to the one used in the MSU  $4\pi$  Array, the pion kinetic energies are calibrated relative to the well known proton calibration. The resulting energy vs. light curve is shown in Figure 2.20 as the solid curve. The dot-dashed curve is the proton response and the dashed line is obtained by using the mass scaling from equation 2.2.

#### 2.5 The Experiment

The experiment was performed in February 1993 at the National Superconducting Cyclotron Laboratory (NSCL) at Michigan State University (MSU). The K1200 superconducting cyclotron was used to accelerate  $^{20}\mathrm{Ne}$  beams at  $\mathrm{E}_{\mathrm{beam}}=90,\,110$  and 150 AMeV that bombarded a 5 mg/cm²  $^{27}\mathrm{Al}$  target. The average beam intensities were between 10 and 40 pA , resulting in about 2000 triggers per second, depending on the hardware trigger condition.

The analog data from all the phoswich detectors are electronically split three ways to extract the  $\Delta E$  and E information and to provide additional trigger information. The  $\Delta E$  and E signals are delayed and fed into 16 channel Lecroy 4301B FERAs. The trigger signal again split two ways, with one of the signals being supplied to an

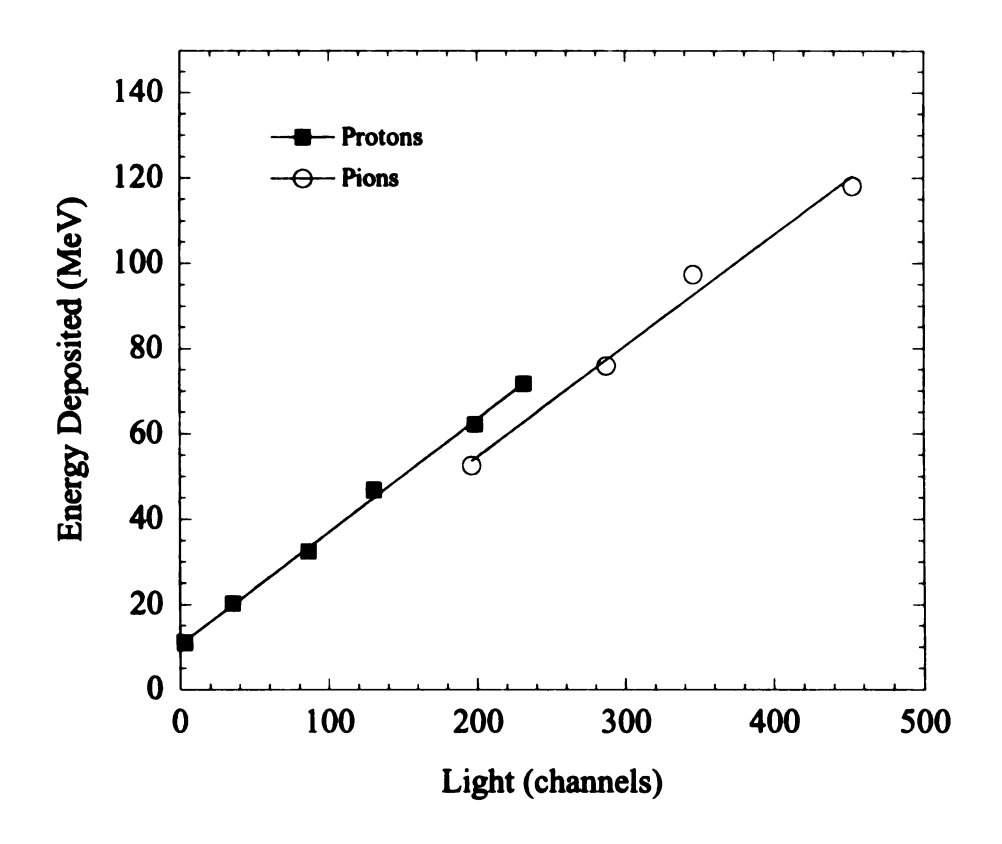


Figure 2.19: Pion and proton energy calibration from the Plastic Ball. From [Bade 82].

additional bank of FERAs that record the  $E_{\mu}$  signal. The other signal is fed into 16 channel Phillips 7106 discriminators where sum and individual outputs are provided. The individual channel outputs are again delayed and fed into 16 channel Lecroy 4303 Time-to-FERA converters (TFCs) that provide an analog time proportional signal to another bank of FERAs. The sum outputs are fed into two EG&G octal constant fraction discriminators CCF 8000. One of these provides scaler information for the detector subsystems (BALL and FA), whereas the other is used to determine the user selectable trigger condition (MASTER). The trigger condition consists of the detector subsystem (or a combination thereof) and a hit multiplicity. The triggers used in this experiment were FA2 (two hits in the forward array), B2 (two hits in the main Ball) and B3 (three hits in the main Ball). The MASTER signal in coincidence with a signal from the data aquisition module, indicating its "readyness" to accept data make up the MASTER.LIVE signal. Another sum output from the Phillips discriminators in coincidence with MASTER.LIVE is used to provide individual gates to the  $\Delta E$  and E FERAs for the main Ball and Forward Array subsystems. The Silenas (BCCs) and the bank of FERAs for the E $\mu$  signal are both gated with appropriate signals derived from MASTER.LIVE.

The digitized data from the FERA QDCs and Silena ADCs are read out by ECL line using a VME based data-bus to buffer-memory interface module and stored in local VME memory. From there it is accessed by an INMOS T-800 transputer linked to a SUN Sparc workstation. The VME transputer packs the data and supplies it to a host process running on the Sparc workstation. The host process on the SUN feeds the data to a general purpose router (also on the SUN) which in turn distributes the data to a number of consumers. The most important consumer is the taping process, which writes the data to 8mm Exabyte magnetic tapes. The other important consumer is a program that supplies the data to consumers running on

different hosts over the Ethernet. Two such consumers are the online data display and analysis program XSARA and a scaler program, both running on VMS DEC Alpha computers. For a more detailed description of the data aquisition system see References [Vand 94, Vand 91].

Over the time of 10 days beam time we collected a total of several billion raw events. The analysis was done using only the B2 trigger data due to some detector problems in the initial phase of the experiment (B3 trigger). In order to reduce analysis time two types of physics tapes were prepared. The first includes about 600000 events of inclusive data for each beam energy and is used to get all distributions not involving pions. The second type consists of all events from all raw tapes that had an  $E\mu$  signal anywhere in the event (not necessarily in coincidence with a pion). The total numbers of pions for the B2 trigger are summarized in Table 2.5.

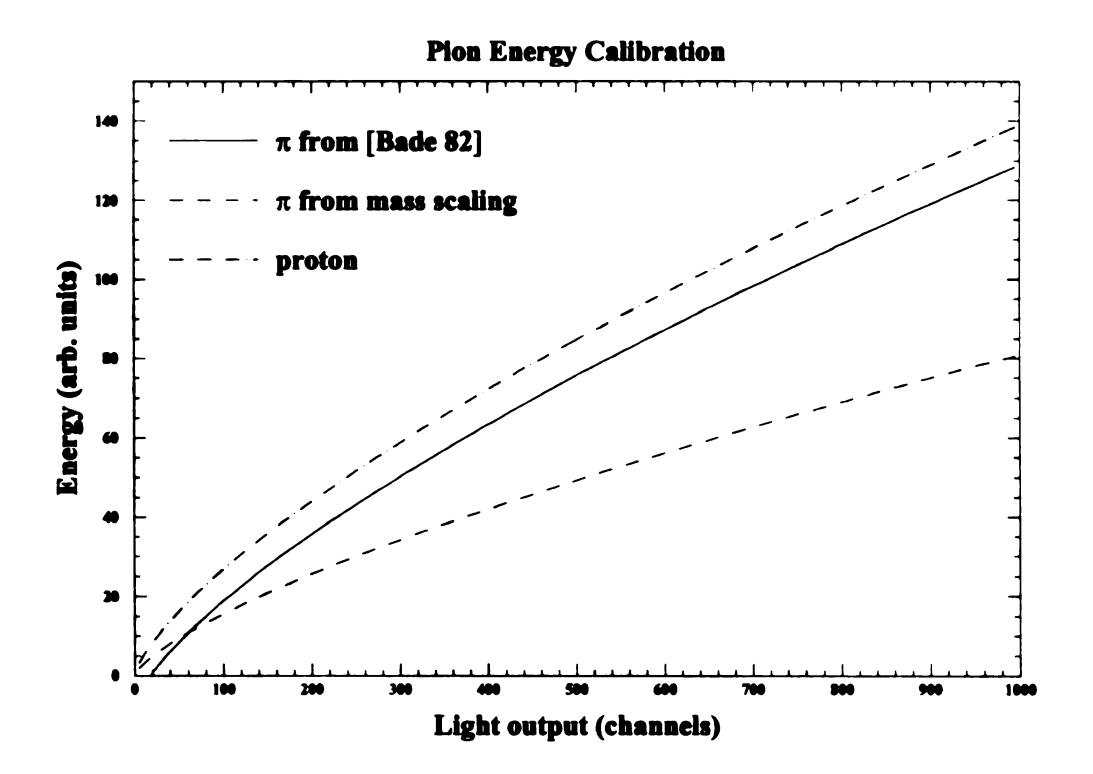


Figure 2.20: Pion energy calibration for plastic phoswich detectors. The pion energies are calibrated relative to the well known proton calibration using the solid line.

Table 2.5: Total number of identified pions for B2 trigger.

$E_{beam}(AMeV)$	# of events with one or more $E_{\mu}$	# of identified pions	approximate number of total events	pions per event
150	443637	47675	100 M	$4.8 \times 10^{-4}$
110	445309	19742	170 M	$1.2 \times 10^{-4}$
90	243182	7291	135 M	$5.4 \times 10^{-5}$

# Chapter 3

# Centrality of Pion Producing Events

#### 3.1 Introduction

In some of the previous experiments that measured pions below the free nucleon-nucleon threshold, indications were seen that a large overlap of the projectile and target nuclei is necessary to produce a pion [Eraz 88, Mill 87]. Also, in the picture of individual nucleon-nucleon collisions producing the pion at the bombarding energies in question, a strong correlation between the number of collisions, and therefore the centrality of the reaction, and the number of pions produced can be expected.

## 3.2 Centrality Selection

The impact parameter or centrality of a nuclear reaction is conventionally determined by dividing the possible values of some event observable into a given number of bins and assume that the values of the observable increase (or decrease) monotonically with decreasing impact parameter. Examples of such observables are total transverse kinetic energy  $KE_t$  or momentum  $P_t$ , charged particle multiplicity  $N_{ch}$  or midrapidity charge  $Z_{mr}$ . For a detailed analysis of advantages and disadvantages as well as possible

auto correlations see Reference [Llop 95]. In this experiment we choose KE<sub>t</sub> as the main centrality observable. Since the total number of nucleons in the system is only 47, all of the multiplicity related observables are very limited in resolution and do not provide a continuous distribution to determine event centrality. For a more detailed description of the centrality selection see Appendix A.

#### 3.3 Less Central

In Figures 3.1 and 3.2 we show the centrality for inclusive and pion gated events as measured by four different event observables. In the case of the total transverse kinetic energy KE<sub>t</sub> (upper two panels) the available phase space is divided into 10 bins ranging from central (high values of KE<sub>t</sub>) to peripheral (low values). Since the displayed data is for the B2 hardware trigger the most peripheral collisions still require two particles in the main Ball, i.e. polar angles above 23°. The absolute normalization of centrality versus impact parameter remains therefore in question, but the trend from central to peripheral events is still valid. The multiplicity related observables N<sub>ch</sub> (number of charged particles, excluding pions), N<sub>lcp</sub> (number of light charged particles) and Z<sub>mr</sub> (midrapidity charge) are, in this reaction, too small to allow for good impact parameter selection. For these we divide the available phase space into only 4 bins. All distributions are area normalized to one. All statistical errors are smaller than the line width or symbol size. The fact that the inclusive centrality distributions for N<sub>ch</sub>, N<sub>lcp</sub> and Z<sub>mr</sub> are not flat at a value of one (like the KE<sub>t</sub> distribution) is due to the limited resolution in these observables.

For the data at 150 AMeV (Figure 3.1) the pion gated distributions (diamonds) produce higher values of the respective observable, indicating more central events. This result is in good agreement with the findings of other authors [Eraz 88, Mill 87],

15

# $^{20}$ Ne + $^{27}$ Al at 150 AMeV incl. events 1.5 pi gated events 1

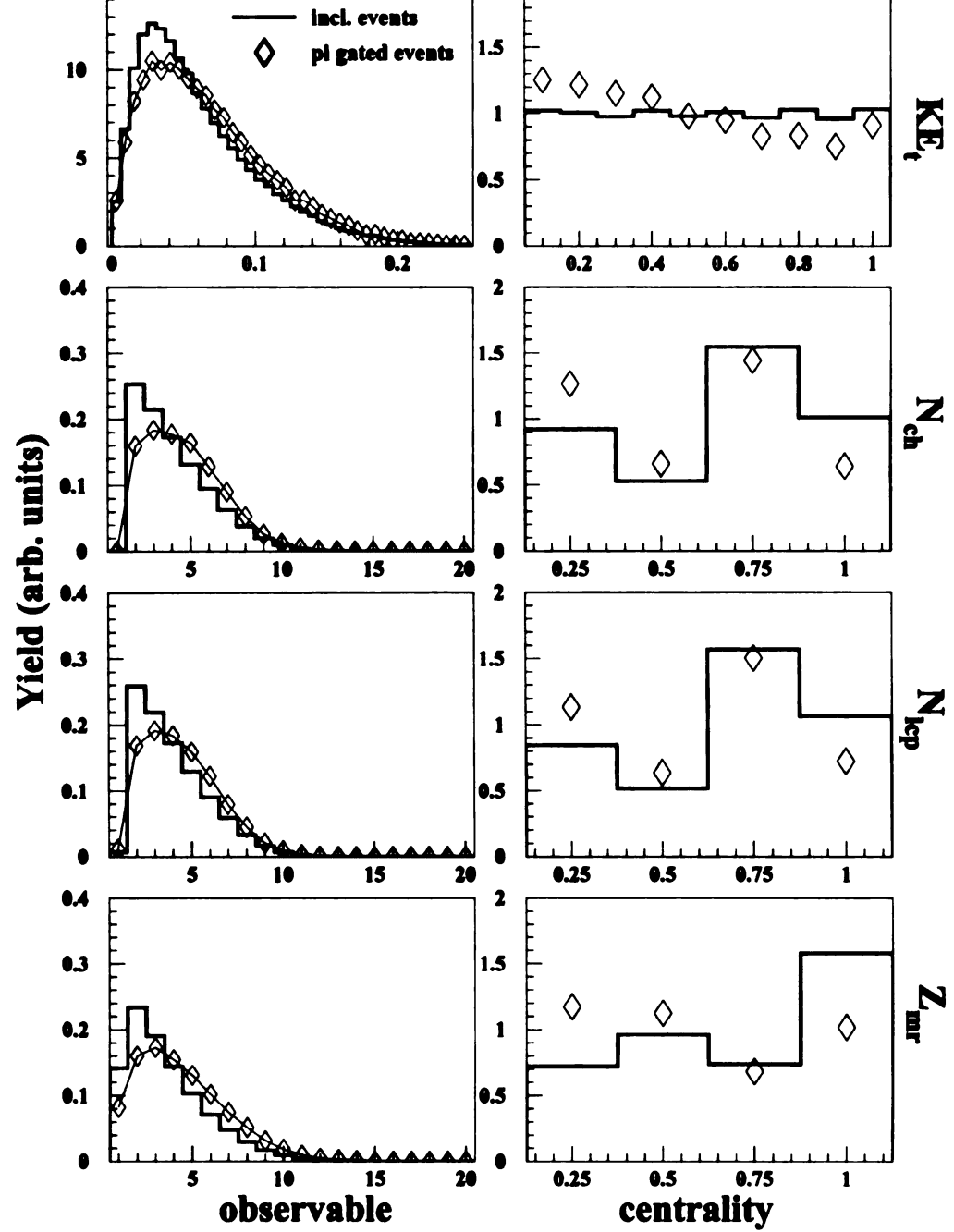


Figure 3.1: Centrality of pion events at  $E_{beam} = 150 \text{ AMeV}$ 

#### $^{20}$ Ne + $^{27}$ Al at 90 AMeV 15 2 incl. events 1.5 pi gated events 10 1 5 0.5 0.2 0.1 0.2 0.4 0.6 8.0 2 $\Diamond$ 0.3 1.5 0.2 1 Yield (arb. units) 0.5 20 0.25 5 10 15 0.5 **0.75** 1 2 0.3 1.5 $\Diamond$ 0.2 1 0.1 0.5 20 10 15 0.25 0.75 0.5 1 2 0.4 0.3 1.5 $\Diamond$ 0.2 1 0.1 0.5

Figure 3.2: Centrality of pion events at  $E_{beam} = 90 \text{ AMeV}$ 

0.25

20

0.5 0.75 centrality

observable

where different methods were used to determine centrality in pion producing events. At the lower bombarding energy of 90 AMeV (Figure 3.2) the total number of pion producing events is significantly lower than for the 150 AMeV case ( $\approx 50000$  at 150 AMeV vs.  $\approx 7000$  at 90 AMeV). While a preference for central events is still present in these data, it is much less pronounced than for the 150 AMeV data, possibly indicating a transition to some more collective process and a less dominant production from individual nucleon-nucleon collisions.

In Figure 3.3 we show a comparison with BUU model calculations [Baue 89, Li 91a]. The BUU calculations were done for the impact parameters determined in Appendix A, which are 2.0, 3.43, 4.43, 5.24 and 5.93 fm. Both the data and the calculations are normalized to unity at the most central bin. At all three beam energies the BUU predictions show a much steeper decrease of the total pion yield with impact parameter than do the data. The BUU calculations were done using a parameterization for a medium equation of state for nuclear matter. Employing a stiff or soft parameterization does not change the results, i.e. the number of pions produced for a given impact parameter. One rather obvious explanation of the discrepancy would be that in peripheral collisions other more collective processes are responsible for the production of pions. On the other hand, it is possible that the total transverse kinetic energy (KE<sub>t</sub>) does not provide a good centrality selection for events that produce a pion since the energy necessary to produce the pion is missing from the system, possibly reducing the values of KE<sub>t</sub>.

In order to further investigate that possibility we can make use of different centrality observables and look for a change in the centrality as determined by  $KE_t$  for events classified as peripheral or central by these other observables. In Figure 3.4 the  $KE_t$  distributions for all events and events with an identified pion are displayed for the global observables  $N_{ch}$ ,  $N_{lcp}$  and  $Z_{mr}$ .

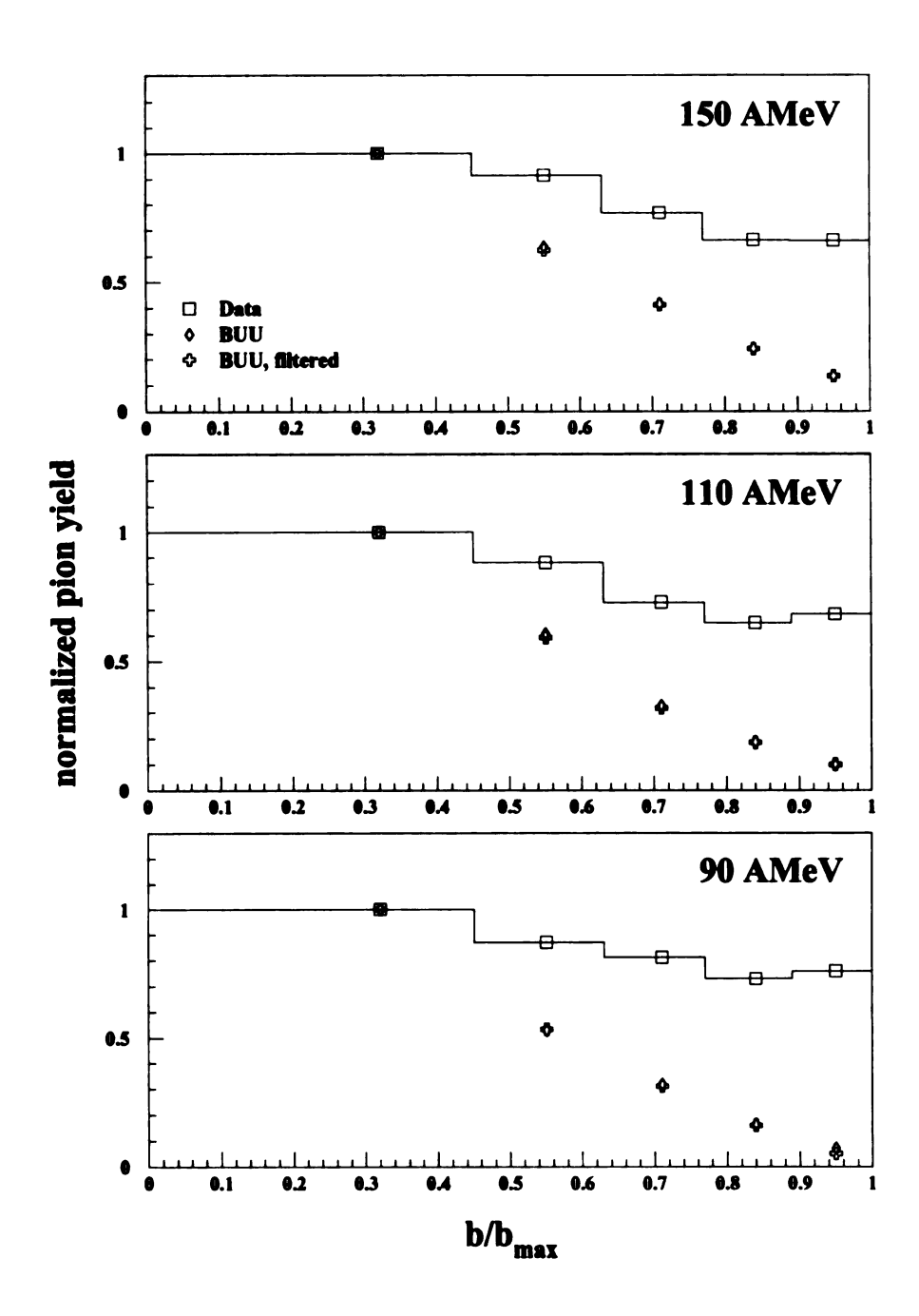


Figure 3.3: Comparison of total pion yield as a function of centrality with BUU calculations.

The circles are for ungated events and are naturally identical for the three observables, the squares are for events with a value of less than 5 for the above observables, representing a peripheral cut, and the triangles for events with a value larger or equal to 5, representing a central cut. The value of 5 represents the point where about 50% of the events are classified as central. The panels in the left column (open symbols) are for events without a pion gate and the right column (filled symbols) for events that had an identified pion. In all cases the central cut shows significantly higher values of KE<sub>t</sub>, as expected, whereas the peripheral one represents most of the low values. In order to be a little more specific, we can determine the mean values for  $KE_t$  for all these event classes. In Figure 3.5 the average  $KE_t$  is shown for the three different global observables. The symbols have the same meaning as in Figure 3.4. For all three observables the pion requirement increases the average KE<sub>t</sub> for the inclusive and the peripheral gate. For the central gate, on the other hand, gating on events with a pion decreases the average by about the same amount, indicating that indeed producing a pion in a central event lowers the average value of KEt. Since the overall size of that change for all event classes is much smaller than the change by going from peripheral to central, we conclude that the requirement of a pion in an event does not significantly change the apparent centrality of the event. Therefore the enhancement of the total pion yield for peripheral events as compared to BUU (see Figure 3.3) could be a real effect.

In order to demonstrate the effect of the pion gate on the centrality of the event in a more direct comparison with impact parameter, we show the probability distributions as a function of reduced impact parameter in Figure 3.6. The open circles are obtained from events with no gating condition and the filled circles are for events where a pion was detected. For all three beam energies the curves for pion events rise faster than the inclusive ones, indicating more central events. After going through a plateau

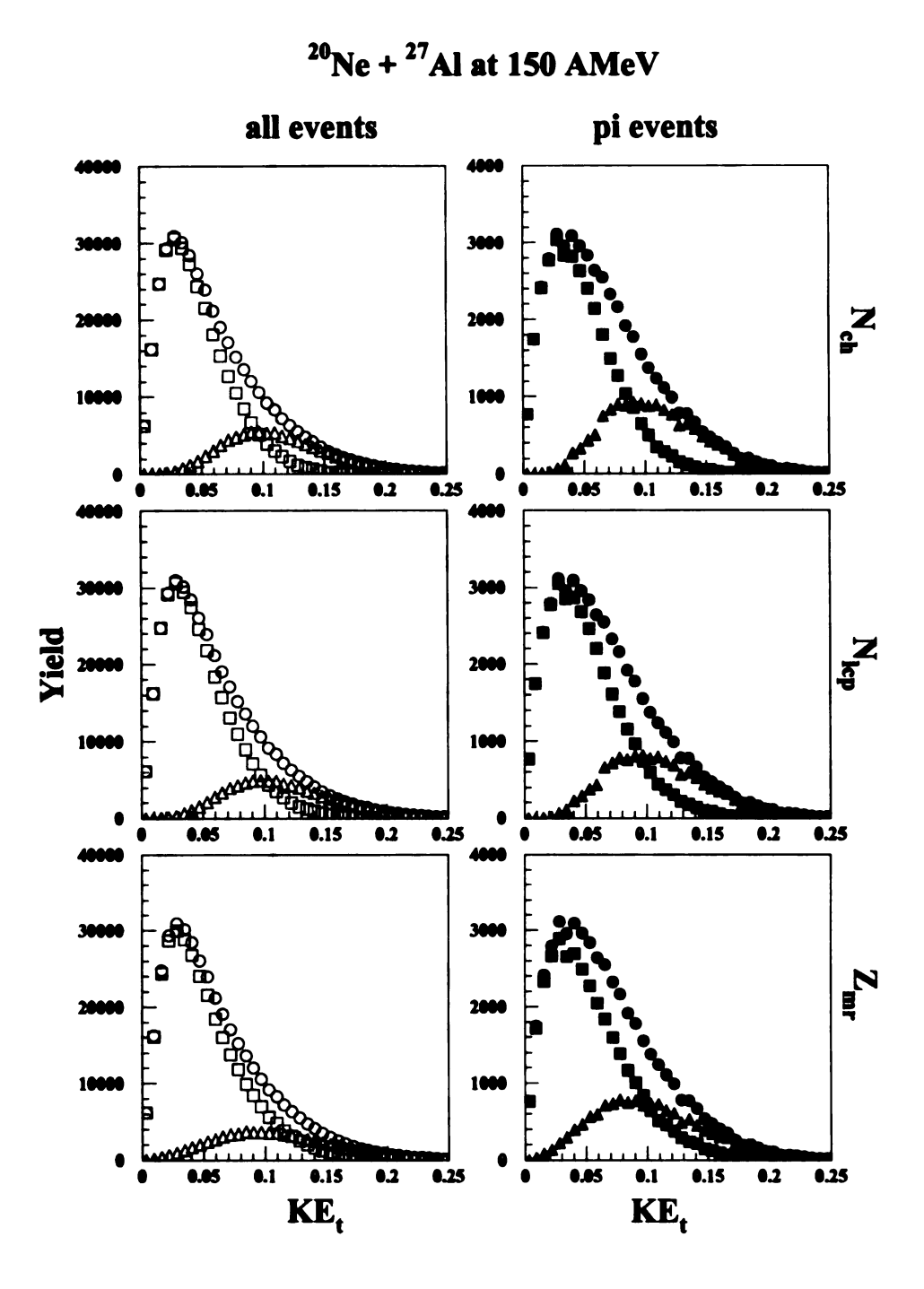


Figure 3.4: Inclusive (circles), central (triangles) and peripheral (squares) KE<sub>t</sub> distributions for inclusive (open symbols) and pion gated (filled symbols) events.

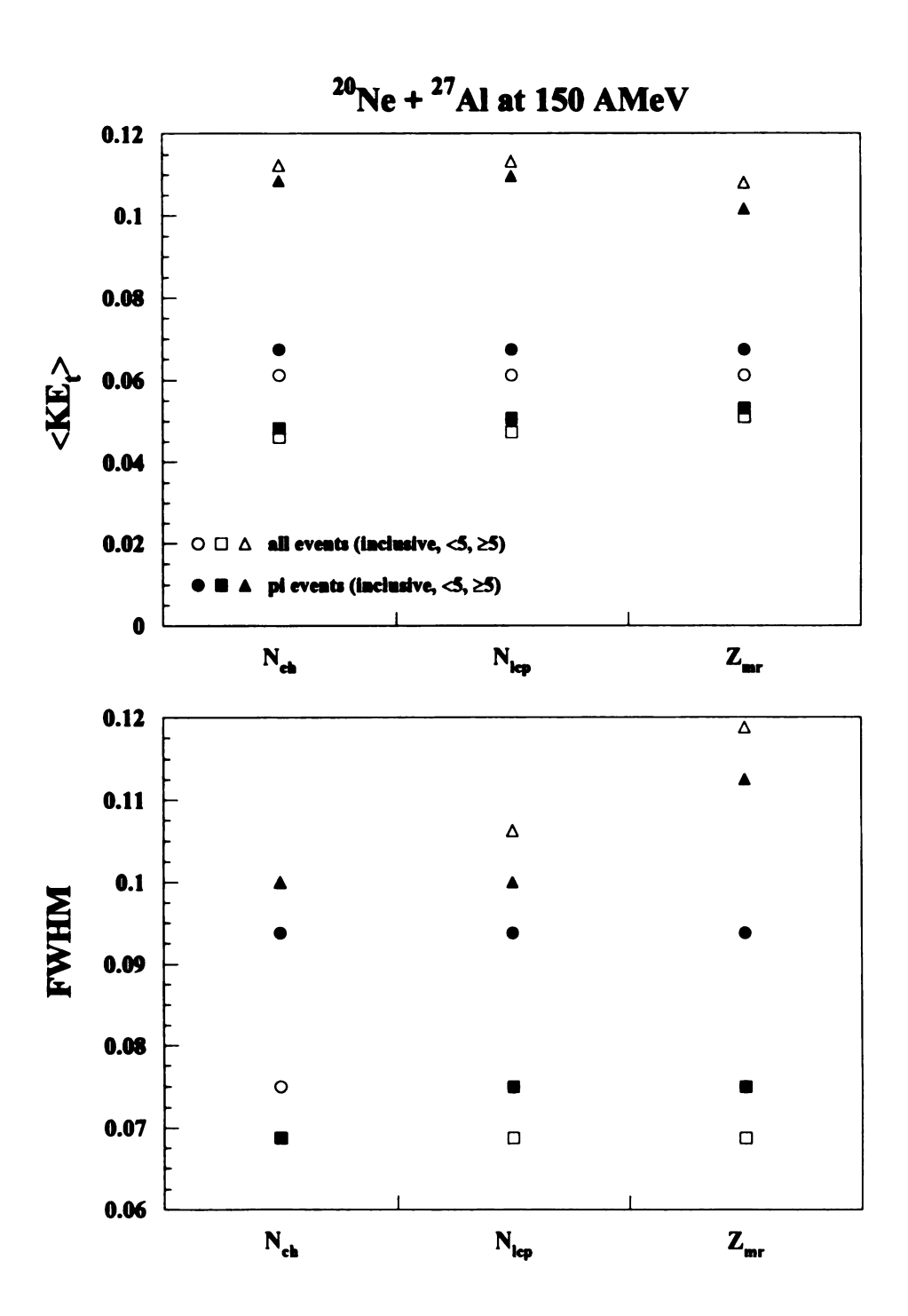


Figure 3.5: Mean  $KE_t$  values and width for the gates from Figure 3.4.

at about  $0.6b/b_{max}$  the gated distributions rise again at the most peripheral impact parameters. It should be noted that this effect does not depend on the detection angle of the pions, so that contamination from neutral particles in the pion gated events is unlikely.

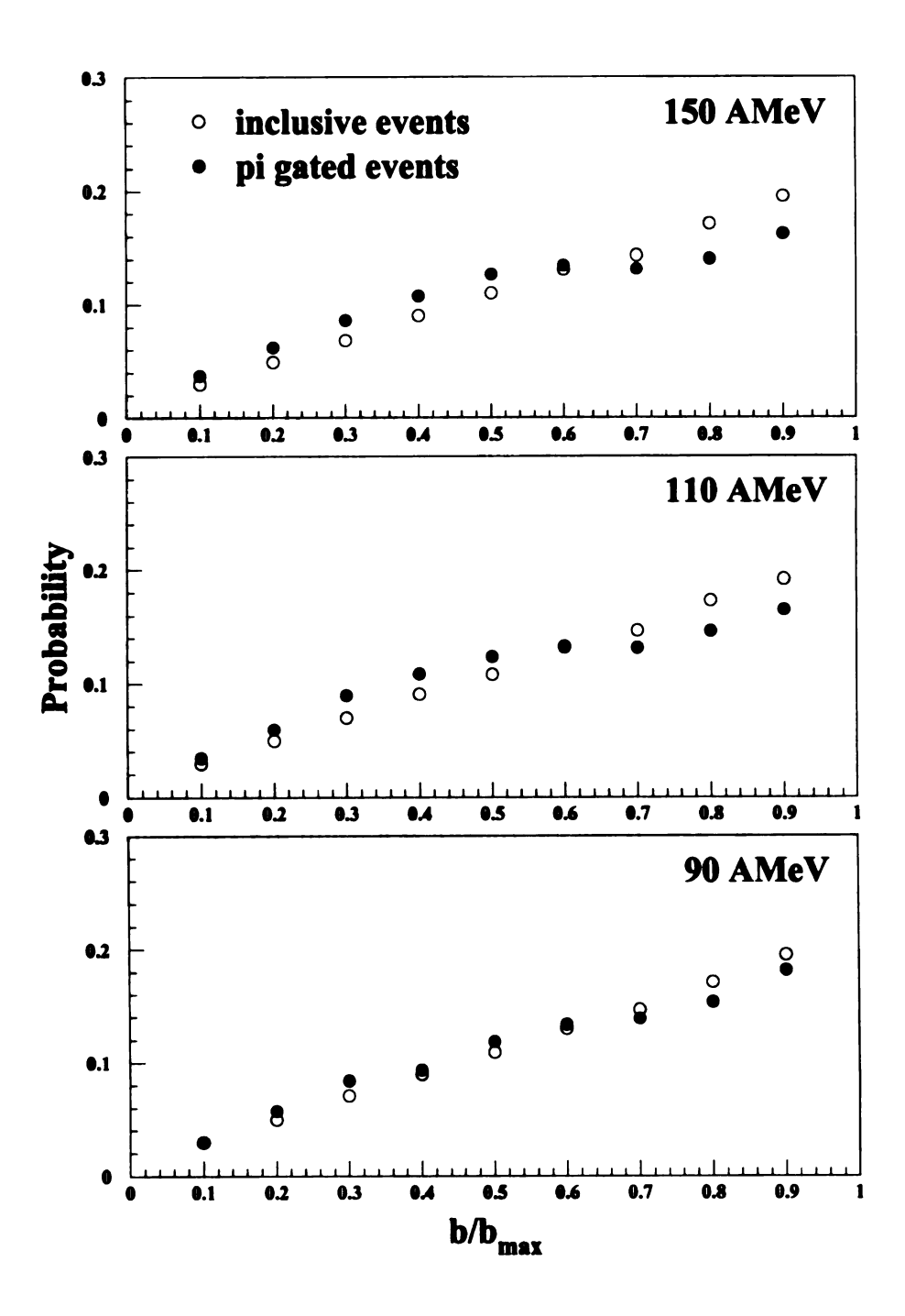


Figure 3.6: Impact parameter distributions for pion events (filled circles) compared to inclusive events (open circles) for the three beam energies.

# Chapter 4

# Single Particle Distributions

## 4.1 Polar Angle Distributions

Polar angle distributions in the laboratory frame in general show a strong forward focussing for all particle types (in fixed target experiments). The heavier the particles the more forward boosted it appears in the laboratory frame. The laboratory polar angle distributions for pions, protons, Helium and Lithium ions are shown in Figure 4.1 for impact parameter inclusive events at the beam energy of 150 AMeV. As expected the pions are much less forward focussed than the other particle types. The enhancement at backward angles can be attributed to a combination of enhanced emission from a target like source and shadowing from the target holder and the target itself. The first effect can be clearly seen in Figure 4.2 where the same distributions are shown as in Figure 4.1 but this time only for particles from central (squares) and peripheral (triangles) events. For protons and Helium ions a clear enhancement at around 130° in the laboratory frame can be observed. For Lithium ions the effect seems to be present, but the statistical errors are too large to make a strong statement. The fact that the pions do not show any difference between the central and the peripheral gates, indicates that no pion emission from a target like source is present and the suppression at angles around 90° is entirely due to shadowing by the target frame and the target itself.

In Figures 4.3 and 4.4 we show the polar angle distributions in the laboratory frame for both protons and pions as solid histograms. The symbols indicate BUU calculations at impact parameters of b=2.0, 3.43, 4.43, 5.24 and 5.93 fm. The diamonds are raw calculations, whereas the crossed points are obtained after all test particles from the calculation are subjected to a possible rejection by a software replica of the detector acceptance of the  $4\pi$  Array. For the first frame in the figures (BIN0), which shows the impact parameter inclusive distributions, no BUU calculations were done. For all but the very peripheral collisions (BIN5) the filtered BUU calculations reproduce the data very well for protons as well as for pions. While the raw BUU calculations do not change appreciably with impact parameter, the filtered ones and the data show an enhancement at the backward angles for the more peripheral reactions. This seems to indicate a change in the detection efficiency by going from central to peripheral events. That can be expected since particles from a target like source will have lower kinetic energy in the lab frame and are therefore more affected by absorption in the target frame and the target itself.

### 4.2 Kinetic Energy Distributions

The kinetic energy distributions for different particle types are important to understand the reaction mechanism in nuclear collisions. By assuming thermal equilibrium in the hot overlap region of projectile and target, the slopes of the kinetic energy distribution give direct access to the temperature, and therefore the excitation energy of the reaction zone. Especially particles that have to be produced in the reaction are supposed to carry information about the properties of the medium in which they are produced. Previous experiments show that temperatures extracted from pion energy

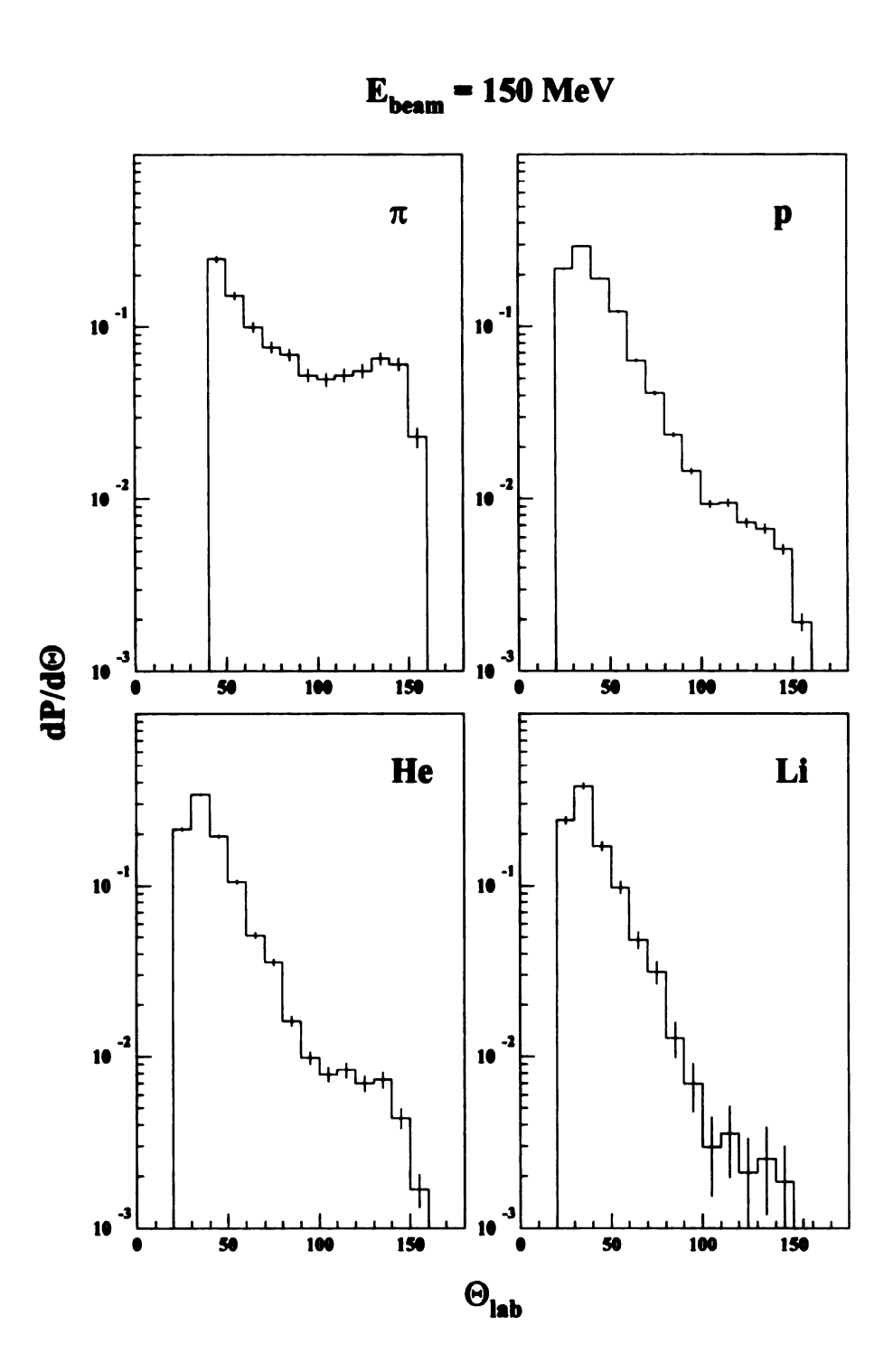


Figure 4.1: Laboratory polar angle distributions for several particle types at  $E_{beam} = 150 \text{ AMeV}$ .

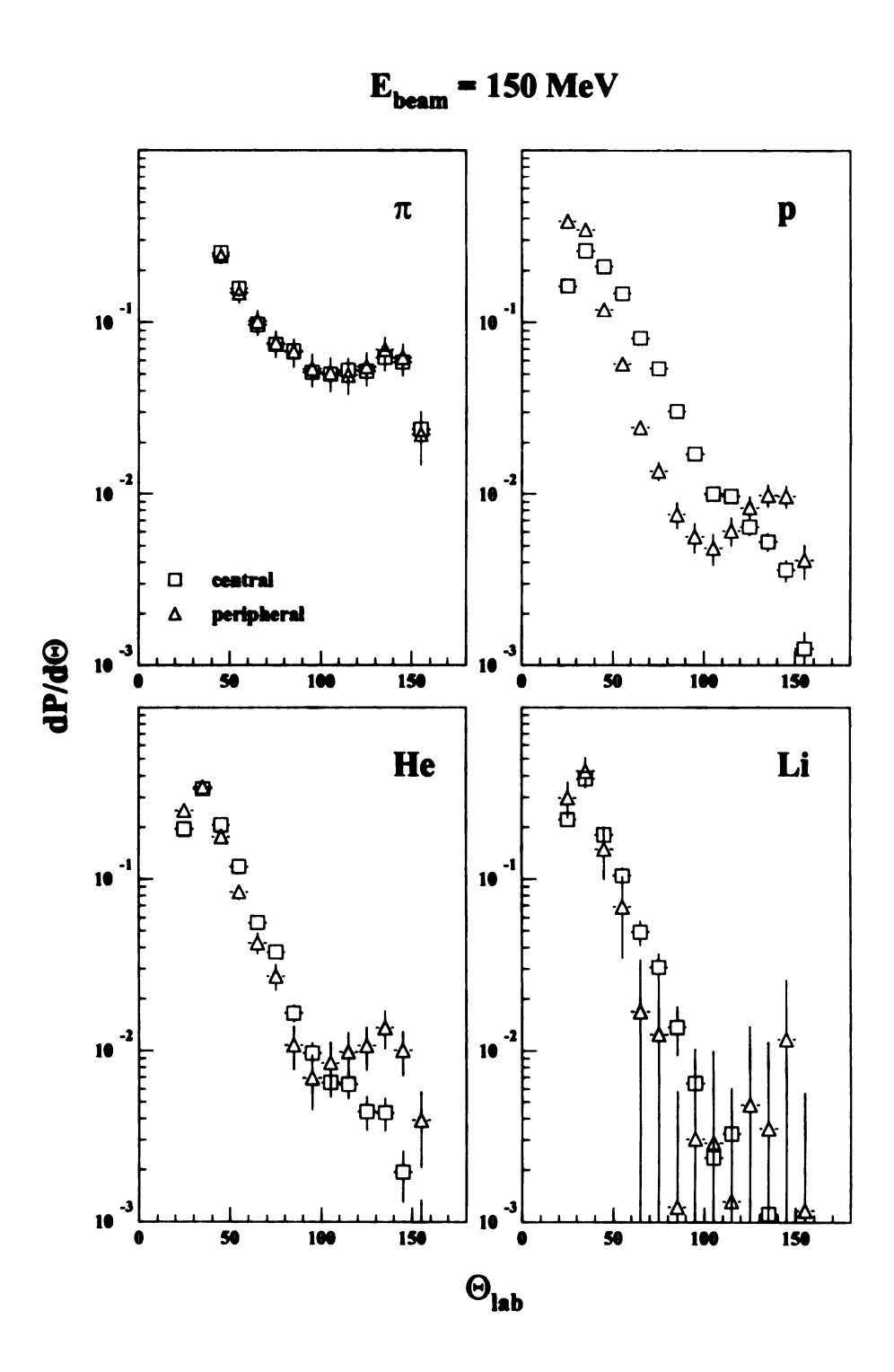


Figure 4.2: Same as Figure 4.1 for particles from central (squares) and peripheral (triangles) events.

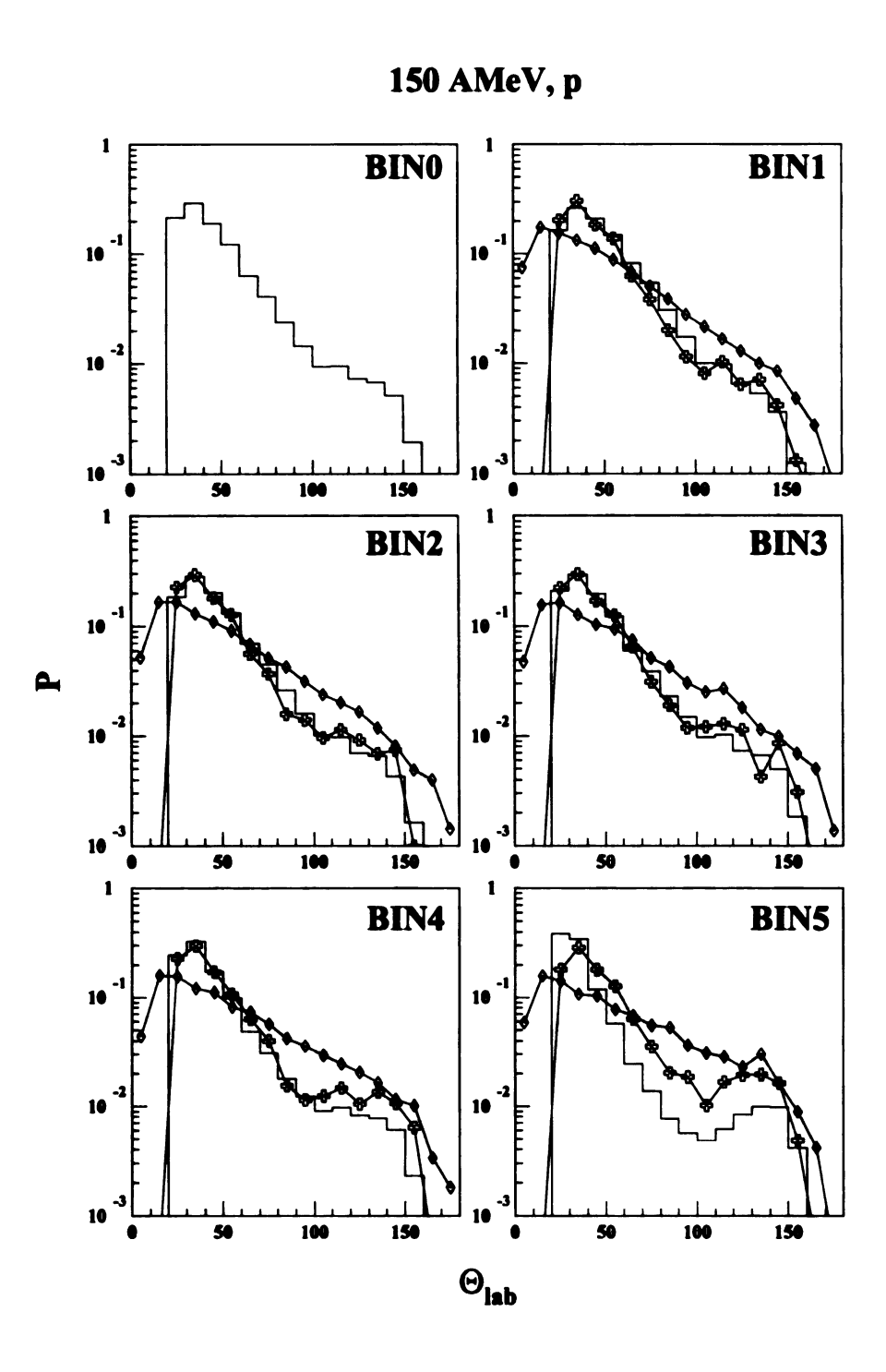


Figure 4.3: Comparison of proton polar angle distributions (histograms) with raw (triangles) and filtered (crosses) BUU calculations for centrality bins from central (BIN1) to peripheral (BIN5).

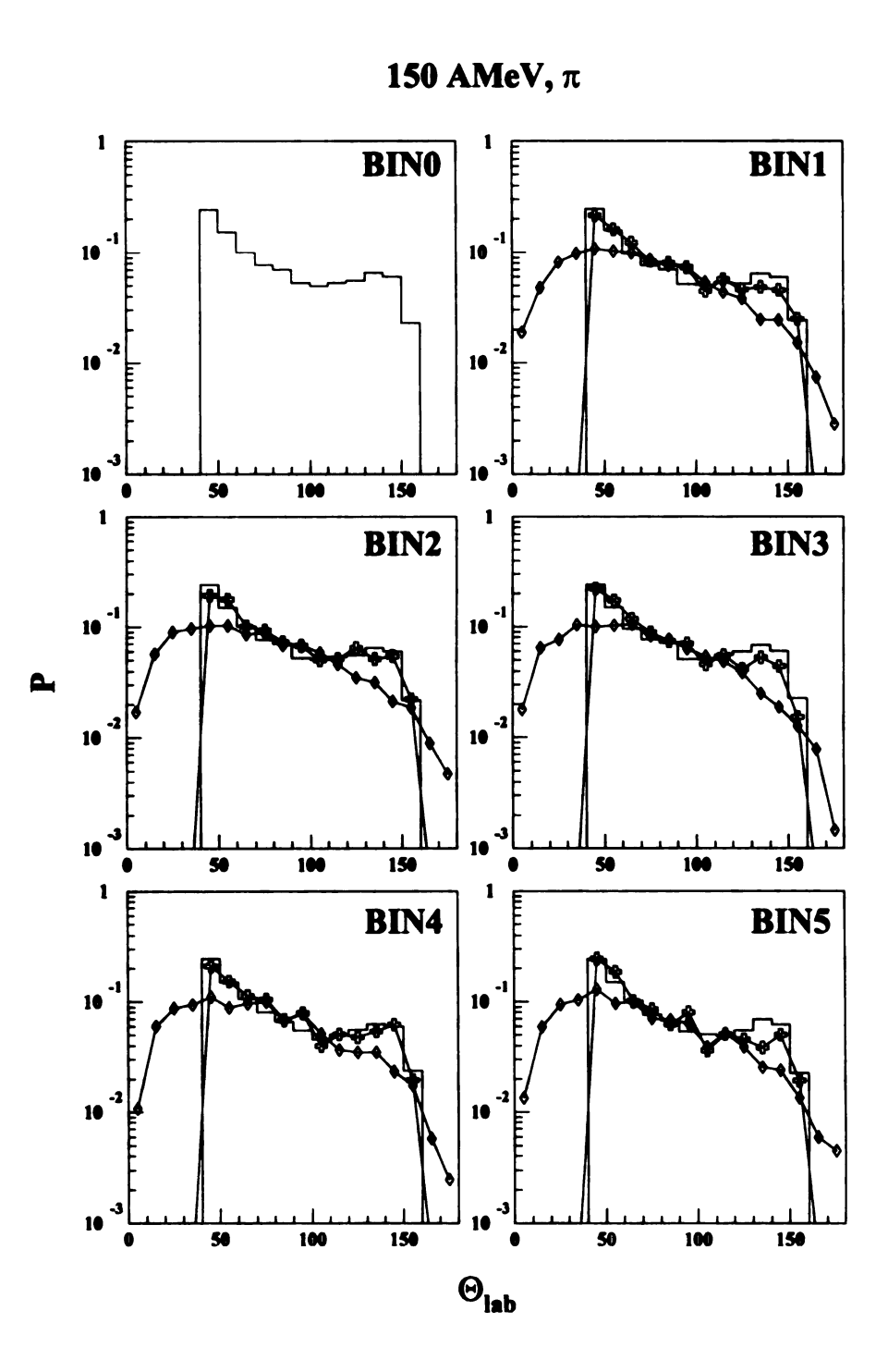


Figure 4.4: Comparison of pion polar angle distributions with raw and filtered BUU calculations for several centrality bins.

spectra are lower than those from proton distributions for bombarding energies above 95 AMeV [Naga 81]. One experiment ( $^{16}O + ^{27}Al$  at 94 AMeV) [Barb 90a] found that the temperature extracted for protons (17 MeV) can be used to fit the positive pion spectra as well. At a lower bombarding energy of 41 AMeV Suzuki et al. reported a temperature of 16 MeV for negative pions [Suzu 91a] whereas the proton temperature for a similar reaction was determined to be around 9 MeV [Glas 83]. Table 4.1 gives an overview for most of the published data for pion temperatures in heavy ion collisions both above and below the free nucleon-nucleon threshold.

As far as the source of pions is concerned it is generally assumed that they are dominantly produced from the intermediate (cm) source in a spectator-participant model. One experiment [Bada 93a] determined a source velocity between the center of mass and the projectile-like source for neutral pion emission. In Figures 4.5 and 4.6 we show the pion kinetic energy spectra in the laboratory frame for angles between 45° and 153° at the two higher beam energies. The different panels in the figures show the results for inclusive and centrality gated reactions (BIN1 being central, BIN5 peripheral). All spectra show the typical exponential decrease for higher energies as well as a bump at low energies. The data for 45° show an enhancement for higher energies, which is probably due to contamination from high energy neutrons that leak into the pion PID gate. All distributions are solid angle normalized, but do not include any correction for pion detection efficiency.

The solid lines in Figures 4.5 and 4.6 are obtained by fitting the two-dimensional  $dN/dEd\Omega$  spectra with a boosted Maxwell-Boltzmann distribution. As in other experiments a single source of pions is assumed, but the velocity of that source  $(\beta_{\pi})$  is left as one of the fit parameters. The other fit parameters are the pion temperature (in the emitting frame)  $\tau_{\pi}$  and an overall normalization factor A. Explicitly, the

Table 4.1: Compilation of pion temperatures from different experiments.

reference	system	E <sub>beam</sub> (AMeV)	pion charge	τ (MeV)
[Barb 90a]	<sup>16</sup> O+ <sup>27</sup> Al	94	+1	17.1
[Joha 82]	<sup>12</sup> C+ <sup>12</sup> C	85	+1	14
,	<sup>12</sup> C+ <sup>197</sup> Au	85	+1	15
[Bern 84] <sup>a</sup>	$^{12}C + ^{12}C$	85	+1	17
[Bada 93a]	<sup>16</sup> O+ <sup>27</sup> Al	94	0	22.1
[Lebr 90] <sup>b</sup>	<sup>16</sup> O+X	93	0	10
[Grim 85] <sup>c</sup>	<sup>12</sup> C+ <sup>12</sup> C	48	0	13.5
	$^{12}C + ^{12}C$	60	0	15
	$^{12}C + ^{12}C$	74	0	17.5
	$^{12}C + ^{12}C$	84	0	19.5
[Naga 82]	<sup>14</sup> N+NaF	400	-1	39
	<sup>14</sup> N+NaF	183	-1	25
[Mill 87]	$^{139}La + ^{139}La$	138	-1	14
	<sup>139</sup> La+ <sup>139</sup> La	183	-1	21
	$^{139}La + ^{139}La$	246	-1	25
[Haya 88]	$^{139}La + ^{139}La$	800	-1	56
[Suzu 91a]	$^{14}N + ^{12}C$	135	-1	16± 1
	$^{14}N + ^{12}C$	80	-1	15± 1
	$^{14}N + ^{12}C$	67	-1	13± 2
	$^{14}N + ^{12}C$	41	-1	16± 2
[Naga 81]	Ar+Pb	800	-1	72
	Ar+KCl	800	-1	66
	C+C	800	-1	60
	Ne+NaF	800	-1	62

asame for π⁻

 $<sup>^</sup>b T_\pi \leq 30 {\rm MeV}$   $^c \tau$  from Bose-Einstein statistics,  $d^3 \sigma/dp^3 = 1/(exp(E/\tau) - 1)$ 

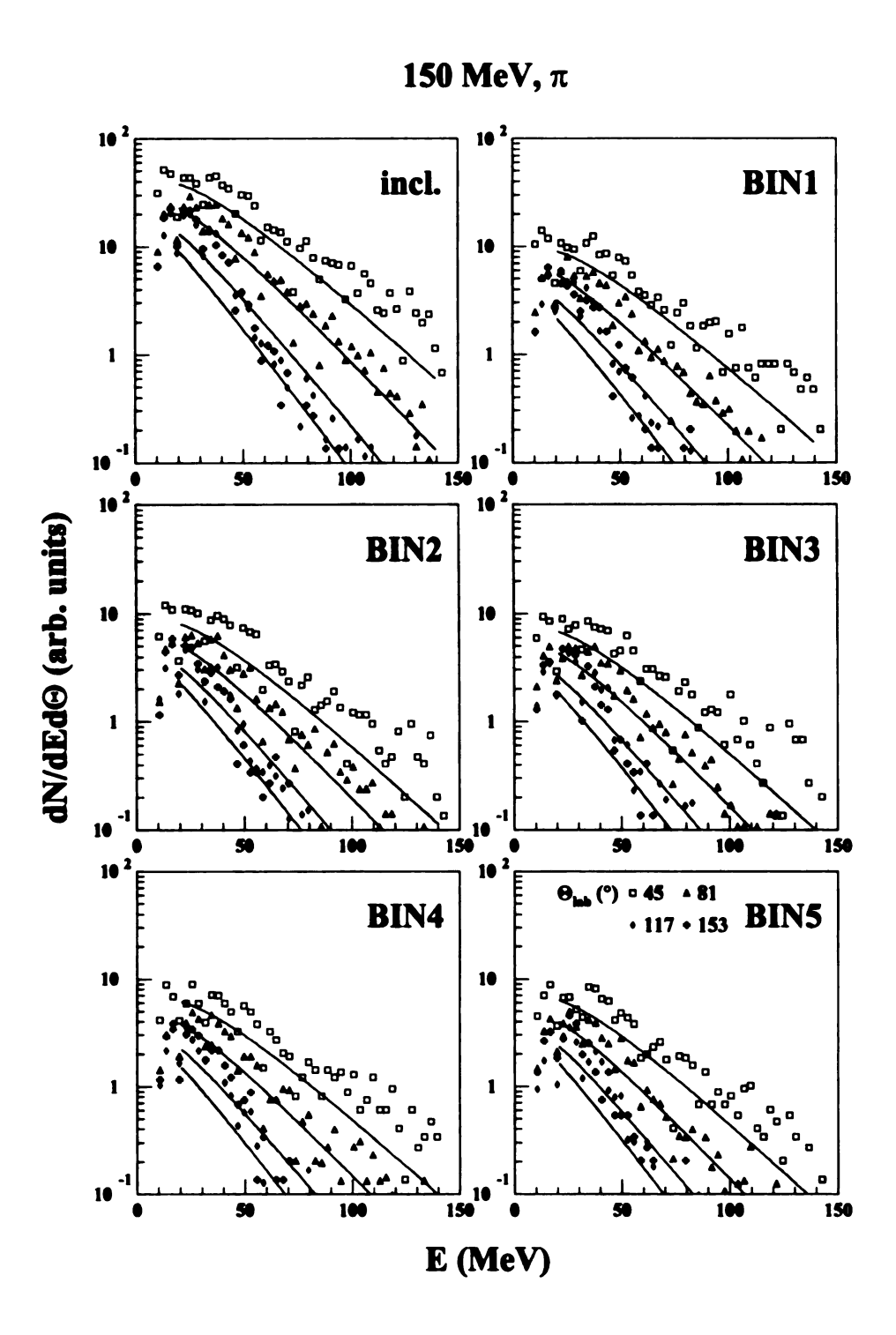


Figure 4.5: Pion kinetic energy distributions at 150 AMeV for several angles and centrality bins. The solid lines are for moving source fits.

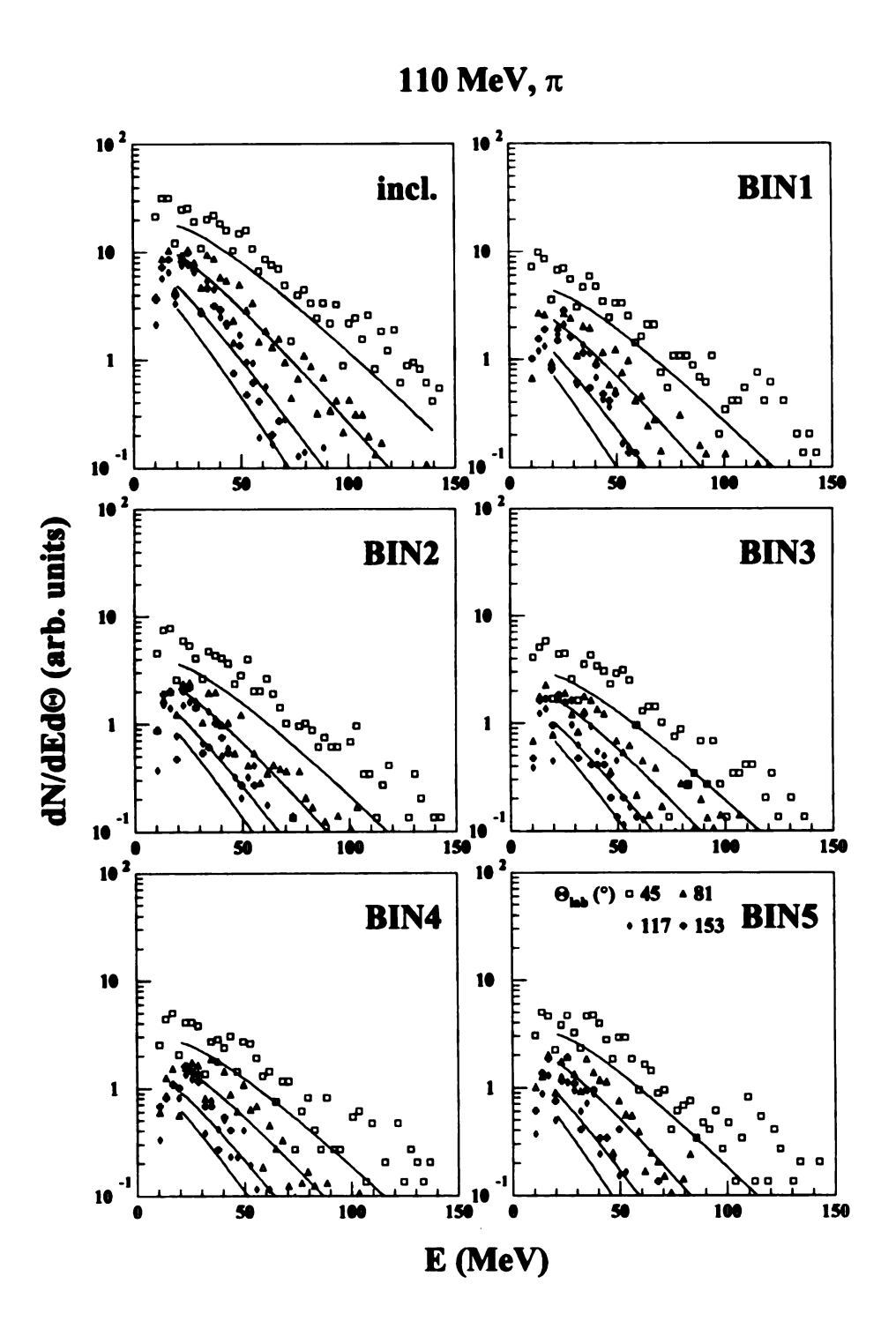


Figure 4.6: Same as Figure 4.5 for 110 AMeV.

equation used is

$$\frac{d^2N}{dEd\Omega} = A\frac{P}{P'}\frac{d^2N}{dE'd\Omega'} \tag{4.1}$$

$$\frac{d^2N}{dE'd\Omega'} = \frac{\sigma_0}{4\pi m^3} \sqrt{T'} exp(-\frac{T'}{\tau_{\pi}})$$
 (4.2)

$$E' = \gamma_{\pi}(E - \beta_{\pi}P\cos\theta) \tag{4.3}$$

where the primes denote cm quantities and  $\gamma_{\pi} = 1/\sqrt{1-\beta_{\pi}^2}$ . The resulting values of  $\tau_{\pi}$ ,  $\beta_{\pi}$  and A for 150 AMeV and 110 AMeV are shown in Figures 4.7 and 4.8 for all centrality bins. The bin labeled 0 represents the results for the impact parameter inclusive fits.

One interesting result is that none of the parameters depend on the centrality of the event. This finding is expected for emission from a completely thermalized source. The normalization factor A for the impact parameter inclusive bin (BIN0) is naturally about 5 times larger than for the 5 different centrality bins. Again the constancy of A with centrality is rather surprising, but follows the findings from Chapter 3.

The slope parameters  $\tau_{\pi}$  are in very good agreement with the values from Table 4.1. In Figure 4.9 we present the data from Table 4.1 (open symbols) and include the points for our measurements (filled stars). The data from this experiment link the positive and negative pion data at low energies to the data for negative pions at the higher energies. The trend for neutral pions seems somewhat different than the one observed for charged pions.

Figure 4.10 shows the beam energy dependence of the source velocity and the slope parameter (open symbols) for impact parameter inclusive events. The reversed trend in the source velocity  $\beta_{\pi}$ , as compared to the values of the cm velocities, could be due to the lack of identified pions in the forward direction. Although the polar angle distributions for pions are not as forward focussed as the ones for other particles, the

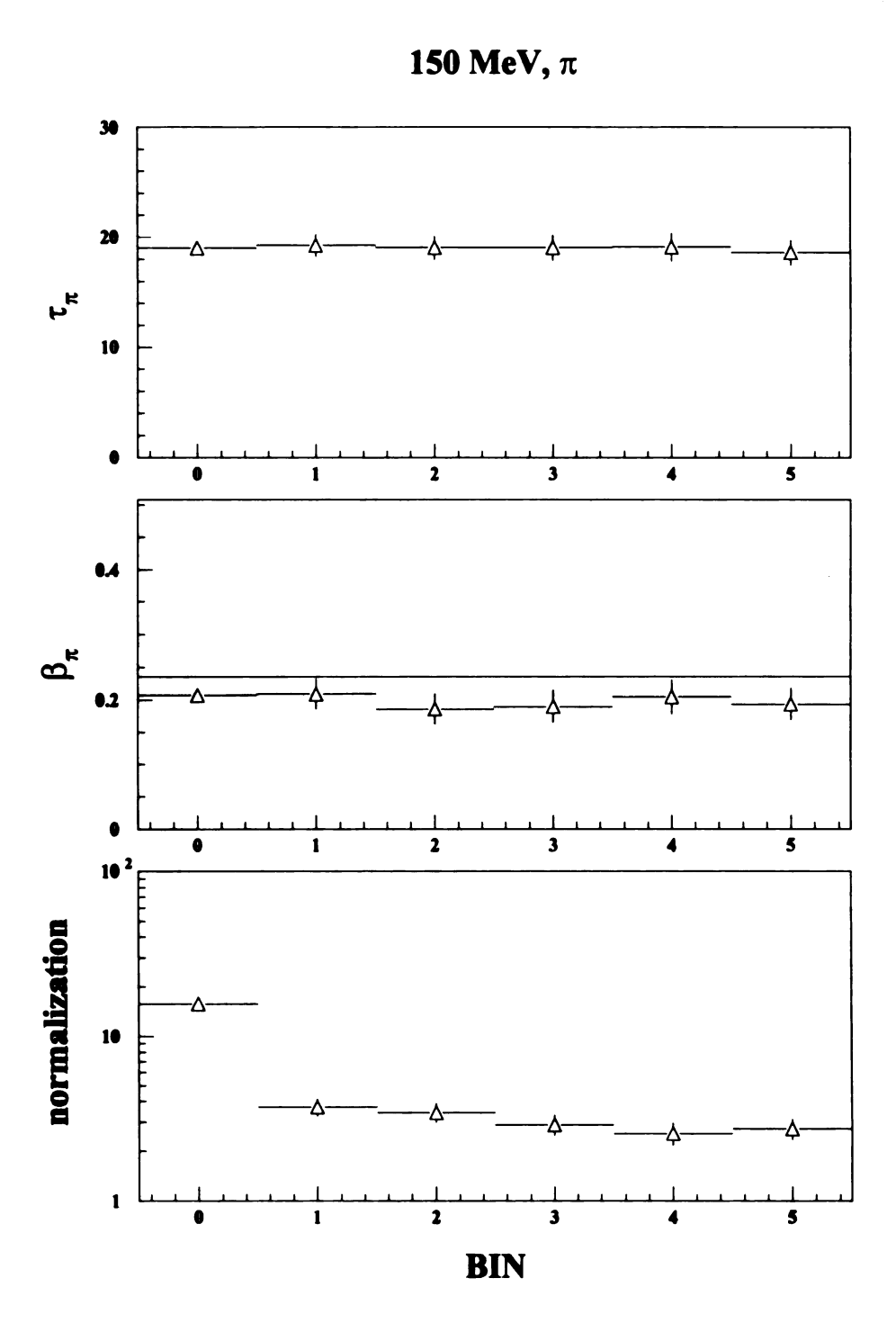


Figure 4.7: Resulting fit parameters from a moving source fit to a Maxwell-Boltzmann distribution for pions at 150 AMeV. The solid line in the middle frame indicates the value of  $\beta_{cm}$ .

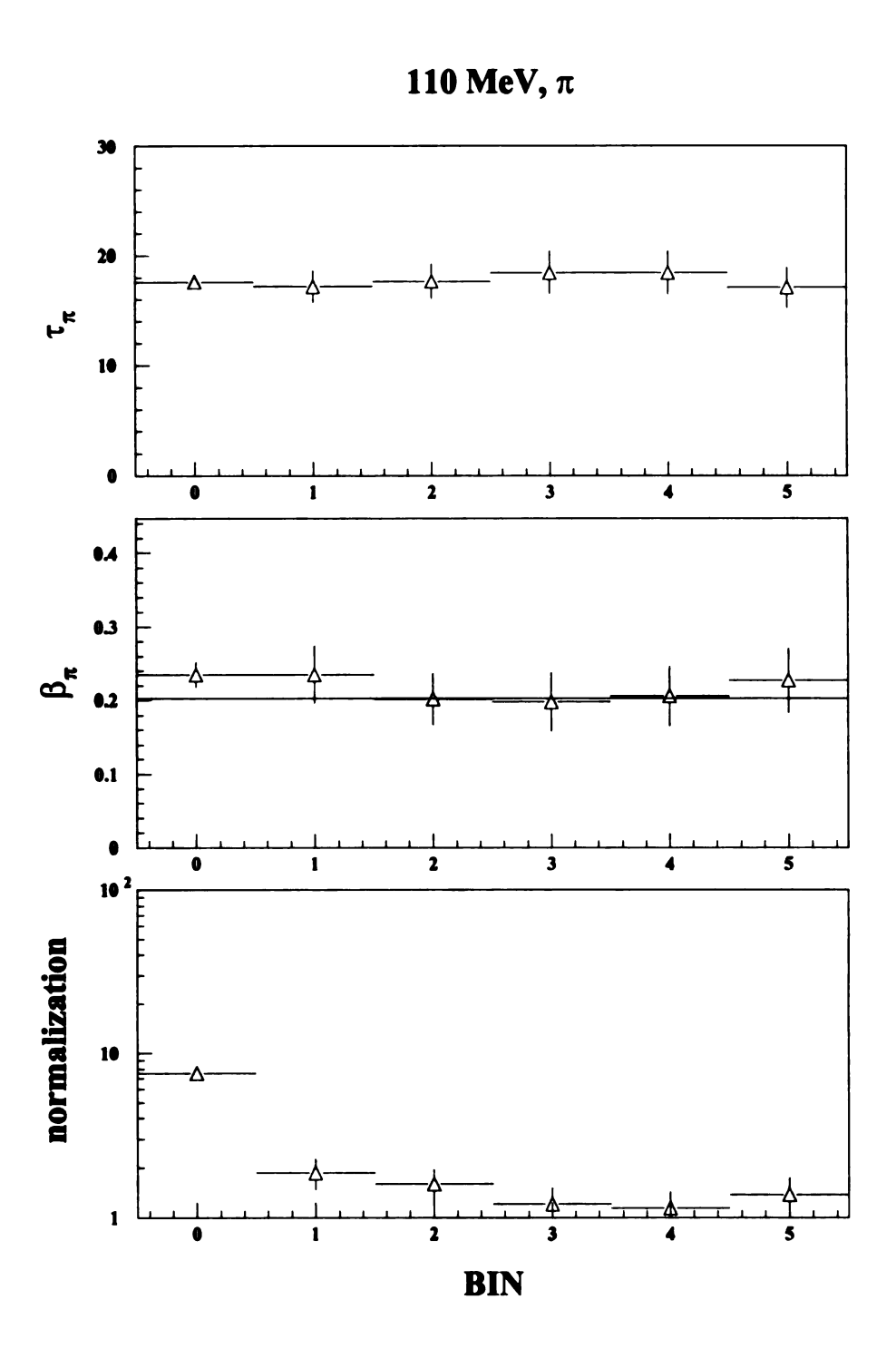


Figure 4.8: Same as Figure 4.7 but for 110 AMeV.

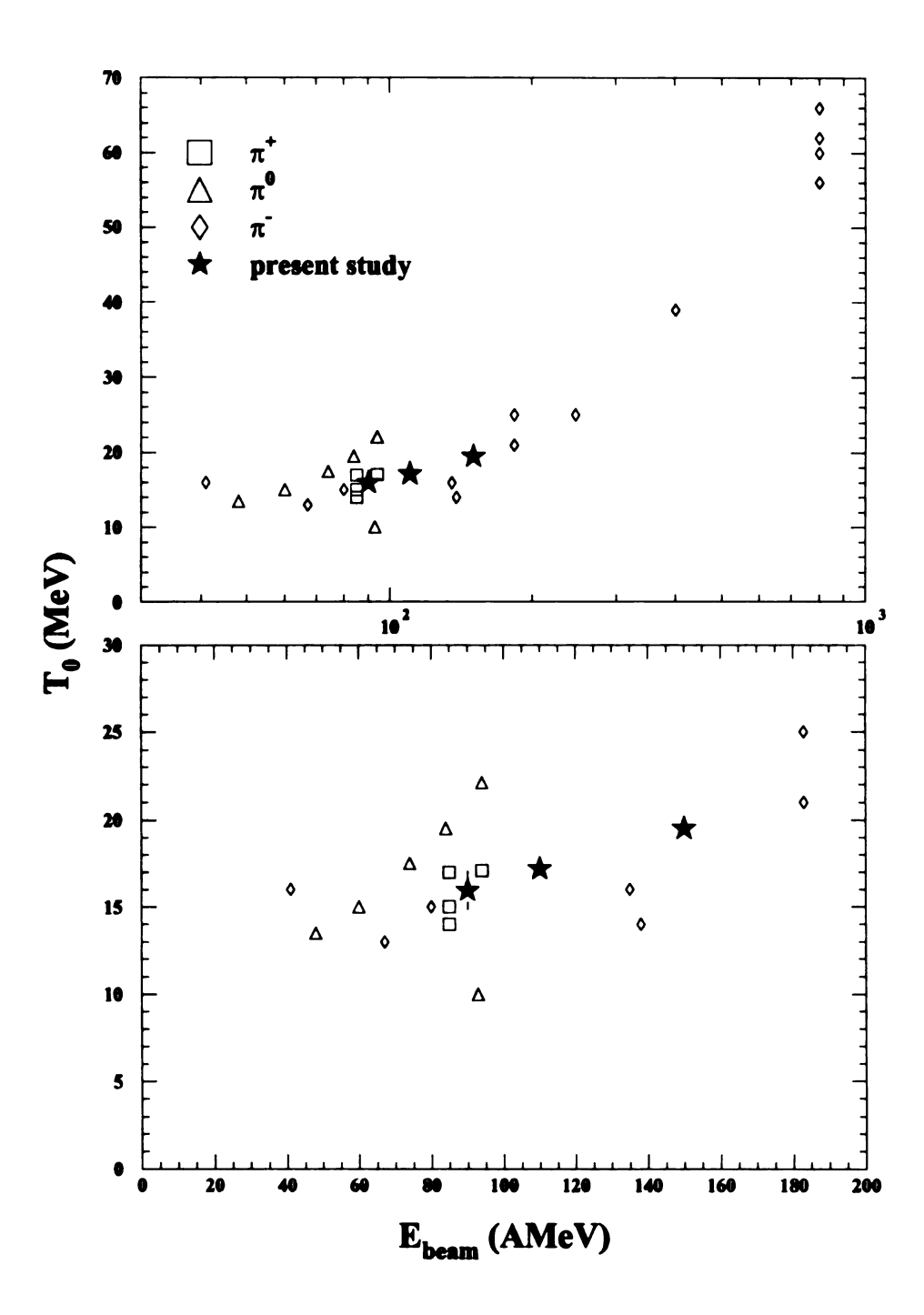


Figure 4.9: Compilation of pion temperatures from different experiments. The lower panel displays the data up to 200 AMeV on a linear scale. The open symbols represent the data from Table 4.1. The errors are typically of the order of 1-2 MeV. The errors for this study are statistical only.

effect is still present and a larger number of pions will not be detected at the higher beam energies. In order to further investigate the possibility of a misidentification of the pion source that may be related to detector acceptance or pion identification problems, we performed another set of fits to the data; again using equation 4.3 but this time keeping the source velocity fixed at the value for the intermediate (i.e., cm) source. These values are indicated in the figure as filled symbols. Even though the source velocities in both cases are quite different, the values of  $\tau_{\pi}$  are essentially the same.

In order to check the assumption of pions being emitted from an equilibrated source in the cm system, we apply the same method to the proton kinetic energy spectra. Figure 4.11 shows the data together with the obtained fits. The overall agreement with the data is good for the inclusive as well as the more central bins. In peripheral collisions the data can probably not be described with a single emitting source since strong contributions from a target like source, especially at the backward angles, can be expected. A contribution from a projectile like source does not seem to be present in the data, since the smallest angle included in the fits is 36°.

In Figure 4.12 the resulting parameters of the fits are displayed. In contrast to the pion result the slope parameter  $\tau_p$  decreases with centrality. In this figure, the impact parameter inclusive bin (BIN = 0) shows the weighted average. The apparent source velocity  $\beta_p$  also decreases from values slightly above to somewhat below the cm velocity, again indicating target like source contributions for peripheral events. The value obtained for the impact parameter inclusive fit is within a few percent of the cm velocity.

In Figure 4.13 we compare the results obtained for  $\tau_p$  and  $\beta_p$  at all three beam energies. The general trend is that  $\tau_p$  as well as  $\beta_p$  decrease with decreasing centrality

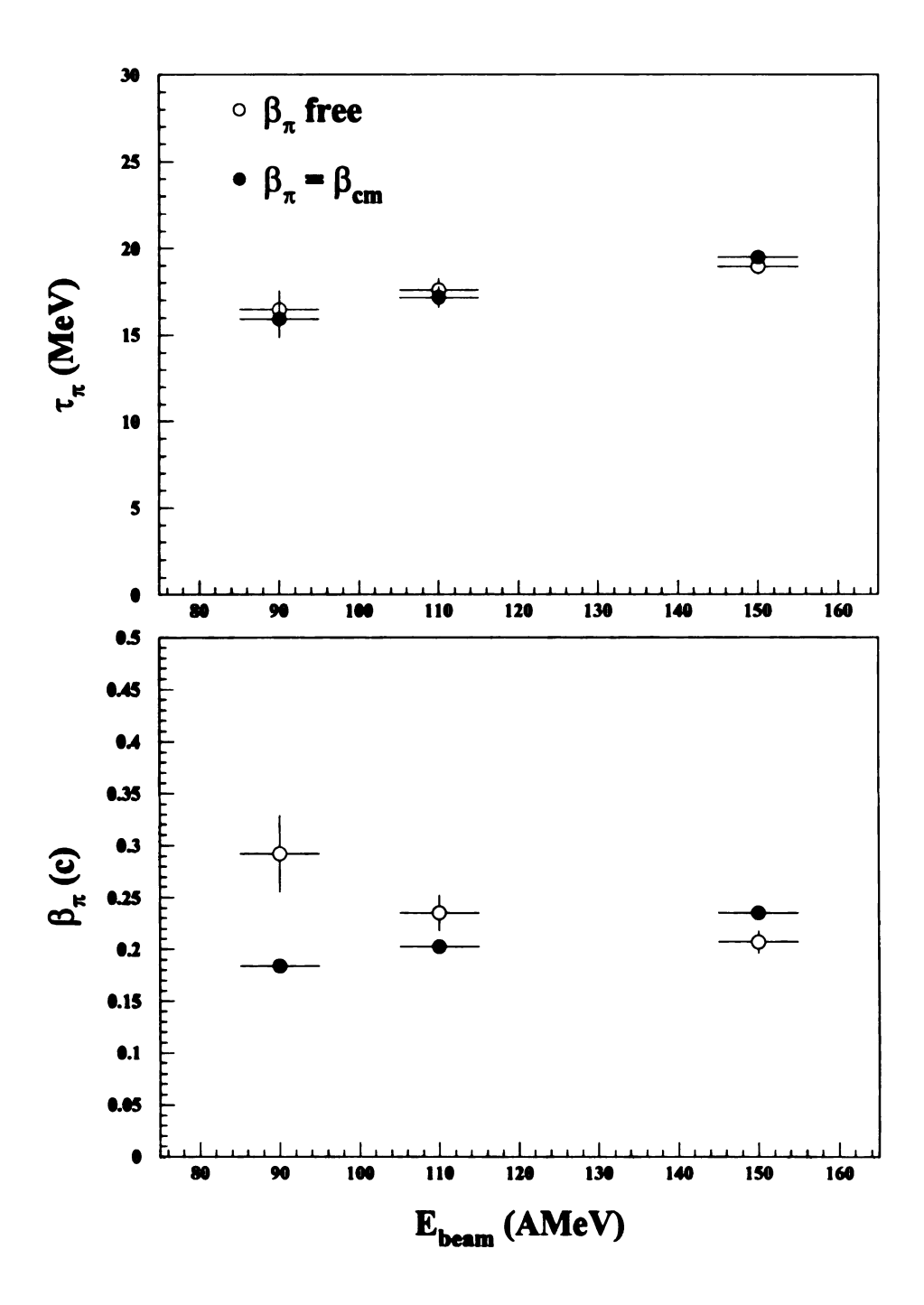


Figure 4.10: Beam energy dependence of pion source velocity and slope parameter.

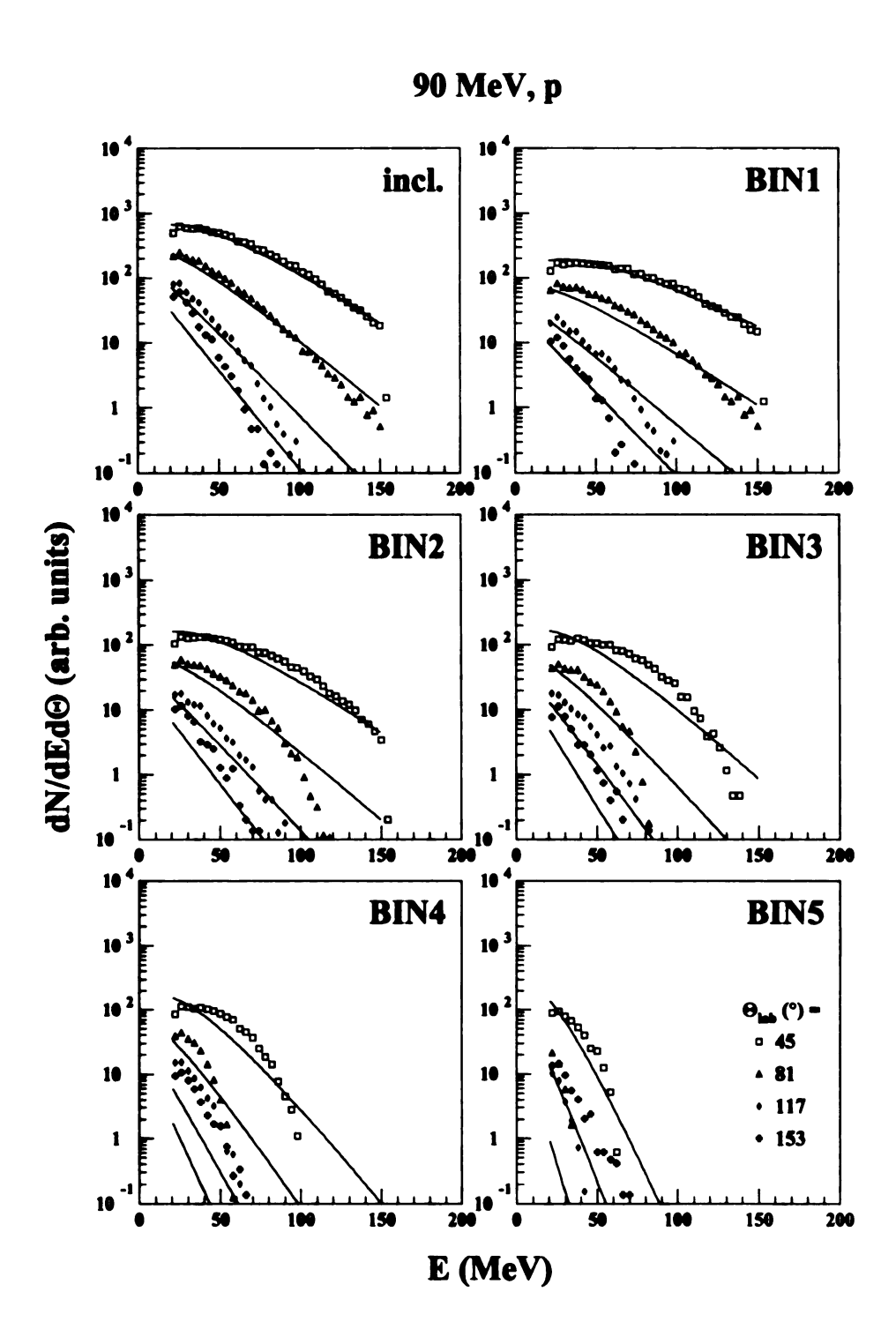


Figure 4.11: Proton kinetic energy distributions at 90 AMeV for several angles and centrality bins.

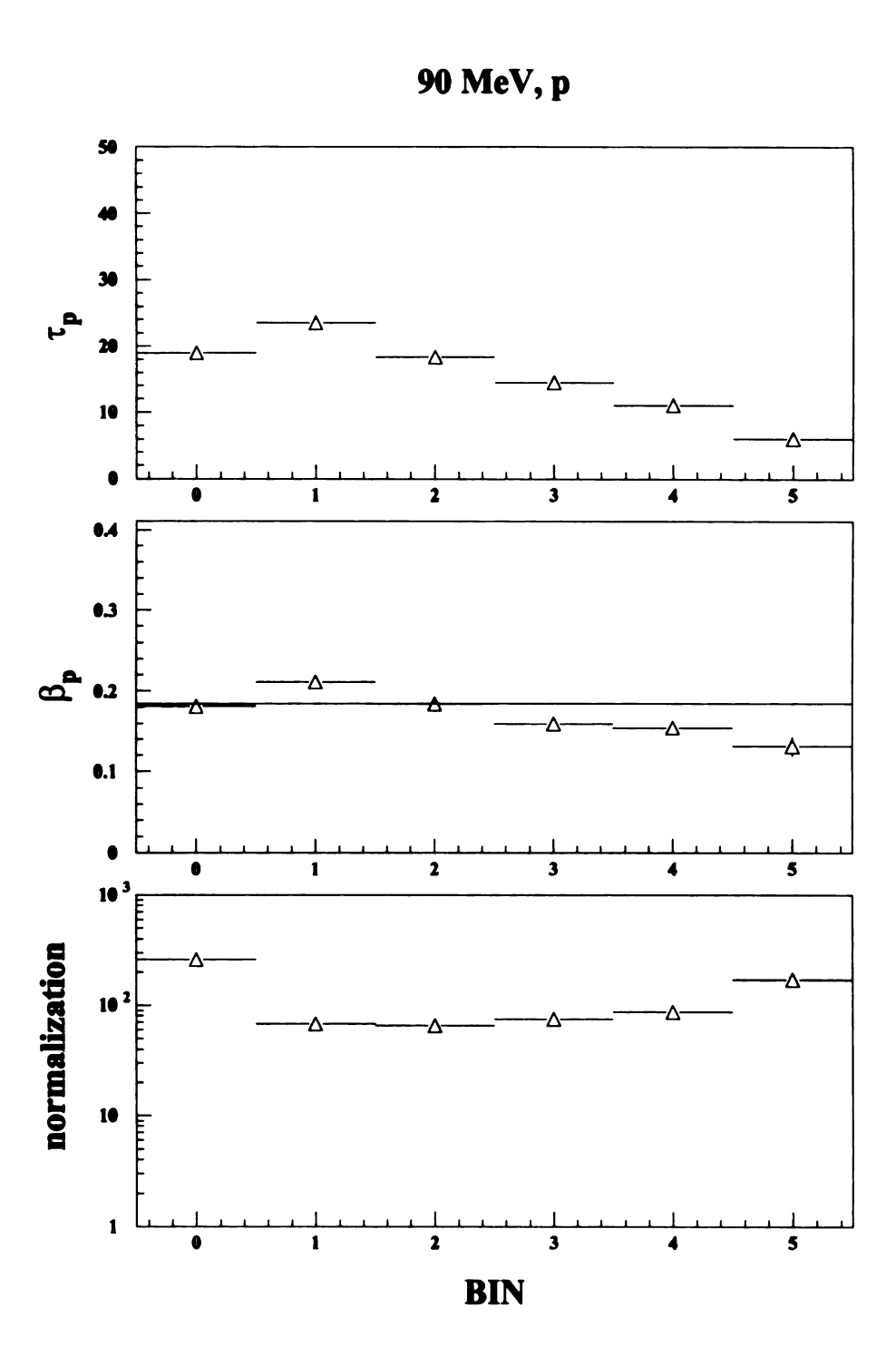


Figure 4.12: Resulting fit parameter from a moving source fit to a Maxwell-Boltzmann distribution at 90 AMeV. The solid line in the middle frame indicates the value of  $\beta_{cm}$ . All statistical errors are smaller than the symbol size.

(increasing impact parameter) and decreasing beam energy. The solid lines in the upper panel are the  $\tau_p$  values extracted from BUU calculations at the three different beam energies. In the bottom panel the solid lines are at the values of  $\beta_{cm}$ .

As a last step in the analysis of the spectral shapes for kinetic energy distributions we compare in Figures 4.14 and 4.15 the experimental results for 150 AMeV with the filtered BUU results. In both figures the 2-dimensional spectra are normalized to unity for angles between 45° and 153°. The energies considered for the normalization are 10 – 150 MeV and 20 – 150 MeV for pions and protons respectively. The proton spectra are well reproduced at all angles for the more central bins. In peripheral collisions the shapes for backward angles are still in good agreement, whereas for the forward angles the data drops much faster than the calculations. For the pions the agreement is relatively good for the higher pion energies, whereas for the lower ones the calculations under-predict the data by a factor of two.

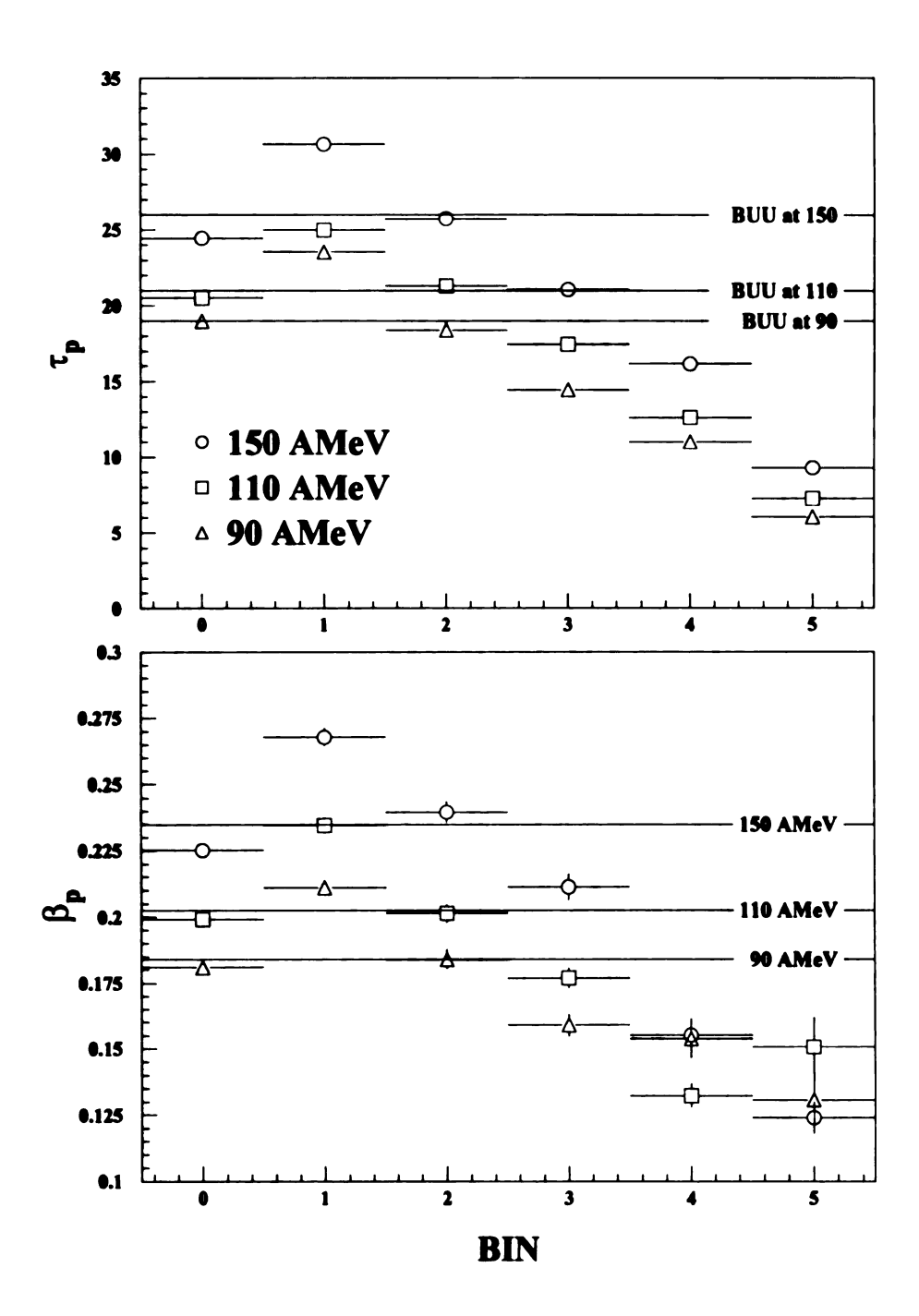


Figure 4.13: Beam energy dependence of proton source velocity and slope parameter. All statistical errors are smaller than the symbol size.

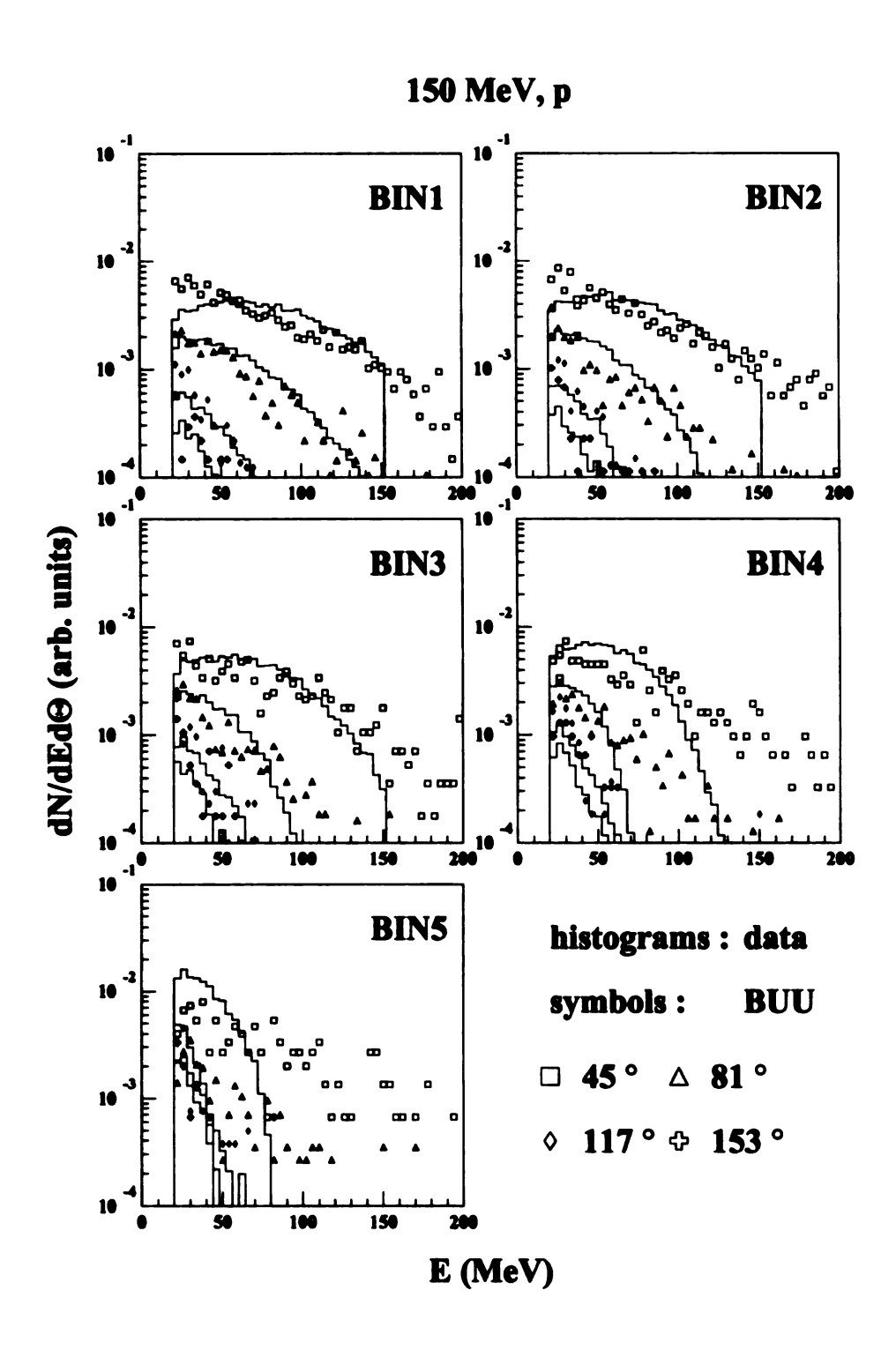


Figure 4.14: Comparison of kinetic energy spectral shapes with BUU calculations for protons at 150 AMeV.

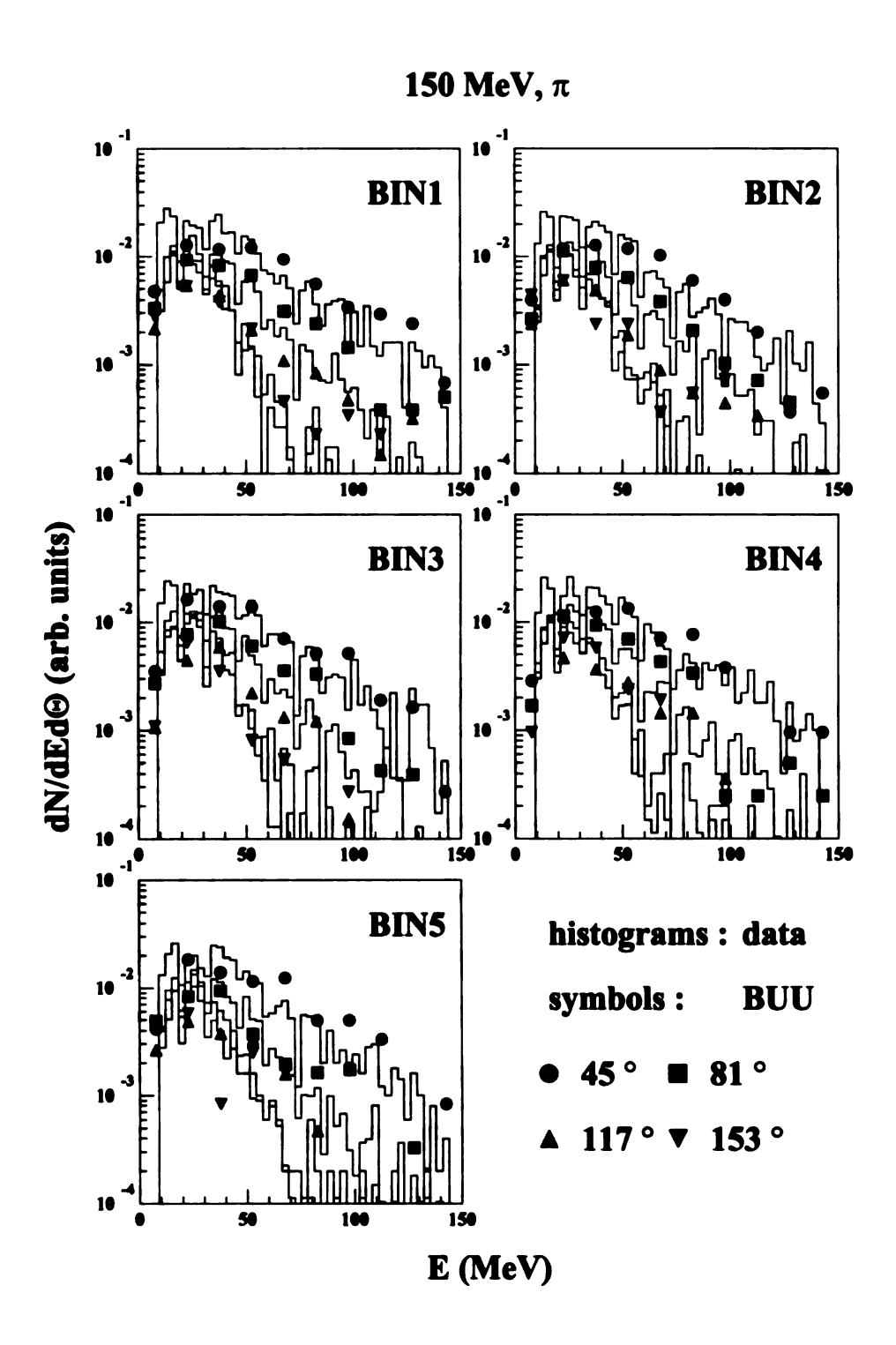


Figure 4.15: Comparison of kinetic energy spectral shapes with BUU calculations for pions at 150 AMeV.

# Chapter 5

# Azimuthal Distributions and Transverse Flow

### 5.1 Introduction

In the study of the properties of hot, exited nuclear matter it is important to separate collective effects from statistical ones. Collective effects such as rotation or collective expansion can distort certain experimental quantities such as kinetic energy spectra and severly affect the results obtained from model comparisons to the data [Hsi 94].

One of the goals for this experiment was to investigate the azimuthal correlations and the possibility of transverse flow for pions produced below the free nucleon-nucleon threshold. The azimuthal correlation, or the relative azimuthal angle of emitted nuclear particles with respect to the reaction plane of the event, can give a picture of the event shape in momentum space. Preferential emission in (or out of) the reaction plane can be easily identified. After having found an approximate reaction plane, the transverse motion in that plane can be determined for different particle types and give a representation of the event shape.

Since for such kind of analysis it is important to have good event characterization one needs to record the properties of as many particles in the events as possible. The  $4\pi$  Array with its large solid angle coverage is well suited for this type of experiment at intermediate energies and results for several such experiments have been published [Wils 92, West 93].

In this experiment the small system size and the relatively high beam energies put some restrictions on the completeness of the event characterization. The total system mass in the  $^{20}$ Ne +  $^{27}$ Al reaction is only 47 amu, with the total charge being 23. This results in rather low multiplicities in the events. For example, the average number of charged particles in inclusive events is only about 4 at all three bombarding energies. The average number of intermediate mass fragments (Z > 2) varies from 0.11 at 150 AMeV to .26 at 90 AMeV. Since both azimuthal correlations and transverse flow are much stronger for heavier particle types, these low numbers affect the analysis.

### 5.2 Azimuthal Correlations

For the determination of the reaction plane in nuclear collisions several methods have been devised. In general these methods rely on either some collective motion of nuclear matter [Cugn 83, Dani 83, Dani 85, Wils 92] or the detection of projectile like fragments (see e.g. [Schu 94]).

For the analysis in this experiment, we use a slightly modified version of the azimuthal correlation method [Wils 92] to determine the reaction plane. The angle of the approximate reaction plane with respect to the x-axis in the laboratory frame  $\Phi_{RP}$  is found by minimizing the sum of the squared distances of the transverse momenta of all particles in an event to a common axis with slope A. In order to avoid autocorrelations, reaction planes have to be determined for every particle in the event by excluding that particle of interest (POI). Because of the exclusion of the POI we require a minimum charged particle multiplicity of  $N_{ch} \geq 3$ . This is at the same time

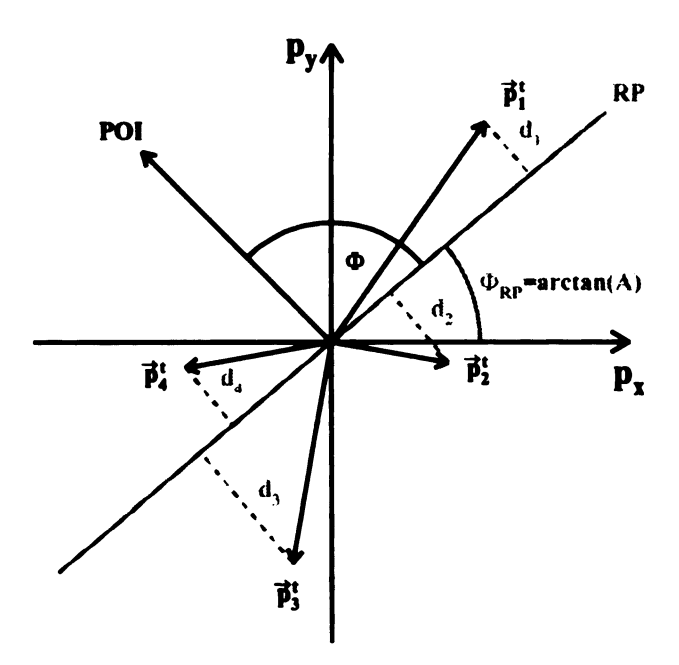


Figure 5.1: Reaction plane determination using azimuthal correlations. The particle of interest is POI, the reaction plane is RP and  $\vec{p}_i^t$  are the remaining particles in the event.

the only restriction on the impact parameter of the reaction. The above procedure will only give the value of the slope of the common axis but not the orientation along that axis. Whereas the original method used the transverse momentum method to determine the forward (positive) side of the reaction plane, the modified method calculates a weighted projection of the transverse momenta onto the found axis, i.e.

$$P_A = \sum_i \omega_i \vec{p_i} \cdot \vec{A},$$

where  $\vec{A}$  is a unit vector along the direction of A and  $\omega_i$  is +1(-1) for particles with positive(negative) cm rapidities. The orientation of  $\vec{A}$  is given by the requirement that  $-90^{\circ} \leq \Phi_{\rm RP} \leq +90^{\circ}$ . The forward side of the reaction plane can now be determined by the sign of  $P_A$  and does not rely on the transverse momentum method. A schematic diagram showing the involved quantities is given in Figure 5.1. This modified method has also been used in another recent experiment and yields distributions very similar to the original method [Pak 95].

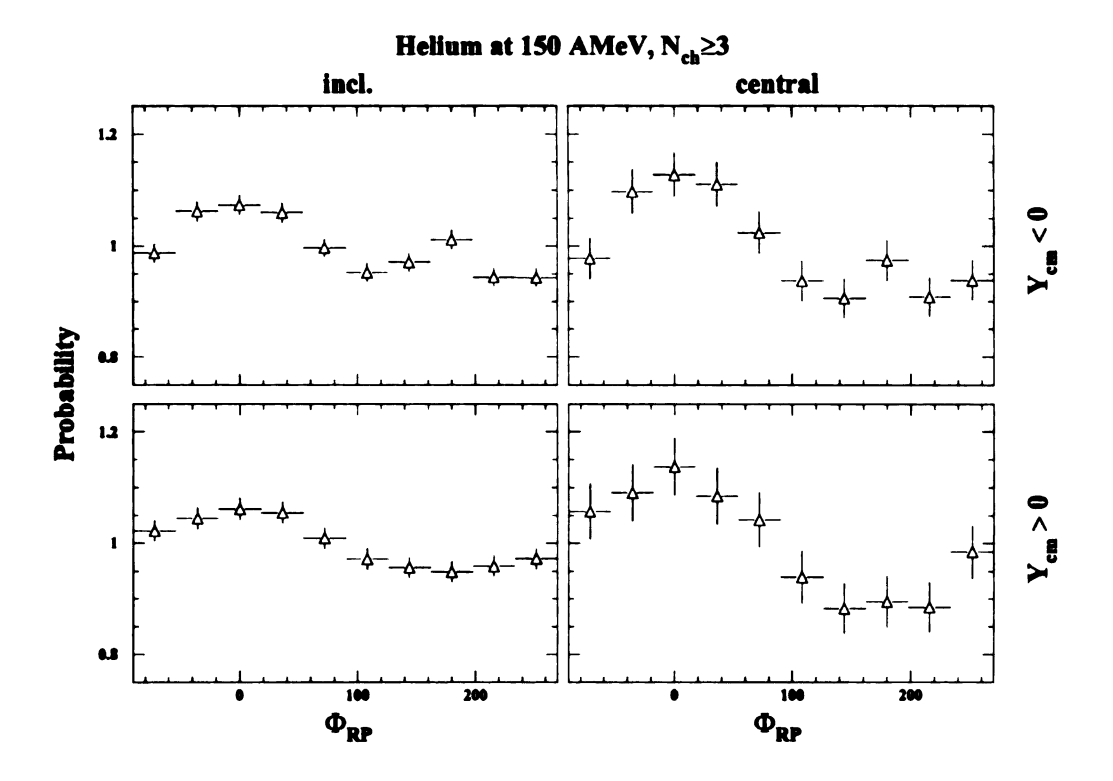


Figure 5.2: Azimuthal angle distributions with respect to the approximate reaction plane for He ions at 150 AMeV.

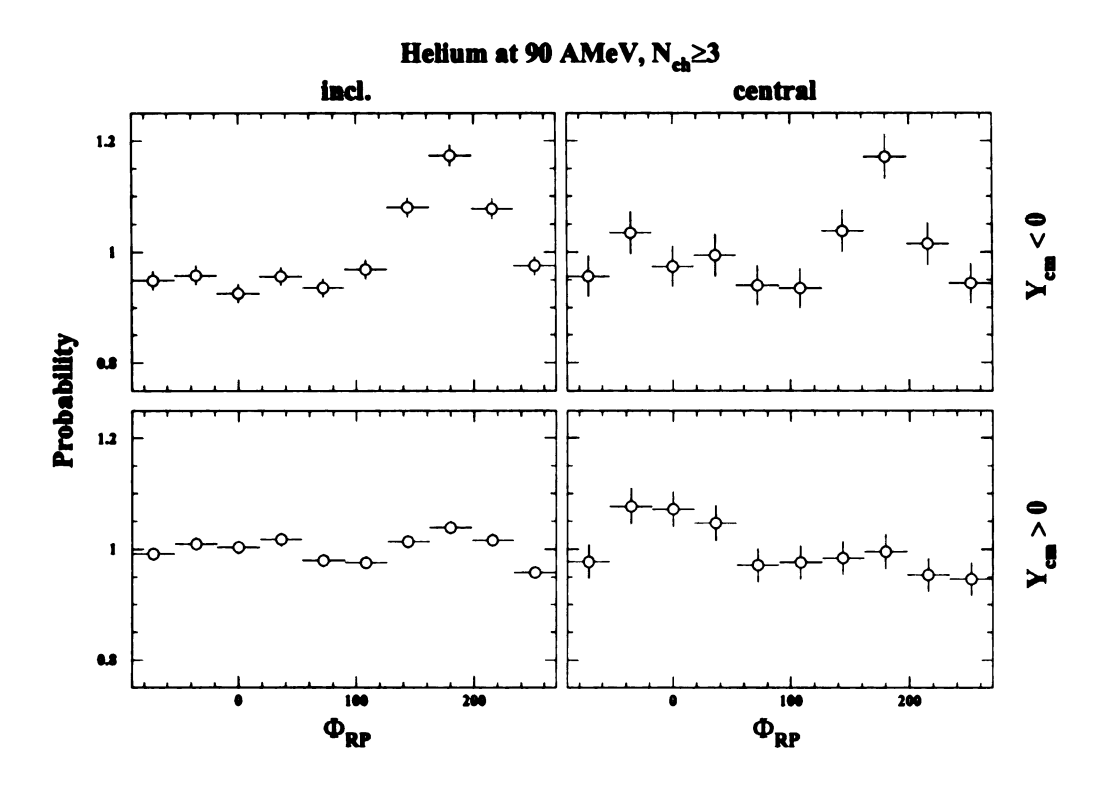


Figure 5.3: Same as Figure 5.2 for 90 AMeV.

In Figures 5.2 and 5.3 we present the azimuthal distributions with respect to the reaction plane for helium ions for the energies of 150 AMeV and 90 AMeV. In each figure the two panels on the left are for impact parameter inclusive events, whereas the two on the right are obtained for events within a 10% central cut on KE<sub>t</sub>. The upper two are for backward, the lower two for forward center of mass rapidities of the particle of interest. One effect that can be seen is that the centrality cut enhances the correlation more for the higher beam energy. Whereas for the lower beam energy the central distributions show a peak in the negative side of the reaction plane for backward rapidities and a peak in the positive side for forward rapidities – as expected for an ellipsoidal shape in momentum space, the data at 150 AMeV show a persistent peak in the forward side even for the backward rapidities. The application of a recoil-correction [Wils 92] has no effect on these distributions, since all the particles have relatively small masses. The distributions for 110 AMeV are somewhere between the ones for 90 and 150 AMeV.

The distributions for protons and pions in central events at 150 AMeV are displayed in Figure 5.4. Similar to the helium data the protons show an in-plane enhancement in the forward side of the plane for both rapidity gates. As far as the pions are concerned the statistical errors tend to be rather large for these cuts, but at forward rapidities a possible enhancement in the forward (positive) side of the plane along with a suppression in the backward (negative) side can be seen. For all of the more inclusive cuts, either in rapidity or centrality, the distributions are flat within the error bars. Also, at the two lower beam energies the distributions for protons show no correlation and for pions the errors are even larger than for 150 AMeV and no correlation can be seen.

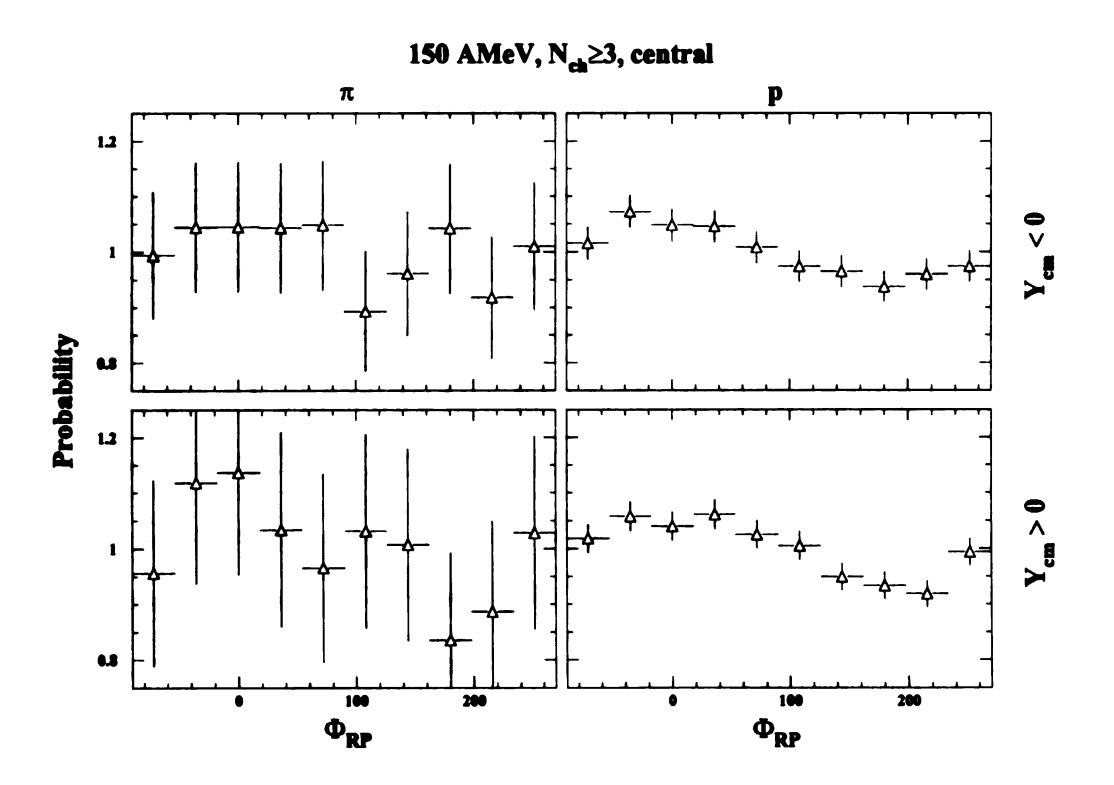


Figure 5.4: Azimuthal angle distributions with respect to the approximate reaction plane for pions and protons from central events at 150 AMeV.

### 5.3 Transverse Flow

One important collective mode is transverse directed flow. This mode is a collective motion of the nuclear matter in the reaction plane and is observed in reactions at both high [Dani 88, Gust 84, Gutb 89] and [Ogil 89, Sull 90, West 93] low bombarding energies.

In general the interpretation is [Moli 85] that at low relative energies the attractive part of the nuclear potential is probed resulting in negative scattering angles, whereas for high (relativistic) energies the repulsive hard core interaction dominates the collision yielding positive flow angles. Since in an experiment only the absolute value of the flow angle can be determined, that value should go through a minimum at a bombarding energy, termed the balance energy  $E_{bal}$ , where the scattering angle crosses zero. Several experiments have been performed to study that disappearance of transverse flow [Ogil 89, Krof 89, Sull 90, Zhan 90]. One publication [West 93] reports the balance energies as a function of the combined system mass. One of the systems measured was Ne + Al, where the balance energy was found to be around 110 AMeV. Since transverse flow for pions has been observed at beam energies of 800 AMeV [Goss 89] and was found to be positive (same direction as fragments) for all rapidities, we hoped to be able to determine the flow for subthreshold pions at energies on either side of the balance energy of 110 AMeV.

Figures 5.5 to 5.7 display the average normalized transverse momentum in the reaction plane  $\langle P_x/P_t \rangle$  as a function of center of mass rapidity  $Y_{\rm cm}$  for helium, protons and pions for the three beam energies. All distributions are for a 10% central cut in KE<sub>t</sub>. In all three figures the values of the projectile and target rapidities are indicated by arrows. The cm rapidity is marked by a vertical line at  $Y_{\rm cm}=0$ . Whereas for helium the typical "S"-shaped curves are observed below and above the

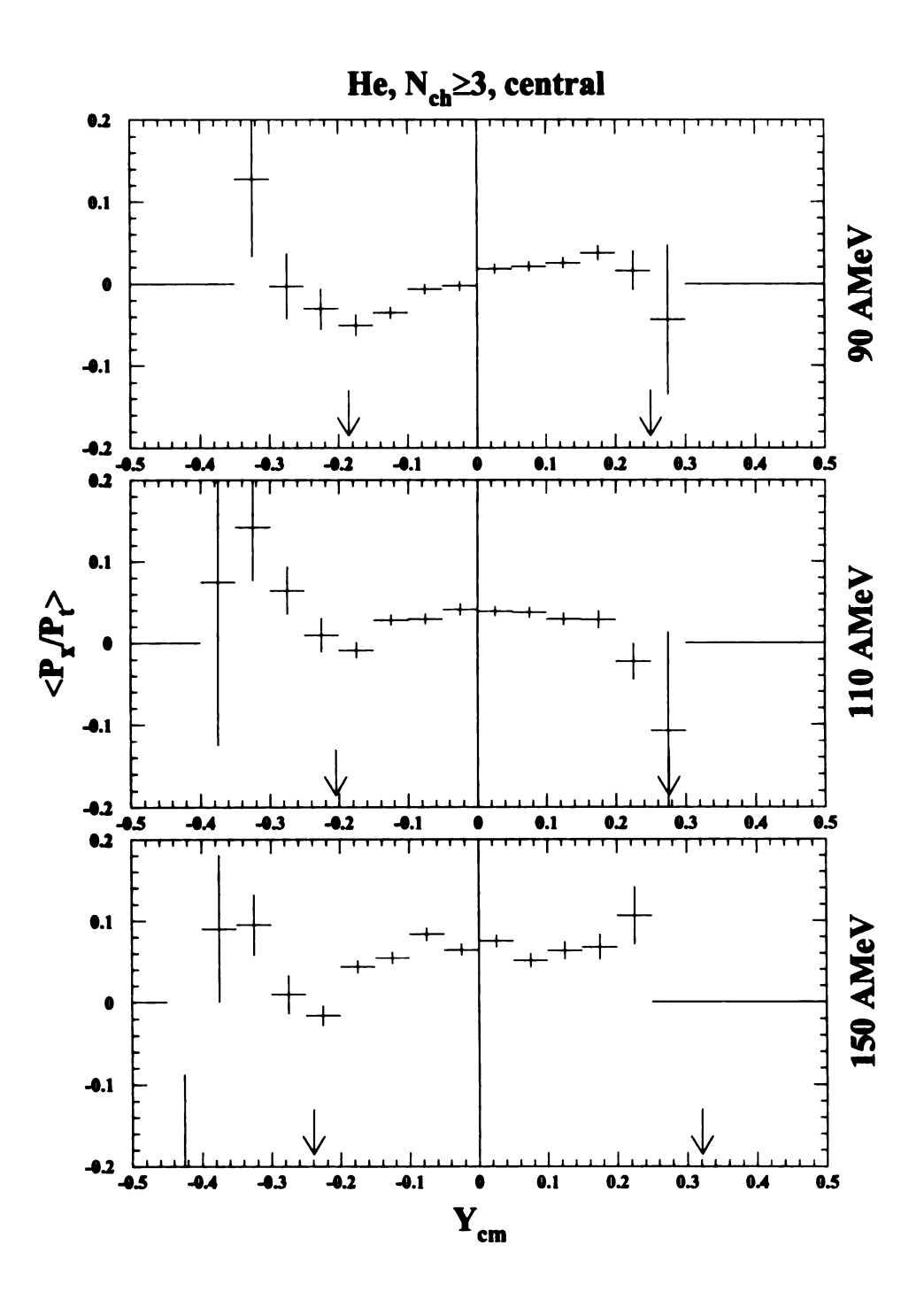


Figure 5.5: Average transverse momentum in the reaction plane as a function of rapidity for helium at the three different beam energies. The arrows indicate the target and projectile rapidities. The balance energy is 110 AMeV.

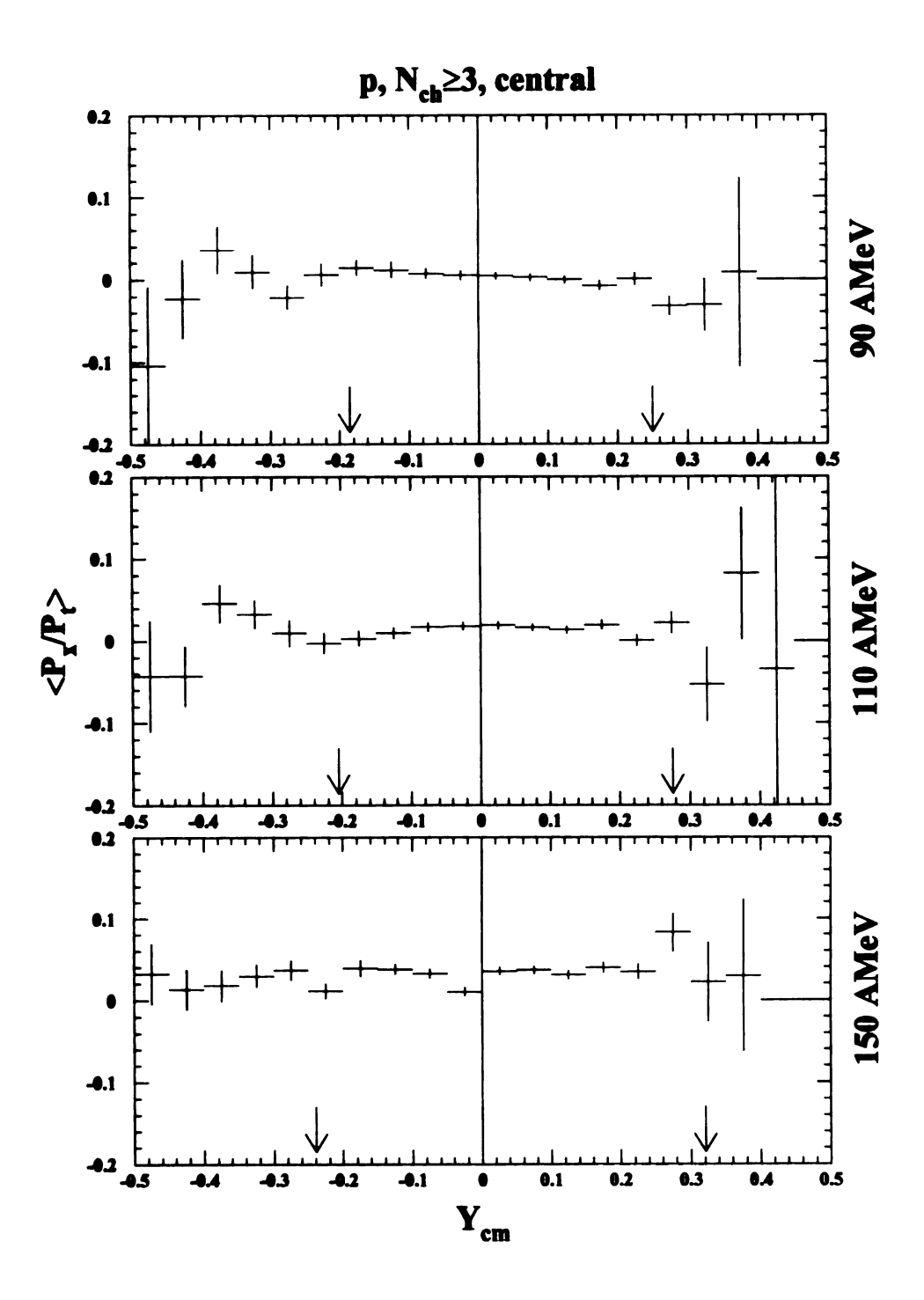


Figure 5.6: Same as Figure 5.5 for protons.

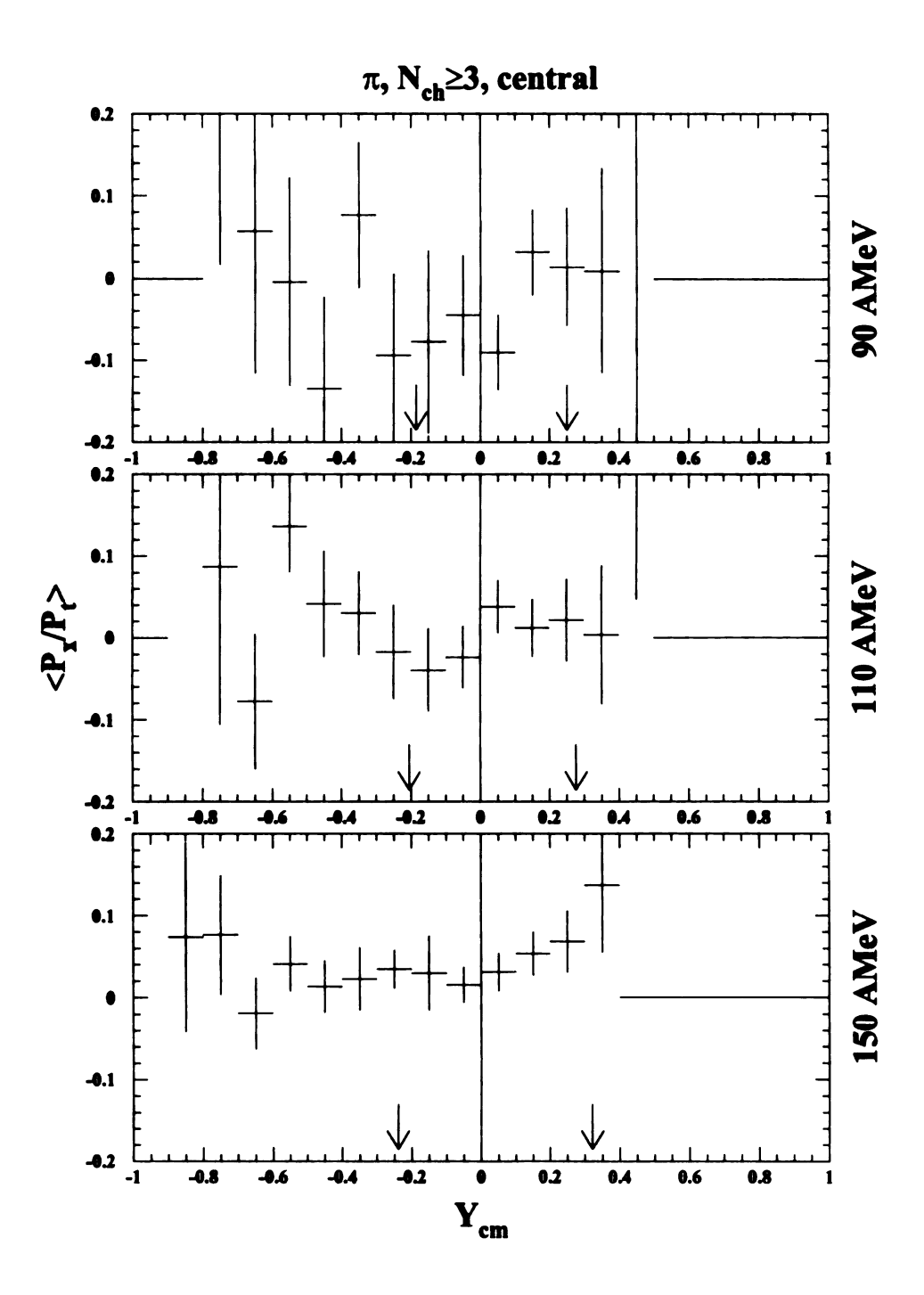


Figure 5.7: Same as Figure 5.5 for pions.

balance energy, the data for protons are flat for all beam energies. In fact the data at 90 AMeV show a slightly negative slope. This does not present a problem, since the slopes for all higher charges are positive. The distributions for pions at the two lower beam energies are strongly affected by the centrality cut. The statistical errors are too large to allow the extraction of a slope at midrapidity. For the 150 AMeV the statistics is much better and a sharp rise at positive rapidities is seen, indicating a preferred emission in the projectile direction. The fact that above a rapidity of  $Y_{\rm cm} \approx 0.4$  the  $\langle P_x/P_t \rangle$  is zero is only due to the missing acceptance for pion detection at polar angles below  $45^{\circ}$ .

To summarize the values of the slopes at midrapidity for the three particle types, we show in Figure 5.8  $d < P_x/P_t > /dY_{\rm cm}|_{Y_{\rm cm}=0}$  as a function of beam energy. Again, due to the large statistical errors at the lower two beam energies, no values for pions are reported for these.

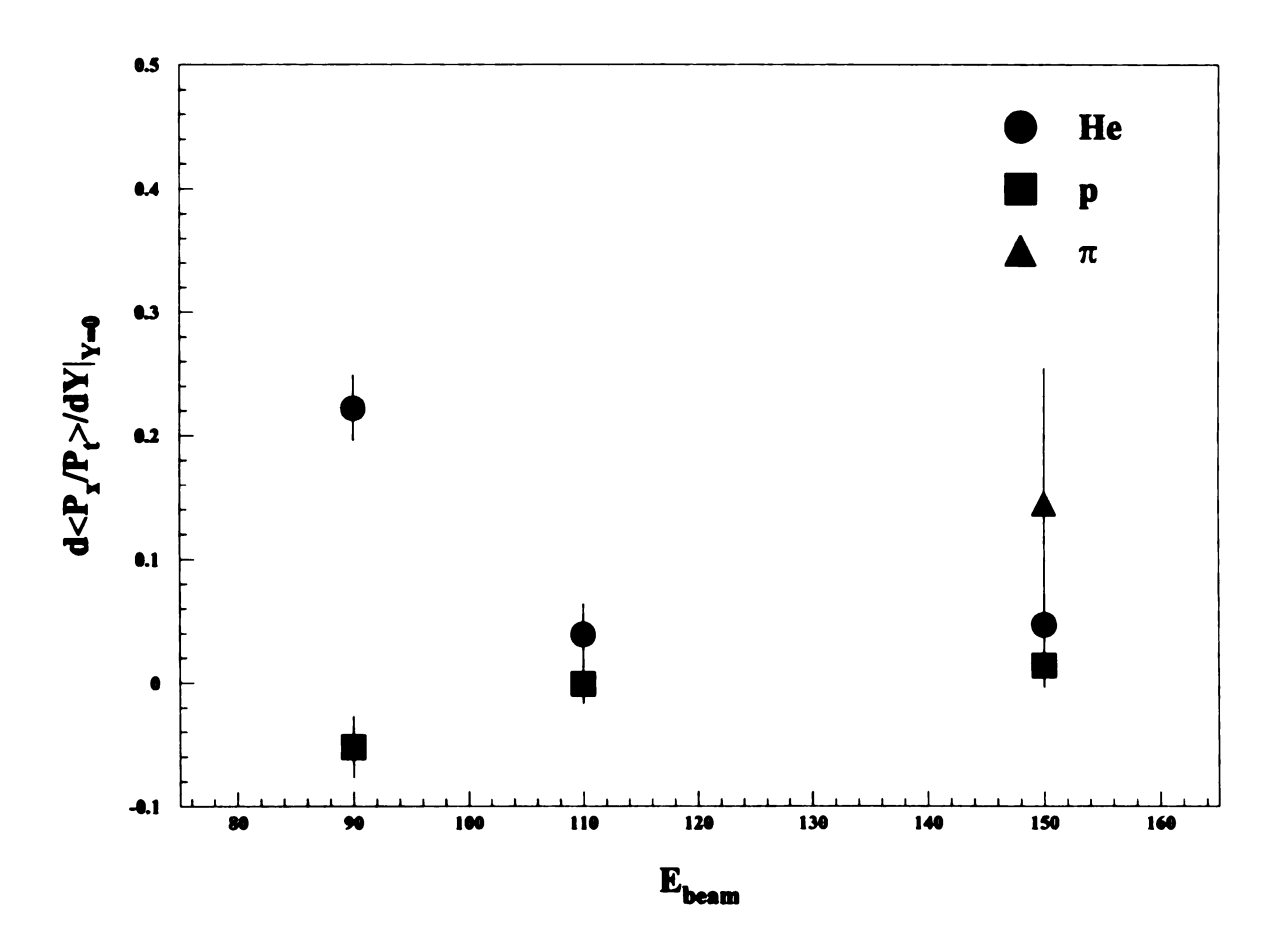


Figure 5.8: Slopes of the average transverse momentum in the reaction plane at midrapidity. Due to the large statistical errors at the lower two beam energies, no values for pions are reported for these.

### Chapter 6

### **Conclusion**

The production of positively charged pions below the free nucleon-nucleon threshold in intermediate energy heavy ion collisions was investigated. The system studied was  $^{20}$ Ne +  $^{27}$ Al at bombarding energies of 90, 110 and 150 AMeV. Pions and nuclear fragments were detected using the MSU  $4\pi$  Array yielding complete event characterization.

#### Pion detection and identification

The pions were detected using fast/slow phoswich  $\Delta E/\mathrm{E}$  detectors for polar angles from 18° to 162° and all azimuthal angles. The separation of the pion signal from the background is accomplished by using the delayed  $\mu^+ \to e^+$  decay in the pion decay chain. That decay can be easily detected in the phoswich detectors. Unfortunately the background contamination at angles below 45° is too large to extract reliable pion signals. The absolute cross section for pion production is not readily available due to the method of identification.

#### Pion event centrality

The fragment information from the  $4\pi$  Array was used to determine the centrality of pion producing events. A surprising enhancement of the production cross section

for peripheral events was found when compared to BUU model calculations. The nuclear equation of state used for the calculations has no impact on the number of pions produced for any given impact parameter. The peripheral enhancement seems to be independent of the observable chosen to determine the centrality. The similarity of inclusive and pion gated impact parameter distributions is found to increase with decreasing beam energy, suggesting more cooperative phenomena for the production of pions at subthreshold energies.

#### Polar angle distributions and kinetic energy spectra

The polar angle distribution in the laboratory frame shows the expected forward focussing, increasing with particles mass. For pions, strong effects of target shadowing are found. Both proton and pion distribution are very well reproduced with BUU model calculations after taking into account the detector acceptance. An analysis of the kinetic energy spectra in terms of a classical Maxwell-Boltzmann source, yields pion and proton temperatures well within the systematics for similar systems and are reproduced by BUU model calculations. The pions temperatures show no dependence on the impact parameter of the collision, as can be expected for emission from a completely thermalized source. For protons a significant decrease in the extracted temperatures with increasing impact parameter is observed. The spectral shapes are well reproduced by BUU calculations for central events. For low energy pions the data are under-predicted by about a factor of 2.

#### Azimuthal distributions and transverse flow

Azimuthal distributions with respect to the estimated reaction plane were found to be more strongly correlated with that plane for heavier particles. The correlation for pions from central events shows a weak in-plane emission in the forward direction for the highest beam energy. At the two lower beam energies, as well as for more inclusive cuts, no correlations are found.

The average transverse momentum in the reaction plane as a function of rapidity shows the typical "S"-shaped curves for helium fragments, both below and above the balance energy. For protons the data show only flat distributions at a value close to zero, which is expected for light particles at energies rather close to the balance energy. For pions, on the other hand, a steep rise at forward rapidities is found at the highest bombarding energy, indicating a preferred emission towards the nuclear matter flow. At the two lower energies the statistics do not allow any conclusions.

# Appendix A

# **Impact Parameter Selection**

### A.1 Method

In experimental studies of nuclear reactions it is highly desirable to determine the (approximate) impact parameter on an event by event basis. This becomes especially important when comparisons with theoretical model calculations are necessary, since these usually require the impact parameter as one of the inputs. Whereas the exclusive measurement of events of a certain class, such as peripheral or central, can usually be achieved with few specialized detectors, the classification of all possible events according to their centrality requires recording as much information about the particles in an event as possible. For that purpose  $4\pi$  detectors, such as the MSU  $4\pi$  Array are well suited. While the impact parameter of a nuclear collision is not directly accessible from an experiment, several "centrality" variables have been shown to be correlated with impact parameter [Cava 90, Phai 92]. The observables used in this experiment are the number of charged particles  $N_{ch}$ , the number of light charged particles  $N_{lcp}$ , midrapidity charge  $Z_{mr}$  and the total transverse directed kinetic energy  $KE_t$ .

The number of light charged particles is defined to include only particles of  $Z \leq 2$ . Both  $N_{ch}$  and  $N_{lcp}$  do not include the pion that might be produced. The midrapidity charge is the sum of the charges of particles with a center of mass rapidity y' between one half the target and projectile cm rapidity, i.e.

$$.5y'_{\mathsf{ta}} \le y' \le .5y'_{\mathsf{pr}}.\tag{A.1}$$

Again pions are not counted in Z<sub>mr</sub>. Since kinetic energy is not a directed quantity, the transverse kinetic energy is derived from transverse momentum, i.e.

$$KE_{t} = \sum_{i} \frac{p_{t,i}^{2}}{2m_{i}}.$$
 (A.2)

In order to obtain the approximate impact parameter from these variables, the geometrical prescription of Reference [Cava 90] is used. It is assumed that a given observable q is monotonically related to the impact parameter b in a way that

$$\frac{2\pi bdb}{\pi b_{max}^2} = \pm f(q)dq,\tag{A.3}$$

with  $b_{max}$  being the maximum impact parameter of the reaction and f(q) the probability density function of q. That is f(q)dq is the probability of detecting a collision with a value of q between q and q + dq. The function f(q) is therefore normalized to unity. The plus (minus) sign indicates an increase (decrease) of q with increasing b. Integration of equation A.3 from a given b to  $b_{max}$  yields

$$\int_{b}^{b_{max}} \frac{2\pi b db}{\pi b_{max}^{2}} = \pm \int_{q(b)}^{q(b_{max})} f(q') dq'. \tag{A.4}$$

If we define

$$F(q) = \pm \int_{q(b)}^{q(b_{max})} f(q')dq',$$
 (A.5)

then

$$b/b_{max} = \sqrt{1 - F(q)}. (A.6)$$

Using equation A.6 one can easily obtain an estimate for the impact parameter in any given event. In practice, we divide the possible values of the observable q into

Table A.1: Impact parameter values for bins in KE<sub>t</sub>

i	$F(KE_t)$	ĥ	$\hat{b}_l$	$<\hat{b}>$	$\hat{b}_u$	j
1	1.0	0.00	0.00	0.32	0.45	1
2	0.9	0.32	0.00	0.02	0.40	1
3	0.8	0.45	0.45	0.55	0.63	2
4	0.7	0.55	0.40	0.00	0.03	2
5	0.6	0.63	0.63	0.71	0.77	3
6	0.5	0.71	0.03	0.71	0.11	3
7	0.4	0.77	0.77	0.84	0.89	4
8	0.3	0.84	0.77	0.04	0.03	4
9	0.2	0.89	0.89	0.95	1.00	5
10	0.1	0.95	0.09	0.90	1.00	٦

a number of bins with an equal number of events in each bin. For these bins we find the appropriate F(q) by integrating the distribution function f(q).

Figure A.1 shows the distributions of the four "centrality" observables used in this experiment. On the left the probability densities f(q) are shown. The hatched areas under the curves indicate the bins for each variable. In the case of  $KE_t$  there are ten bins. For the other three variables only four bins are used, since the limited range of values does not allow for a finer distinction. Even for four bins the resulting integrated numbers of events in each bin, displayed on the right, is not constant, as it is the case for  $KE_t$ . Here all bins have approximately the same number of events and the normalized distribution is flat at a value of .1. In the later stages of the analysis these bins can be grouped to yield any possible cut on centrality. For the comparison with model calculations in Chapter 3 the bins in centrality are grouped in pairs of two so that an estimate of impact parameter can be made for the center of the bin as well as for the upper and lower limit. The resulting values for  $\hat{b} = b/b_{max}$  obtained for the different observables are listed in Tables A.1 to A.4.

As the final step in the determination of an approximate impact parameter one

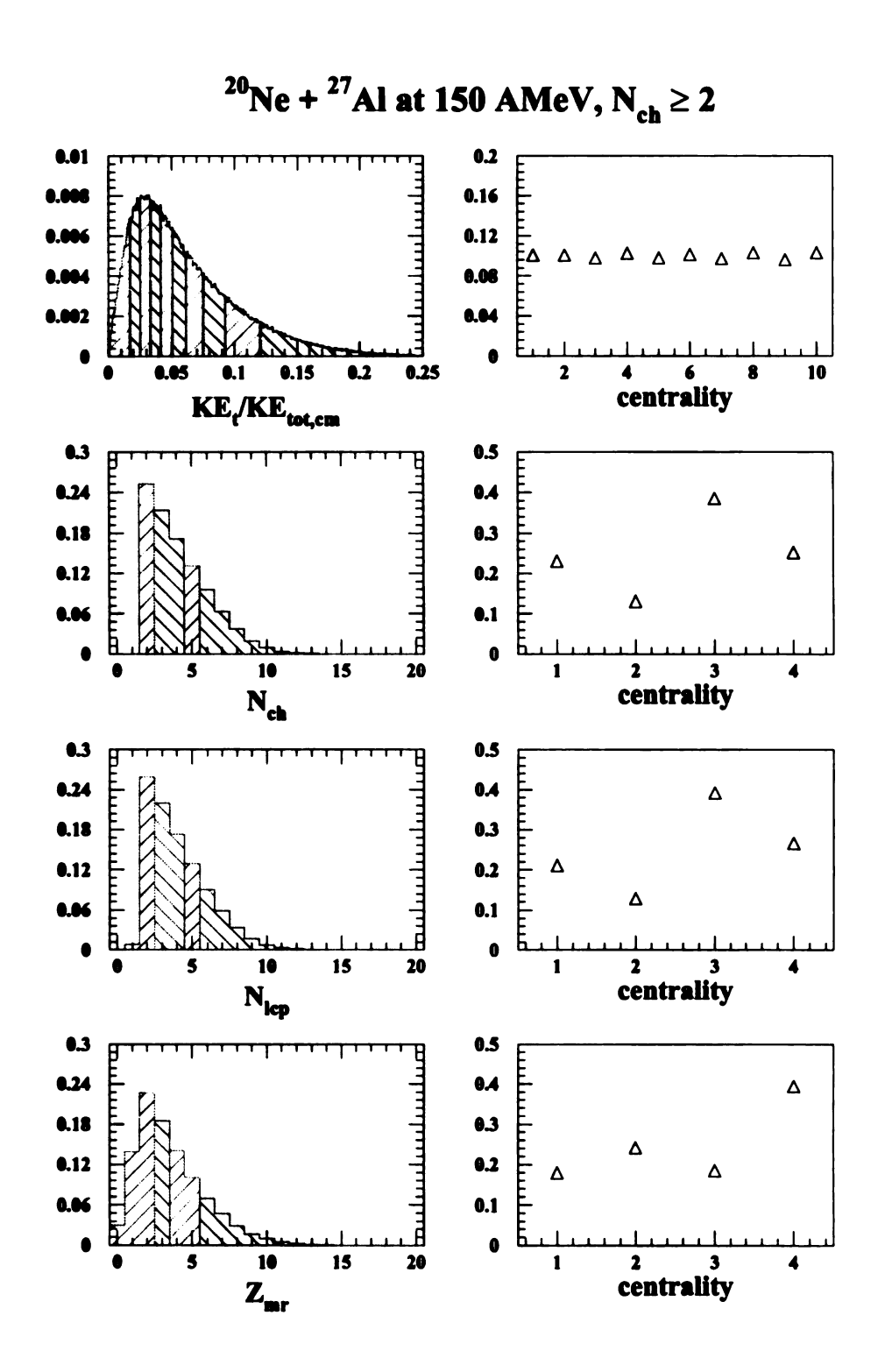


Figure A.1: Probability distributions for centrality observables.

Table A.2: Impact parameter values for bins in N<sub>ch</sub>

i	$F(\mathrm{N_{ch}})$	$\hat{b}$	$\hat{b}_l$	$<\hat{b}>$	$\hat{b}_u$	$oxed{j}$
1	1.00	0.00 0.56	0.00	0.56	0.69	1
2	0.68	0.56	0.00	0.50	0.03	1
3	0.52	0.69	0.69	0.92	1.00	2
4	0.16	0.92	0.03	0.32	1.00	2

Table A.3: Impact parameter values for bins in  $N_{\rm lcp}\,$ 

i	$F(\mathrm{N_{lcp}})$	$\hat{b}$	$\hat{b}_l$	$<\hat{b}>$	$\hat{b}_u$	j
$\begin{bmatrix} 1 \\ 2 \end{bmatrix}$	1.00 0.72	0.00 0.53	0.00	0.53	0.67	1
3 4	0.56 0.18	0.67 0.91	0.67	0.91	1.00	2

Table A.4: Impact parameter values for bins in  $Z_{mr}$ 

i	$F(\mathbf{Z_{mr}})$	ĥ	$\hat{b}_l$	$<\hat{b}>$	$\hat{b}_u$	j
1	1.00	0.00 0.54	0.00	0.54	0.76	1
2	0.71	0.54	0.00	0.01	0.10	1
3	0.43	0.76	0.76	0.86	1.00	ĭ.
4	0.26	0.86	0.10	<b>0.00</b>	1.00	3

needs to obtain an estimate for  $b_{max}$ . Since the experimental hardware trigger condition naturally presents a centrality bias, one can estimate  $b_{max}$  by comparing the total cross sections of the trigger used in the data (EX) and a minimum bias trigger (MB). Assuming a geometrical cross section for the minimum bias trigger, i.e.

$$\sigma_{\rm MB} = \sigma_{\rm tot} = \pi (R_{pr} + R_{ta})^2 \tag{A.7}$$

with  $R_{pr}$  and  $R_{ta}$  being the projectile and target radii, we can write

$$b_{max} = \sqrt{\frac{\sigma_{EX}}{\sigma_{MB}}} (R_{pr} + R_{ta}). \tag{A.8}$$

The transverse kinetic energy distributions used for the above procedure are shown in Figure A.2 for 150 AMeV. The histogram labeled FA2M1 is the data taken with a hardware trigger requiring a minimum of two detector hits in the forward array and one identified charged particle in the whole array. It is assumed to be the minimum bias trigger for the experiment. The curve labeled B2M2 represents the trigger that was used for the data analysis. I required at least two phoswich detector hits in the main ball and also two identified particles in the whole array. The two histograms are normalized by minimizing the sum of the squared differences for values of the reduced KE<sub>t</sub> larger than 0.025. That value is where the B2M2 data has its maximum. The assumption here is that for values of KE<sub>t</sub><sup>red</sup> above the maximum the trigger bias becomes negligible. The ratio of the two cross sections is

$$R = \sqrt{\frac{\sigma_{B2M2}}{\sigma_{FA2M1}}} = 0.90. \tag{A.9}$$

Using  $R_{\rm pr} + R_{\rm ta} = 1.124 (A_{pr}^{1/3} + A_{ta}^{1/3}) = 6.42$  fm for the sum of projectile and target radii, we obtain  $b_{max} \approx 5.8$  fm from equation A.8, which turns out to be independent of the beam energy. Combining the values of  $\hat{b}$  from Table A.1 with the estimate for  $b_{max}$  we obtain average impact parameters of < b > = 2.0, 3.4, 4.4, 5.2 and 5.9 fm for the five centrality bins in KE<sub>t</sub>.

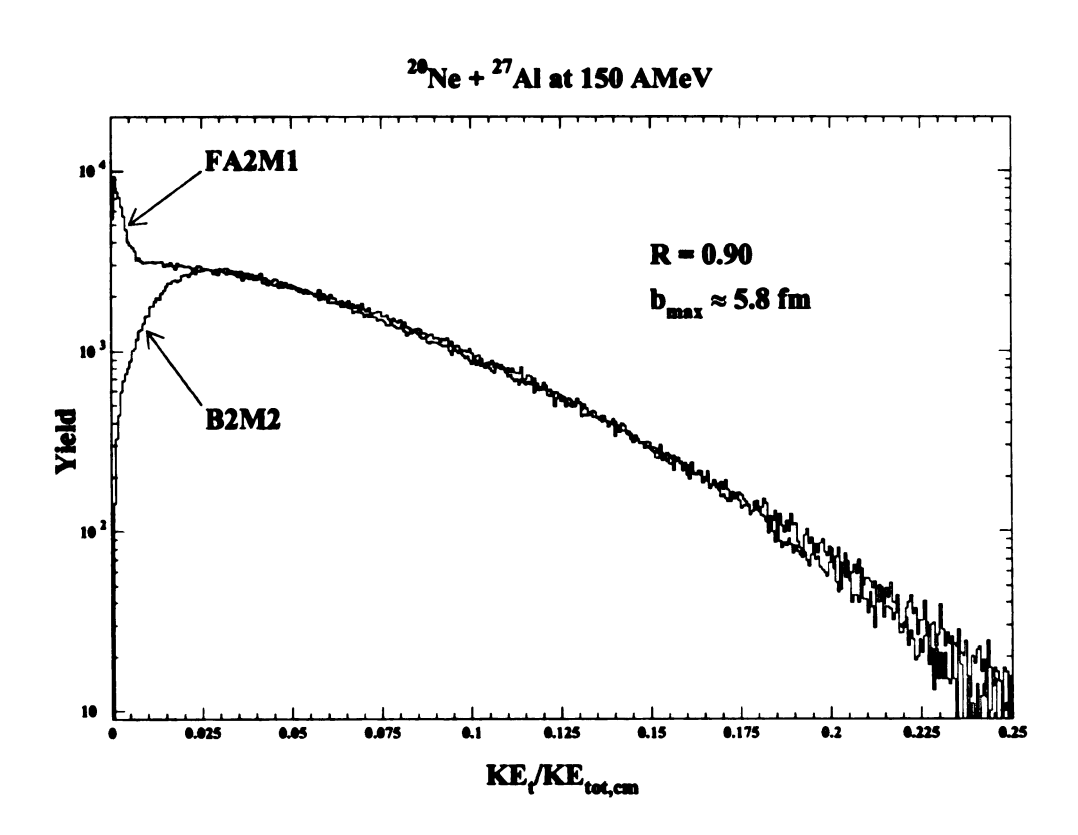


Figure A.2: Estimate of maximum impact parameter.

# **Bibliography**

- [Ador 92] A. Adorno, A. Bonasera, and J. Molitoris, LNS Preprint (1992).
- [Aiel 88] S. Aiello, A. Badalá, R. Barbera, S. Lo Nigro, D. Nicotra, A. Palmeri, G.S.
   Pappalardo, G. Bizard, R. Bougault, D. Durand, A. Genoux-Lubain, J.L.
   Laville, and F. Lefebvres, Europhys. Lett. 6, 25 (1988).
- [Bada 93a] A. Badalá, R. Barbera, A. Palmeri, G.S. Pappalardo, F. Riggi, A.C. Russo, C. Agodi, R. Alba, G. Bellia, R. Coniglione, A. Del Zoppo, P. Finocchiaro, C. Maiolino, E. Migneco, P. Piattelli, G. Russo, P. Sapienza, and A. Peghaire, Phys. Rev. C47, 231 (1993).
- [Bada 93b] A. Badalá, R. Barbera, A. Palmeri, G.S. Pappalardo, F. Riggi, and A.C. Russo, Z. Phys, A344, 455 (1993).
- [Bade 82] A. Baden, H.H. Gutbrod, H. Löhner, M.R. Maier, A.M. Poskanzer, T. Renner, H. Riedsel, H.G. Ritter, H. Spieler, A. Warwick, F. Weik, and H. Wieman, Nucl. Inst. and Meth. 203, 189 (1982).
- [Barb 90a] R. Barbera, A. Badalá, A. Adorno, A. Bonasera, M. Di Toro, A. Palmeri, G.S. Pappalardo, G. Bizard, R. Bougault, D. Durand, A. Genoux-Lubain, J.L. Laville, E. Lefebvres, J.P. Patry, G.M. Jin, and E. Rosato Nucl. Phys. A518, 767 (1990).
- [Barb 90b] R. Barbera, A. Badalá, A. Adorno, A. Bonasera, M. Di Toro, A. Palmeri, G.S. Pappalardo, F. Riggi, G. Russo, G. Bizard, D. Durand, J.L. Laville, G.M. Jin, and E. Rosato Nucl. Phys. **A519**, 231c (1990).
- [Barz 91] H.W. Barz, D.A. Cebra, H. Schulz and G.D. Westfall, Phys. Lett. **B267**, 317 (1991).
- [Baue 89] W. Bauer, Phys. Rev. C40, 715 (1989).
- [Baue 91] W. Bauer and B.-A. Li, Proc. of the Workshop pn Relativistic Aspects of Nuclear Physics, 1991, World Scientific.
- [Bene 79] W. Benenson, G. Bertsch, G.M. Crawley, E. Kashy, J.A. Nolen Jr., H. Bowman, J.G. Ingersoll, J.O. Rasmussen, J. Sullivan, M. Koike, M. Sasao, J. Péter, and T.E. Ward, Phys. Rev. Lett. 43, 683 (1979).

- [Bern 84] V. Bernard, J. Girard, J. Julien, R. Legrain, J. Poitou, A. Oskarsson, L. Carlén, H.-Å. Gustafsson, B. Jakobsson, P. Kristiansson, B. Norén, I. Otterland, H. Ryde, T. Johansson, G. Tibell, R. Bertholet, C. Guet, M. Maurel, H. Niefenecker, P. Perrin, F. Schussler, M. Buenerd, D. Lebrun, P. Martin, G. Løvhøiden, J.P. Bondorf, O.-B. Nielsen, and A. Palmeri, Nucl. Phys. A423, 511 (1984).
- [Birk 64] J.B. Birks, The Theory and Practice of Scintillation Counting, Pergamon Press, 1964, p. 194.
- [Brau 84] P. Braun-Munzinger, P. Paul, L. Ricken, J. Stachel, P.H. Zhang, G.R. Young, F.E. Obenshain, and E. Grosse Phys. Rev. Lett. **52**, 255 (1984).
- [Brau 87] P. Braun-Munzinger and J. Stachel, Ann. Rev. Nucl. Part. Sci. 37, 97 (1987).
- [Cava 90] C. Cavata, M. Demoulins, J. Gosset, M.-C. Lemaire, D. L'Hôte, J. Poitou, and O. Valette, Phys. Rev. C42, 1760 (1990).
- [Cebr 90] D.A. Cebra, Ph.D. Thesis, Michigan State University, 1990.
- [Cebr 90a] D.A. Cebra, S. Howden, J. Karn, A. Nadasen, C.A. Ogilvie, A. Vander Molen, G.D. Westfall, W.K. Wilson, J.S. Winfield, and E. Norbeck, Phys. Rev. Lett. 64, 2246 (1990).
- [Cebr 91] D.A. Cebra, S. Howden, J. Karn, D. Kataria, M. Maier, A. Nadasen, E. Norbeck, C.A. Ogilvie, N. Stone, D. Swan, A. Vander Molen, W.K. Wilson, J.S. Winfield, J. Yurkon, and G.D. Westfall, Nucl. Inst. and Meth. A300, 518 (1991).
- [Cebr 92] D.A. Cebra, W.K. Wilson, A.M. Vander Molen, and G.D. Westfall, Nucl. Inst. and Meth. A313, 367 (1992)
- [Chia 84] E. Chiavassa, S. Costa, G. Dellacasa, N. De Marco, M. Gallio, A. Musso,
   E. Aslanides, P. Fassnacht, F. Hibou, T. Bressani, M. Caria, S. Serci, F. Iazzi, and B. Minetti, Nucl. Phys. A422 621 (1984).
- [Cugn 83] J. Cugnon and D. L'Hôte, Nucl. Phys. A397, 519 (1983).
- [Dani 83] P. Danielewicz and M. Gyulassy, Phys. Lett 129B, 283 (1983).
- [Dani 85] P Danielewiczand G. Odyniec, Phys. Lett. 157B, 146 (1985)
- [Dani 88] P. Danielewicz, H. Ströbele, G. Odyniec, D. Bangert, R. Bock, R. Brockmann, J.W. Harris, H.G. Pugh, W. Rauch, R.E. Renfordt, A. Sandoval, D. Schall, L.S. Schroeder, and R. Stock, Phys. Rev. C38, 120 (1988).
- [Eraz 88] B. Erazmus, C. Guet, R. McGrath, M.G. Saint-Laurent, Y. Schutz, J.L. Ciffre, M. Boloré, Y. Cassagnou, H. Dabrowski, M. Hisleur, J. Julien, R. Legrain, C. Le Brun, J.F. Lecolley, and M. Louvel, Nucl. Phys. A481, 821 (1988).

- [Glas 83] R. Glasow, G. Gaul, B. Ludewigt, R. Santo, H. Ho, W. Kühn, U. Lynen, and W.F.J. Müller, Phys. Lett. B120, 71 (1983).
- [Goss 89] J. Gosset, O.Valette, J.P. Alard, J. Augerat, R. Babinet, N. Bastid, F. Brochard, N. De Marco, P. Dupieux, Z. Fodor, L. Fraysse, P. Gorodetzky, M.C. Lemaire, D. L'Hôte, B. Lucas, J. Marroncle, G. Montarou, M.J. Parizet, J. Poitou, C. Racca, A. Rahmani, W. Schimmerling, and Y. Terrien, Phys. Rev. Lett. 62, 1251 (1989).
- [Grim 85] P. Grimm and E. Grosse, Progr. in Part. and Nucl. Phys. 15, 339 (1985).
- [Gust 84] H.A. Gustfsson, H.H. Gutbrod, B. Kolb, H. Löhner, B. Ludewigt, A.M. Poskanzer, T. Renner, H. Riedesel, H.G. Ritter, A. Warwick, F. Weik, and H. Wieman, Phys. Rev. Lett. 52, 1590 (1984).
- [Gutb 89] H.H. Gutbrod, A.M. Poskanzer, and H.G. Ritter, Rep. Prog. Phys. 52, 1267 (1989)
- [Heck 84] H. Heckwolf, E. Grosse, H. Dabrowski, O. Klepper, C. Michel, W.F.J. Müller, H. Noll, C. Brendel, W. Rösch, J. Julien, G.S. Pappalardo, G. Bizard, J.L. Laville, A.C. Mueller, and J. Péter, Z. Phys. A315, 243 (1984).
- [Hsi 94] W.C. Hsi, G.J. Kunde, J. Pochodzalla, W.G. Lynch, M.B. Tsang, M.L. Begemann-Blaich, D.R. Bowman, R.J. Charity, F. Cosmo, A. Ferrero, C.K. Gelbke, T. Glasmacher, T. Hofmann, G. Imme, I. Iori, J. Hubele, J. Kempter, P. Kreutz, W.D. Kunze, V. Lindenstruth, M.A. Lisa, U. Lynen, M. Mang, A. Moroni, W.F.J. Müller, M. Neumann, B. Ocker, C.A. Ogilvie, G.F. Peaslee, G. Raciti, F. Rosenberger, H. Sann, R. Scardaoni, A. Schüttauf, C. Schwarz, W. Seidel, V. Serfling, L.G. Sobotka, L. Stuttge, S. Tomasevic, W. Trautmann, A. Tucholski, C. Williams, A. Wörner, and B Zwieglinski, Phys. Rev. Lett. 73, 3367 (1994).
- [Joha 82] T. Johansson, H.-Å. Gustafsson, B. Jakobsson, P. Kristiansson, B. Norén, A. Oskarsson, L. Carlén, I. Otterland, H. Ryde, J. Julien, C. Guet, R. Bertholet, M. Maurel, H. Niefenecker, P. Perrin, F. Schussler, G. Tibell, M. Buenerd, J.M. Loiseaux, P. Martin, J.P. Bondorf, O.-B. Nielsen, A.O.T. Karvien, and J. Mougey, Phys. Rev. Lett. 48, 732 (1982).
- [Krof 89] D. Krofcheck, W. Bauer, G.M. Crawley, C. Djalali, S. Howden, C. A. Ogilvie, A.M. Vander Molen, G.D. Westfall, W.K. Wilson, R.S. Tickle, and C. Gale, Phys. Rev. Lett. 63, 2028 (1989)
- [Krof 91] D. Krofcheck, D.A. Cebra, M. Cronquist, R. Lacey, T. Li, C. A. Ogilvie, A.M. Vander Molen, K. Tyson, G.D. Westfall, W.K. Wilson, J.S. Winfield, A. Nadasen, and E. Norbeck, Phys. Rev. C43, 350 (1991)
- [Krof 92] D. Krofcheck, W. Bauer, G.M. Crawley, S. Howden, C. A. Ogilvie, A.M. Vander Molen, G.D. Westfall, W.K. Wilson, R.S. Tickle, C. Djalali, and C. Gale, Phys. Rev. C46, 1416 (1992)

- [Lebr 90] D. Lebrun, G.Perrin, P. de Saintignon, R. Bougault, D. Durand, A. Genoux-Lubain, J. Julien, C. LeBrun, J.F. Lecollen, and M. Laurel, Proc. of IN2P3-RIKEN Symp. on Heavy Ion Collisions, eds. B. Hersch and M. Ishihara, World Scientific, 209 (1990).
- [Li 91a] B.-A. Li and W. Bauer Phys. Rev. C44, 450 (1991)
- [Li 91b] B.-A. Li, W. Bauer, and G.F. Bertsch, Phys. Rev. C44, 2095 (1991)
- [Llop 93] W.J. Llope, D. Craig, E. Gualtieri, S. Hannuschke, R.A. Lacey, T. Li, A. Nadasen, E. Norbeck, R. Pak, N. Stone, A.M. Vander Molen, G.D. Westfall, J.S. Winfield, J. Yee, and S.J. Yennello, Michigan State University Preprint, MSUCL-900.
- [Llop 95] W.J. Llope, J.A. Conrad, C.M. Mader, G. Peilert, W. Bauer, D. Craig,
  E. Gualtieri, S. Hannuschke, R.A. Lacey, J. Lauret, T. Li, A. Nadasen,
  E. Norbeck, R. Pak, N.T.B. Stone, A.M. Vander Molen, G.D. Westfall, J.
  Yee, and S.J. Yennello, Phys. Rev. C51, 1325 (1995).
- [Vand 91] A. Vander Molen, M.R. Maier, M. Robertson, and G.D. Westfall, Nucl. Inst. and Meth., A307, 116 (1991).
- [Mill 87] J. Miller, J. Bercovitz, G. Claesson, G. Krebs, G. Roche, L.S. Schroeder, W. Benenson, J. van der Plicht, J.S. Winfield, G. Landaud, and J.-F. Gilot, Phys. Rev. Lett. 58, 2408 (1987).
- [Moli 85] J.J. Molitoris, D. Hahn, and H. Stocker, Nucl. Phys. A447, 13c (1985).
- [Haya 88] S. Hayashi, Y. Miake, T. Nagae, S. Ngamiya, H. Hamagaki, O. Hashimoto, Y. Shida, I. Tanihata, K. Kimura, O. Yamakawa, T. Kobayashi, and X.X. Bai, Phys. Rev. C38, 1229 (1988) Don't know.
- [Naga 81] S. Nagamiya, M.-C. Lemaire, E. Moeller, S. Schnetzer, G. Shapiro, H. Steiner, and I. Tanihata, Phys. Rev. C24, 971 (1981).
- [Naga 82] S. Nagamiya, H. Hamagaki, P. Hecking, S. Kadota, R. Lombard, Y. Miake, E. Moeller, S. Schnetzer, H. Steiner, I. Tanihata, S. Bohrmann, and J. Knoll, Phys. Rev. Lett. 48, 1780 (1982).
- [Niit 91] K. Niita, Proceedings of the 4th International Conference on Nucleus-Nucleus Collisions, Kanazawa, Japan, 1991, p. 183.
- [Noll 84] H. Noll, E. Grosse, P. Braun-Munzinger, H. Dabrowski, H. Heckwolf, O. Klepper, C. Michel, W.F.J. Müller, H. Stelzer, C. Brendel, and W. Rösch, Phys. Rev. Lett. 52, 1284 (1984).
- [Ogil 89] C.A. Ogilvie, D.A. Cebra, J. Clayton, P. Danielewicz, S. Howden, J. Karn, A. Nadasen, A.M. Vander Molen, G.D. Westfall, W.K. Wilson, and J.S. Winfield, Phys. Rev. C40, 2592 (1989).
- [Ogil 89] C.A. Ogilvie, W. Bauer, D.A. Cebra, J. Clayton, S. Howden, J. Karn, A. Nadasen, A.M. Vander Molen, G.D. Westfall, W.K. Wilson, and J.S. Winfield, Phys. Rev. C42, R10 (1990).

- [Pak 95] R. Pak, W.J. Llope, D. Craig, E.E. Gualtieri, S.A. Hannuschke, R.A. Lacey, J. Lauret, A.C. Mignerey, D.E. Russ, N.T.B. Stone, A.M. Vander Molen, G.D. WWestfall, and J. Yee, submitted for publication in Phys. Rev. C.
- [Phai 92] L. Phair, D.R. Bowman, C.K. Gelbke, W.G. Gong, Y.D. Kim, M.A. Lisa, W.G. Lynch, G.F. Peaslee, R.T. de Souza, M.B. Tsang, and F. Zhu, Nucl. Phys. A548, 489 (1992).
- [Schu 94] A. Schubert, R. Holzmann, S. Hlaváč, R. kulessa, W. Niebur, R.S. Simon, P. Lauridou, F. Lefòvre, M. Marqués, T. Matulewicz, W. Mittig, R.W. Ostendorf, P. Roussel-Chomaz, Y. Schutz, H. Löhner, J.H.G. van Pol, R.H. Siemssen, H.W. Wilschut, F. Ballester, J. Díaz, A. Marín, G. Martinez, V. Metag, R. Novotny, V. Wagner, and J. Québert, Phys. Lett. B328, 10 (1994)
- [Sull 90] J.P. Sullivan, J.Péter, D. Cussol, G. Bizard, R. Brou, M. Louvel, J.P. Patry, R. Regimbart, J.C. Steckmeyer, B. Tamain, E. Crema, H. Doubre, K. Hagel, G.M. Jin, A. Péghaire, F. Saint-Laurent, Y. Cassagnou, R. Lebrun, E. Rosato, R. Macgrath, S.C. Jeong, S.M. Lee, Y. Nagashima, T. Nakagawa, M. Ogihara, J. Kasagi, and T. Motobayashi, Phys. Lett. B249, 8 (1990).
- [Suzu 91a] T. Suzuki, M. Fukuda, T. Ichihara, N. Inabe, T. Kubo, T. Nakagawa, K. Yoshida, I. Taniahata, T. Kobayashi, T. Suda, S. Shimoura, and M. Fujiwara, Phys. Lett. **B257**, 27 (1991).
- [Suzu 91b] T. Suzuki, N. Inabe, T. Nakagawa, K. Yoshida, and I. Taniahata, Proceedings of the 4th International Conference on Nucleus-Nucleus Collisions, Kanazawa, Japan, 1991, p. 182.
- [Suzu 92] T. Suzuki, Nucl. Phys. A538, 113c (1992).
- [Vand 94] A. Vander Molen, R. Au, R. Fox, and S. Hannuschke, IEEE Trans. on Nucl. Sci., 41 (1994) 80
- [West 85] G.D. Westfall, J.E. Yurkon, J. van der Plicht, Z.M. Koenig, B.V. Jacak, R. Fox, G.M. Crawley, M.R. Maier, B.E. Hasselquist, R.S. Tickle, and D. Horn, Nucl. Inst. and Meth. A238, 347 (1985).
- [West 93] G.D. Westfall, W. Bauer, D. Craig, M. Cronquist, E. Gualtieri, S. Hannuschke, D. Klakow, T. Li, T. Reposeur, A.M. Vander Molen, W.K. Wilson, J. Yee, S. Yenello, R. Lacey, A. Elmaani, J. Lauret, A. Nadasen, and E. Norbeck, Phys. Rev. Lett 71, 1986 (1993).
- [Wils 90] W.K. Wilson, W. Benenson, D.A. Cebra, J. Clayton, S. Howden, J. Karn, T. Li, C. A. Ogilvie, A.M. Vander Molen, G.D. Westfall, J.S. Winfield, A. Nadasen, and E. Norbeck, Phys. Rev. C41, R1881 (1990).
- [Wils 91] W.K. Wilson, Ph.D. Thesis, Michigan State University, 1991.
- [Wils 92] W.K. Wilson, R. Lacey, C.A. Ogilvie, and G.D. Westfall, Phys. Rev. C45, 738 (1992)

[Zhan 90] W.M. Zhang, R. Madey, M. Elaasar, J. Schambach, D. Keane, B.D. Anderson, A.R. Baldwin, J. Cogar, J.W. Watson, G.D. Westfall, G. Krebs, and H. Wieman, Phys. Rev. C42, R491 (1990)

MICHIGAN STATE UNIV. LIBRARIES
31293013904523